



TECHNISCHE
UNIVERSITÄT
WIEN

DISSERTATION

Towards high-precision VUV frequency comb spectroscopy of the thorium-229 nuclear isomer

ausgeführt zum Zwecke der Erlangung des akademischen Grades eines
Doktors der technischen Wissenschaften

von

Dipl.-Ing. Georg Winkler

Matrikelnummer 0127119

Goethegasse 1/30

2500 Baden, Österreich

unter der Leitung von

Prof. Dr. Thorsten Schumm

Atominstitut (E141)

eingereicht an der

Technischen Universität Wien

Fakultät für Physik

Wien, Juli 2016

Die Dissertation haben begutachtet:

G. Winkler

T. Schumm

T.Udem

To my parents.

Typesetting: The Author
Day of Print: July 6, 2016

Zusammenfassung

Laut Vorhersagen besitzt das Radioisotop Thorium-229 einen äußerst niederenergetischen angeregten Kernzustand im Bereich von 7.8 ± 0.5 eV, welcher erstmals die Aussicht auf kohärente Manipulation eines Atomkerns mittels (VUV) Laserlichts bietet [1–2]. Vom Aspekt der Grundlagenforschung (welcher auch die Frage nach einer zeitlichen Variation der Fundamentalkonstanten beinhaltet) abgesehen, ermöglicht der gut abgeschirmte schmalbandige Kernübergang die Realisierung eines kompakten Festkörper-basierten optischen Frequenznormals, mit um Größenordnungen verbesserter Präzision und absoluter Genauigkeit gegenüber existierenden Systemen [3–4].

Da es nicht möglich ist optische (THz) Frequenzen direkt mit elektronischen Messgeräten zu erfassen, wird ein optisches „Uhrwerk“ benötigt, welches für eine exakte Frequenzteilung bis hinunter in den Radiofrequenzbereich sorgt, wo einzelne Oszillationsperioden direkt gezählt und mit existierenden Frequenzstandards (wie Cäsium-Atomuhren) verglichen werden können. Dieses Problem besteht gleichermaßen für alle optischen Uhren, und wurde erst kürzlich mit der Erfindung optischer Frequenzkämme gelöst. Solche speziell stabilisierten Femtosekunden-Kurzpulslaser sind durch ein breites durchstimmbares Spektrum charakterisiert, welches sich aus vielen exakt äquidistanten schmalbandigen Frequenzlinien zusammensetzt. Über die Messung eines Schwebungssignals kann ein solches „Lineal im Frequenzraum“ als exakte Referenz zur Bestimmung unbekannter optischer Frequenzen verwendet werden. Zwecks Einsatzes eines solchen vielseitigen Werkzeugs in Hinblick auf eine „Thorium Uhr“, müssen existierende Femtosekunden-Laserquellen - welche nur im sichtbaren bzw. nahen Infrarotbereich zur Verfügung stehen - jedoch in den Wellenlängenbereich von 159 ± 10 nm konvertiert werden, in dem der Kernübergang erwartet wird.

Unser Zugang zu dieser Frequenzvervielfachung (und Inhalt dieser Doktorarbeit) ist die Generierung einer fünften Harmonischen eines Titan:Saphir-Laser-basierten Frequenzkamms mit einer Zentralwellenlänge von 800 nm, durch Erzeugung höherer Harmonischer in einem Xenon Gasstrahl innerhalb eines optischen Überhöhungsresonators. Durch diesen Prozess wird sowohl die kurze Pulsdauer von etwa 25 fs als auch die hohe Wiederholrate (108 MHz) der Quelle erhalten. Es wurde ebenfalls bereits gezeigt, dass dabei die Phasenkohärenz, und damit die ursprüngliche Kammstruktur, erhalten bleibt [5].

Obwohl konzeptuell einfach, bietet der Aufbau eines solchen Systems einige fundamentale Herausforderungen: Der stark nichtlineare Prozess der Erzeugung höherer Harmonischer hat eine sehr geringe Konversionseffizienz. Basierend auf einer Laserquelle mit lediglich 900 mW verfügbarer Leistung, wird außerdem selbst in einem Überhöhungsresonator mit relativ großem Verstärkungsfaktor von 250, die erforderliche maximale Leistungsdichte von über 10^{13} W/cm² nur knapp erreicht. Wie bereits durch den Namen angedeutet, wird die erzeugte Vakuumultraviolettstrahlung durch Luftsauerstoff absorbiert, so dass der Aufbau nur innerhalb einer Vakuumkammer betrieben werden kann, was auch die Fernsteuerung aller notwendigen Stellelemente erforderlich macht. Sowohl die Träger-Einhüllenden-Phase als auch die Pulswiederholrate müssen relativ zum Resonator stabilisiert werden.

Dabei müssen Effekte chromatischer Dispersion, welche eine zeitliche Verbreiterung und Chirp der Pulse hervorrufen, genau kontrolliert werden. Allgemein sind Femtosekunden-Resonatoren (hoher Finesse) sehr empfindlich gegenüber Vibrationen, und erfordern eine sehr hohe mechanische Stabilität der Anordnung. Die effiziente Auskopplung der (kollinear) erzeugten harmonischen Strahlung ist eine nichttriviale Anforderung, ebenso wie die Optimierung der Phasenanpassung und der Geometrie des Gasstrahls.

Um einen möglichst kleinen Fokus innerhalb des Resonator, und ein sauberes Gaußförmiges Strahlprofil der harmonischen Strahlung sicherzustellen, führen wir eine neuartige dreidimensionale Resonatorgeometrie ein. Die spezielle Anordnung verhindert ein elliptisches Strahlprofil im Fokus, welches typischerweise durch den leicht schrägen Einfallswinkel auf sphärische Spiegel verursacht wird, und erhält dabei eine lineare Polarisationsrichtung. Die dritte und fünfte Harmonische des Frequenzkamms wurde (mit Leistungen von $20 \mu\text{W}$ und 60nW) erfolgreich erzeugt.

Abstract

The radio isotope thorium-229 is predicted to possess a unique, extremely low-energy metastable excited state of the nucleus in the range of 7.8 ± 0.5 eV [1–2], offering the chance to coherently manipulate a nucleus by (VUV) laser light for the first time. Apart from exciting fundamental research questions (including the search for temporal variations of fundamental constants), this well-shielded narrow-linewidth transition opens up the possibility to realize a compact solid-state optical time standard, surpassing existing systems by orders of magnitude in both precision and accuracy [3–4].

Since optical (THz) frequencies can't be directly measured using electronic equipment, an optical “clockwork” is needed to exactly divide them down to the radio frequency regime, where individual oscillations can be counted and compared to existing standards (like cesium atomic clocks). This problem arises for all types of optical clocks and has been recently solved by the advent of optical frequency combs. These specially stabilized femtosecond lasers provide a broad tunable spectrum of exactly equidistant narrow-linewidth frequency components, which can be thought of as a “ruler in frequency space”, usable as a reference for precise beat-note measurements of any unknown optical frequency. In order to apply these versatile tools to a potential “thorium clock”, existing femtosecond laser sources - which operate in the visible to near-infrared domain - somehow have to be converted to the 159 ± 10 nm range where the nuclear transition is expected.

Our approach to this frequency-upconversion (and scope of this thesis) is the generation of the 5th harmonic of a titanium-sapphire laser based comb, with a central wavelength of 800 nm, by means of high harmonic generation (HHG) in a xenon gas jet, inside a passive external enhancement resonator. This allows to maintain the short pulse length of around 25 fs and the high repetition rate (108 MHz) of the source. It has also been already demonstrated that the phase coherence and thereby the comb structure of the source is conserved in the process [5].

However, although conceptually simple, the setup involves several fundamental challenges: The highly nonlinear process of HHG has a very low conversion efficiency, and the required high peak power density above 10^{13} W/cm² is barely reached inside the enhancement cavity on the basis of only 900 mW of available fundamental power, even with a comparably large power enhancement factor of 250. As already implied by the name vacuum ultraviolet (VUV), light at the target wavelength is absorbed by oxygen in air, so that everything has to be operated under vacuum conditions and remote-controlled. Both carrier-envelope offset frequency and pulse repetition rate have to be stabilized to the cavity. Chromatic dispersion effects, leading to pulse chirp and temporal broadening, have to be strictly controlled. Generally, (high-finesse) femtosecond enhancement cavities also have very strict requirements on mechanical stability. Efficient outcoupling of the (collinearly) generated harmonic light from the cavity is a non-trivial task, as is the optimization of phase matching and the gas jet geometry.

To ensure a tight intracavity focus and clean Gaussian beam profiles of the generated harmonics, we introduce a novel three-dimensionally folded variant of the typical planar bow-tie resonator geometry. This scheme allows us to mitigate the formation of an elliptical intracavity focus, usually caused by oblique incidence on spherical focusing mirrors, while still maintaining linear polarization. Third and fifth harmonic signals are successfully generated with average powers of $20\ \mu\text{W}$ and $60\ \text{nW}$ respectively.

Contents

1	Introduction	
1.1	On the importance of precision measurements and frequency metrology in particular	1
1.2	Optical clocks and the success story of the optical frequency comb	3
1.3	A solid-state approach towards a Th-229 based nuclear clock	6
2	Spectroscopy with an optical frequency comb	
2.1	Optical frequency comb basics	9
2.1.1	Modelocked femtosecond lasers	9
2.1.2	Frequency comb stabilization	12
2.1.3	Frequency metrology with a comb	13
2.1.4	Direct frequency comb spectroscopy	15
2.2	Short pulse diagnostics	17
2.2.1	Group delay dispersion, pulse chirp and transform limit	17
2.2.2	SPIDER measurement scheme	21
2.3	The Ti:Sa oscillator	23
2.4	Metrology experiments in the visible and near-IR spectrum	25
2.4.1	Use of the comb as a real time high-precision wavemeter	25
3	A novel non-planar passive femtosecond enhancement cavity design	
3.1	Pulse amplification for nonlinear conversion applications	31
3.2	Enhancement cavity basics	31
3.2.1	Resonance, power enhancement and impedance matching	31
3.2.2	Finesse, dispersion effects and spectral mode matching	36
3.2.3	Transversal modes, stability and spatial mode matching	39
3.3	Counteracting astigmatism in fsECs	42
3.3.1	Conventional cavity design	42
3.3.2	Non-planar cavity design	46
4	Experimental realization of the EC	
4.1	Overview of the resonator setup	49
4.2	3D beam folding	50
4.3	Geometrical alignment	51
4.4	Dispersion management	56
4.5	Spectral mode matching and cavity lock	59
4.6	Vacuum system and vibration isolation	60
4.7	Cavity characterization	65
5	A frequency comb at 160nm via HHG	
5.1	High harmonic generation theory	69
5.1.1	Perturbative harmonic generation	69
5.1.2	Semi-classical strong field approximation	71

5.1.3	Phase matching	73
5.2	Experimental realization	75
5.2.1	Gas supply and nozzle design	75
5.2.2	Output couplers	76
5.2.3	XUV detection	80
5.2.4	HHG results	81

6 Conclusions and Outlook

A	Driver electronics for shear piezoelectric motors	87
	Acknowledgements	91
	List of Publications	93
	References	95
	Curriculum Vitae	101

1 Introduction

1.1 On the importance of precision measurements and frequency metrology in particular

Advances in the field of precision¹ measurement and standardization² might seem to be a bureaucratic endeavor at times, however, they have always been one (if not “the”) cornerstone of scientific and technological progress.

The *scientific method* owes a lot of its success to putting “observation” first, and “explanation” second. Precision measurements are also at the core of its ambition to “dig deeper”, to expose basic mechanisms which can explain complex systems from the bottom up. History has proven, that if there is some chance to improve the precision of a measurement technique by an order of magnitude, it is usually worth the effort, because new effects - previously masked by measurement uncertainty - will become visible and extend our physical understanding and toolbox.

This notion of “going where no one has gone before” is most obvious for a measurement device which is a direct extension of our (most relied on) visual sense - the microscope. In the above sense, it is nothing else than a “high precision³ length (and thereby position) measurement device”, and its invention has literally opened completely new worlds in biology, medicine, material science and electronics, just to name a few. The same also applies for less tangible quantities like magnetic field strength. The discovery of the giant magnetoresistance effect (GMR), for example, has enabled the sensitive detection necessary for the high storage densities of modern day magnetic hard drives.

Interestingly, the quantity we can measure with by far highest precision to date, is frequency. This is grounded in the fact that such a measurement involves counting the number of oscillations during a given time interval, which is an intrinsically digital process, immune to many sources of noise [6]. This partly explains the special role of precision spectroscopy in fueling a lot of our insight into the atomic world, by looking at ever smaller details of electromagnetic emissions from matter (ranging from Bohr model energy levels to fine structure, to Lamb shift, to hyperfine structure). It also explains why there is an avid interest in defining other quantities through relations to a frequency via some fundamental physical process (like the Josephson effect, which translates voltage to frequency). The measurement of time is a trivial example in this respect, following the relation $f = 1/T$.

¹ Although precision (variability of the results from repeated measurements of the same quantity) and accuracy (deviation of the mean of said measurement set from the “true” value) are very different things, one often implies both when informally talking about a “precision measurement device”.

² Standardization refers to the realization of accurate measurements by providing universally agreed upon calibration standards.

³ Resolution (size of discernible increments in the digital measurement outcome) determines an upper bound for precision. Therefore high precision always implies high resolution - the opposite is however not generally true.

Length is also an “easy one”: If we trust in the constancy of the speed of light⁴ in vacuum, we can, for example, relate it to the frequency with which a light pulse is bouncing back and forth between two mirrors at a given distance⁵.

In the end, the absolute value of a measurement is always derived by some comparison procedure relative to a physical standard for the measured quantity, even if this measured quantity is a frequency⁶.

In order to make meaningful and comparable measurements, such a standard needs to be accurate (Fig. 1.1). Ideally it should have no temporal drift⁷ (due to uncontrolled external influences) and it should be universally agreed upon, with no shifts between different realizations of the same standard. The last issue can be solved by calibrating copies against some designated primary standard (like the former international prototype meter - a platinum iridium bar stored by the *bureau international des poids et mesures*). However, it is even more convenient, if (at least the primary standard) is easily reproducible, for example by exploiting atomic characteristics (like the frequency of a cesium hyperfine transition currently defining the SI second) which are intrinsically the same for each atom of the same species. Depending on the precision of a standard (or stability, in the context of frequency standards), a certain averaging time is necessary to achieve its ultimate accuracy.

In any case, just like the precision of measurements, the practical relevance of accurate standards can hardly be overemphasized. If we think of times where length has been measured in multiples of the size of peoples limbs (like an “ell” or a “foot”) so that no two pieces of separately manufactured table legs would match together to be integrated in one table, this becomes pretty obvious. This is even true for current time standards with fractional frequency deviations on the order of 10^{-17} (clocks that lose or gain no more than a second over the estimated age of the universe). The transmission of ever-increasing amounts of data over telecommunication channels - let’s say “the internet” - is all about timing and synchronization. Zeroes and ones have to be so “densely packed” that exactly synchronized clocks on the sender and receiver end are needed to decode the information content without ambiguity. The global positioning system (GPS) relies at its very core on accurate atomic clocks on board its satellites. The triangulation of a receiver position leverages information about its distance to several satellites, derived by

⁴ In the sense of a firm belief, that this assumption is so basic, that it will never lead to complications in modeling our physical world. Since the simplest model is always the best model, it is of course always possible, that such assumptions could ultimately be challenged, based on new empirical findings, enabled by further improved measurement techniques.

⁵ The relation $x = c_0 \cdot t$ is exactly what the current SI definition of the meter exploits. Previously the relation between the wavelength and frequency of propagating light was used as a definition. However, the realization of this translation in an interferometer suffers from a number of uncertainties such as wavefront distortion. This emphasizes, that the fundamental process providing the frequency link, must be very well understood and controllable.

⁶ So, in the best case, we need at least one standard - a frequency (or time) standard!

⁷ Undeniably, there is somewhat of a semantical problem with the concept of temporal constancy, considering that a primary standard actually absolutely defines a quantity. Nevertheless, comparison of at least three realizations of the same standard, can enable an assessment of individual “quality”.

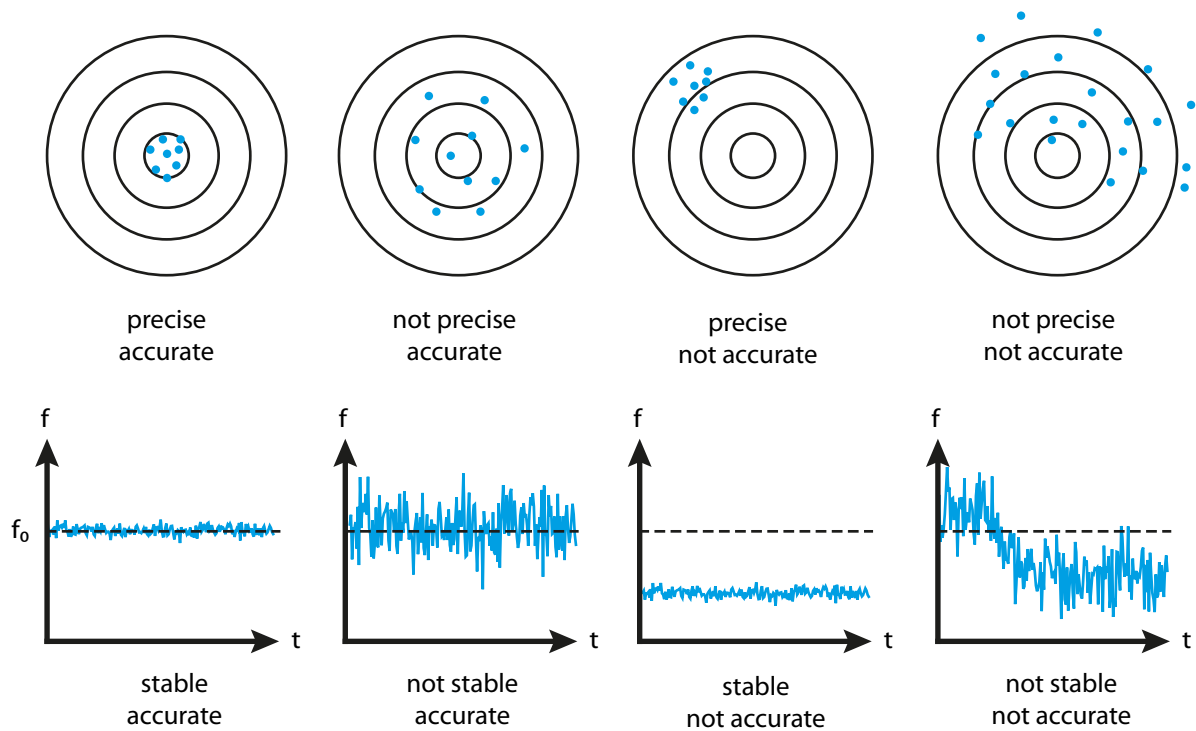


Figure 1.1 Illustration of the precision of a measurement (stability of an oscillator) versus accuracy.

measuring the time of travel of signals they emit (traveling at the speed of light). In detail, this is done by comparing the (digital) timestamps (marking the time of signal emission) for signals originating from different satellites, but received at the same time - a feat which only works if those on-board clocks keep the same time to very high accuracy. Already three centuries ago, the most accurate mechanical clocks (famously built by John Harrison for the royal navy, around the time of the Anglo-Spanish war) were top secret military technology, because they first enabled practical marine navigation (accurate determination of the longitude, in particular). For a fixed observer, the regular trajectories of celestial objects can be used as a (slow) reference oscillator, or time standard. This is not possible for a moving observer who has no knowledge of his current position, however, he can calculate exactly this information based on the position of those objects, if he has access to an alternative clocking device (like those first marine chronometers) that is accurately synced to the celestial motions.

1.2 Optical clocks and the success story of the optical frequency comb

While accuracy is, in a sense, the most important characteristic of a frequency standard, we already mentioned how a bad stability (precision) leads to the requirement of long averaging times to reduce statistical fluctuations to the level of the oscillators intrinsic accuracy. The current U.S. civilian time standard, the NIST-F1 cesium fountain clock, for

example, must be averaged for about five days to achieve its best performance. This can be a practical limitation.

A common measure of a clocks frequency (in)stability (dependent on the averaging time τ) is the Allan deviation $\sigma_y(\tau)$. It can be shown that it is ultimately limited⁸ by quantum projection noise [7–8], following the scaling behaviour

$$\sigma_y(\tau) \propto \frac{\Delta f}{f\sqrt{N}\tau} \quad (1.1)$$

where Δf is the natural linewidth of the (atomic) reference oscillators (only realized for sufficiently long measurement times), f their frequency, and N their number.

This result makes intuitive sense, as the ratio $\Delta f/f$ (inverse of the *quality factor* $Q = f/\Delta f$) exactly quantifies the relative uncertainty in the instantaneous frequency of a (theoretical) drift-free oscillator⁹. Observing a factor of N larger number of oscillators is just a means of speeding up the averaging process, equivalent to a factor of N increase in averaging time.

Equation 1.1 directly motivates the trend in the evolution of frequency standards, to always use reference oscillators with the highest usable frequency compatible with current technology. This involves the progression from mechanical pendulums, to electrical quartz oscillators, to radio frequency atomic transitions (like the cesium clock) to current experimental primary standards based on optical transitions. The last technological step has only happened quite recently. Although precision narrow-linewidth lasers are long available for interrogation of optical atomic transitions, there still doesn't exist a measurement device which is able to directly count the oscillations of the electric field amplitude of an electromagnetic wave in the visible spectral range.

What is possible, however, is to slow down these oscillations via exact frequency division, until a frequency domain is reached where individual oscillations can be readily counted. Efforts of epic proportions have therefore been undertaken, to realize such a link spanning from the optical domain (hundreds of Terahertz) to the radio frequency (Gigahertz) domain, by so called *frequency chains*. These “devices” coupled a multitude of oscillators based on completely different technologies, filled entire rooms, and required several people to maintain operation (Fig. 1.2).

The problem has been thoroughly solved by the advent of frequency comb technology (explained in detail in Ch. 2) replacing above installations with a compact, tabletop laser setup of even more general applicability. A Nobel prize was awarded in 2005 to Theodor W. Hänsch and John L. Hall in honor of this achievement.

⁸ In practice, other sources of noise are often by far more dominant contributions.

⁹ The main argument to actually use the above Allan deviation to characterize stability, instead of simply stating a linewidth, is that the latter is a badly defined (not converging) quantity, when experimentally determined for a real oscillator, subject to a temporally drifting mean value.

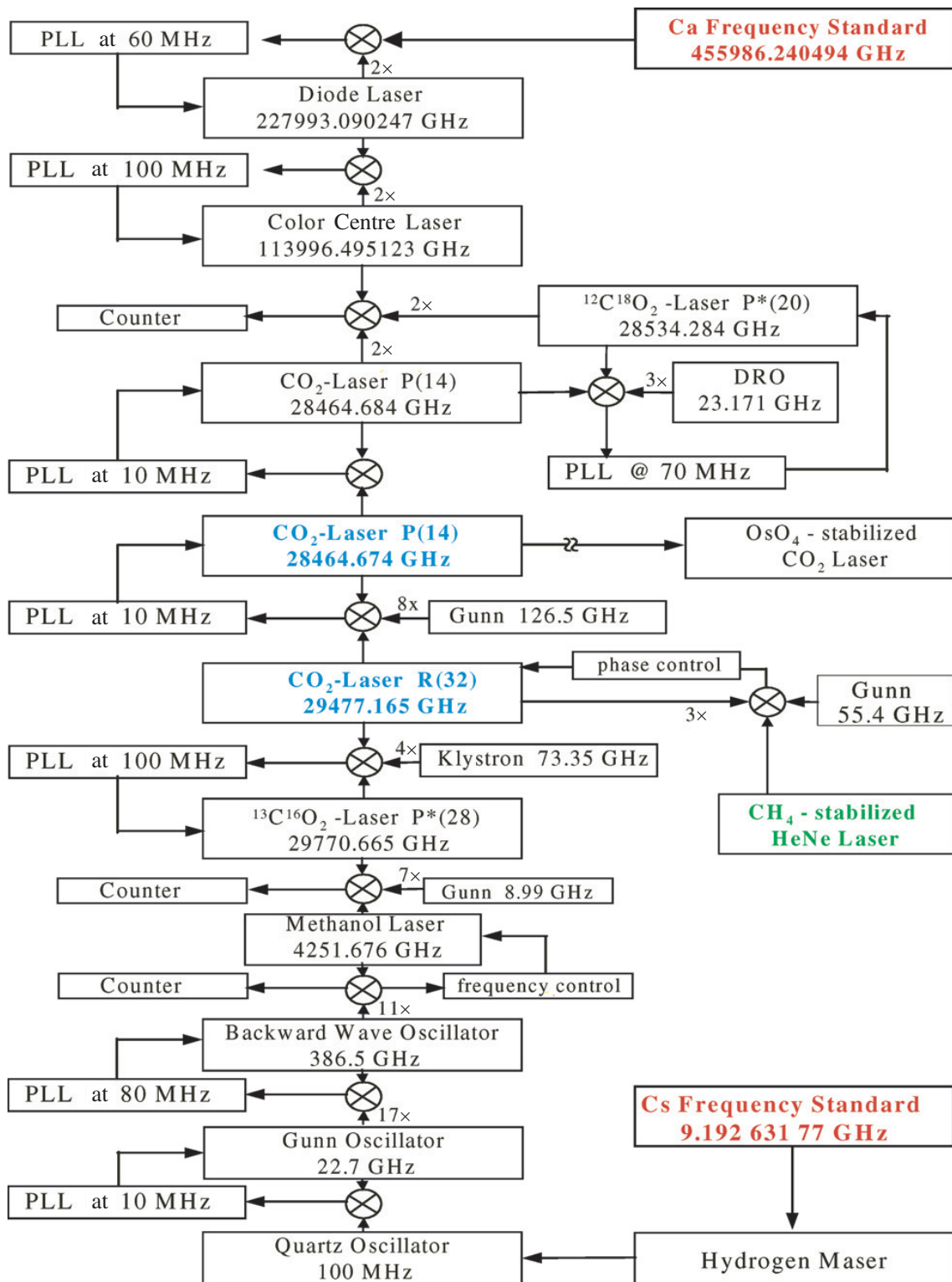


Figure 1.2 The frequency chain of the German *Physikalisch Technische Bundesanstalt* (PTB) was the first to achieve a phase-coherent connection between the cesium primary standard and an optical-frequency reference in the visible range. Chart reproduced from [9]

1.3 A solid-state approach towards a Th-229 based nuclear clock

Following the arguments of the previous chapter, nuclear transitions - involving energies of the emitted γ -radiation in the keV to MeV range (with correspondingly higher frequency compared to atomic emission spectra in the eV range) - would be even better candidates as clock transitions.

An added advantage would be the possibility for straightforward Doppler free detection of a large ensemble of nuclear oscillators (advantageous according to Eq. 1.1), when confined to the recoil-free Lamb-Dicke regime inside a crystal matrix (as exploited in Mößbauer spectroscopy). Current ion or optical lattice atomic clocks, by comparison, need intricate trapping schemes to suppress Doppler shifts, which also limit the number of oscillators (to an order of 10^4 atoms for optical lattice clocks), which can be simultaneously interrogated.

Unfortunately, counters for such high frequencies are technologically not available today. However, among all nuclear transitions, the transition between the thorium-229(m) metastable excited state (so-called *isomer* state) and its ground state, features a uniquely small energy of 7.8 ± 0.5 eV, which puts it in the VUV (vacuum ultraviolet) frequency range. The corresponding wavelength range of about 159 ± 10 nm is right at the edge of the region potentially accessible for coherent control via the tools of laser spectroscopy. As will be detailed in chapters 3 and 5, optical frequency combs can be extended to this spectral region via the process of high harmonic generation in external enhancement cavities. The long expected lifetime of the (metastable) state of around 1000 seconds¹⁰, corresponds to a very small Millihertz linewidth of the nuclear transition, constituting yet another incentive to exploit it as a frequency standard¹¹.

Maybe even more importantly, a “nuclear clock” based on this transition could eventually outperform existing atomic clocks with respect to accuracy, since systematic frequency shifts through external electric or magnetic fields are heavily suppressed due to the nuclear nature of the transition [3].

The first studies of this isomer transition date back as far as the 1970s, when it was noticed that the ground state of thorium-229 is energetically very close to its first excited state [12–13]. Unfortunately, a direct optical excitation or de-excitation of the transition has not yet been observed. The currently accepted energy value is a result of an indirect measurement based on the (high-energy) gamma-ray spectrum of thorium-229 produced in the alpha decay of uranium-233, acquired with a state of the art high-resolution microcalorimeter [1–2] in 2007. It is worth noting that derivation of the isomer energy according to Fig. 1.3(a) required measuring the keV lines with sub-eV precision¹².

¹⁰ Estimate of the lifetime for a bare nucleus (or highly ionized atom) [10–11].

¹¹ If embedded inside a solid state sample, broadening effects due to internal fields will however lead to a significantly larger linewidth.

¹² Although the energy resolution in this experiment is only stated with 26 eV (FWHM), the centroids of energy peaks in the line spectrum can be determined with much higher precision.

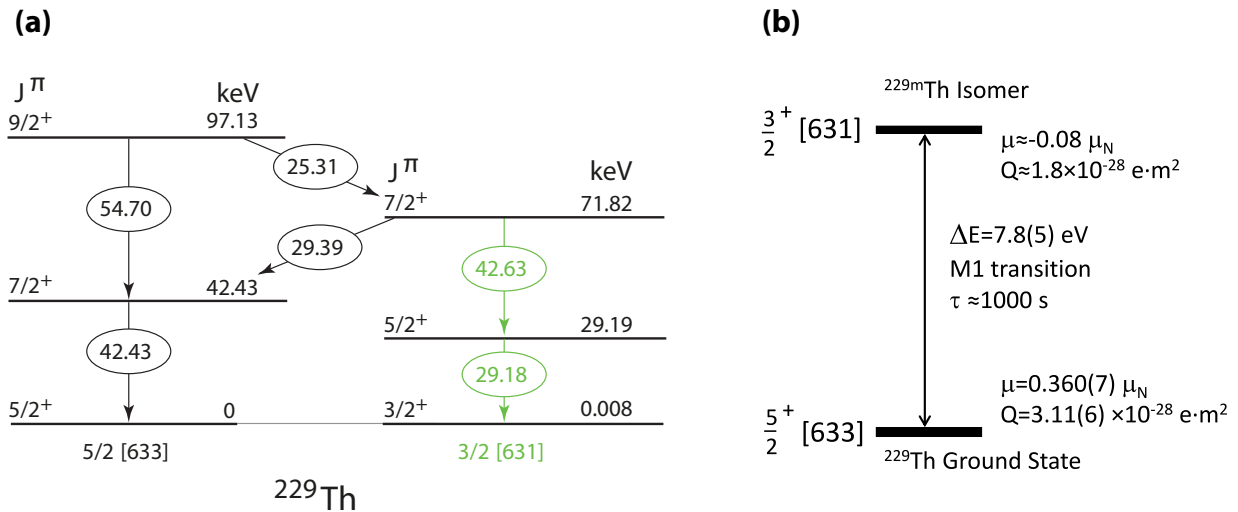


Figure 1.3 (a) Partial level scheme of ^{229}Th with the two rotational bands displayed in different color. The isomer energy of $7.8 \pm 0.5 \text{ eV}$ was determined by differencing the sum energies of the two decay paths leading to the ground state (bottom left) and first excited state (bottom right), starting at the common level of 71.82 keV . Reproduced from [1]. (b) Details about the ground state, lowest excited state and isomer transition. Reproduced from [3].

Failure to directly detect the transition can be explained by several complications:

Any kind of fluorescence detection suffers from the fact that ^{229}Th is an alpha emitter with a half-life of 7880 years, which causes a large signal background due to radioluminescence, Tscherenkow radiation or other spurious signals related to the (high-energy) radioactive decay products. In contrast, the useful signal is very small, owing to the long lifetime of the isomer state.

Optical excitation is generally not efficient, due to the low scattering cross section (of the magnetic dipole transition - see Fig. 1.3(b)) estimated around 10^{-21} cm^2 (in comparison to, e.g. rubidium with $\sigma = 10^{-9} \text{ cm}^2$). For direct excitation with a tunable narrow-band laser (which would also enable absorption detection, and thereby improve the signal to noise ratio), the search region of $\pm 10 \text{ nm}$ would be prohibitively large compared to the small linewidth, let alone the fact that such a tunable light source currently does not exist. Broadband excitation (e.g. by high intensity synchrotron radiation) is possible for a solid state sample. Since the transition energy lies above the first ionization energy of thorium (6.31 eV), it is necessary to work with the ion. This can be realized by doping a UV-transparent host crystal with thorium atoms, such that they form a suitable ionic bond. In that respect, it is also worth noting, that the chemically purified thorium-229 required for the doping, is very expensive to obtain.

A cheaper (and potentially simpler) approach in the experimental search for the transition, is to populate the isomer state via the decay from uranium-233 with a branching ratio (probability that the decay product thorium-229 ends up in the excited isomer state) of 2 percent. A very simple attempt to mitigate the even stronger radioluminescence background of this method, is to collect thorium nuclei, ejected from a sample by the

uranium alpha decay recoil, on an absorber (such as CaF_2 or MgF_2) which is then quickly transferred to a physically separated detector. Nevertheless, this method does not provide separation from other daughter products in the uranium decay chain, such that all experiments still failed to produce reliable results due to signal to noise constraints. Based on a much more sophisticated implementation of the isotope purification, using a gas buffer cell, beam forming stage, and a quadrupole mass-separator, this approach was recently successful [14]. However, the decay of the isomer state could only be detected via the (much faster) non-radiative decay path of internal conversion (where the energy is transferred to an outer electron in the shell). This process is usually suppressed for thorium ions, and is triggered in the experiment upon direct contact with the detector surface.

Yet another approach is based on ion traps, where an excitation transfer from the shell to the nucleus should be feasible, together with indirect detection of the isomer de-excitation via changes in the hyperfine structure [15].

In our group, we work with thorium nuclei embedded in a UV-transparent calcium fluoride (CaF_2) host crystal matrix, which is intended to realize a miniaturized, robust, solid-state frequency standard [16–17]. The necessary VUV probe lasers could eventually become available based on the new nonlinear crystal potassium beryllium fluoroborate (KBBF) [18].

Besides the discussed practical usefulness as a frequency standard, coherent control of a nuclear transition via laser excitation is also exciting from a purely fundamental research point of view. It is expected, for example, that the delicate balance of coulomb interaction and strong nuclear force leads to an enhanced sensitivity of isomer transition to eventual time-dependent variations of fundamental constants (like the fine structure constant α), compared to other measurements of that kind [19].

2 Spectroscopy with an optical frequency comb

2.1 Optical frequency comb basics

2.1.1 Modelocked femtosecond lasers

An optical frequency comb is an optical spectrum which consists of (several millions) of perfectly equidistant lines of known frequency which can be used as a “ruler in frequency space” for metrological applications (among others). Typically such spectra are generated by femtosecond mode-locked lasers¹³ producing periodic trains of ultrashort (that is, broadband) pulses [6, 20–22].

The term “mode-locked” refers to a frequency-domain description of the laser resonator: In the simplest case (free-running regime) a laser starts to oscillate on several of its approximately¹⁴ evenly spaced eigenmode frequencies (compare Ch. 3.2.2) within the gain bandwidth. However, the generally random phases of these modes lead to a messy periodic¹⁵ signal of dense irregular pulses. To concentrate its average power in one well-defined pulse per period, a more ordered (e.g. linear) phase relationship between individual modes is required, which can be provided by an additional nonlinear “mode-locking” mechanism inside the resonator [23]. Although conceptually instructive, following this line of argumentation makes it hard to explain how the known comb spectrum with *perfectly* even line spacing emerges¹⁶.

The phenomenon is much easier to understand through reasoning in the time-domain. For femtosecond lasers, the modelocker is basically a passive mechanism that leads to a higher net gain for short pulses inside the cavity, by introducing additional losses, which decrease for high (instantaneous) intensity. Since lasing is always started by random light bursts, we can imagine a beam with some spiked spatial intensity profile being present within the cavity. Due to the modelocker, the spike of highest intensity will experience the highest gain, so that its growth and stabilization is favored, leading (after several round trips) to a single pulse oscillating inside the cavity. The same mechanism will increasingly narrow this pulse, thanks to the tendency of increasing the pulse peak and decreasing its wings.

¹³ The meaning of the term “frequency comb” is colloquially extended to also denote the generating mode-locked laser itself.

¹⁴ The spacing is given by the free spectral range $\Delta\nu_{\text{FSR}} = c/(Ln_g)$ where L is the length of a total cavity roundtrip and n_g is the group index of the medium inside the cavity. However, the latter is usually frequency-dependent (due to chromatic dispersion). Additional frequency-dependent terms would need to be added to consider contributions by different media inside the cavity as well as dispersion effects in the mirror substrates. For this reason, the eigenmode frequencies are not strictly equidistant in practice. (See Chap. 3.2.2 for a more complete treatment in the context of passive cavities.)

¹⁵ The period is given by $1/\Delta\nu_{\text{FSR}}$.

¹⁶ In fact, the concept of resonator modes becomes somehow obsolete in the presence of strong nonlinearities. Since they would actually start to depend on the current intracavity field, a description in terms of the above “cold cavity modes” cannot be fully accurate anymore.

Competition with other processes - most importantly pulse broadening due to the finite amplifier bandwidth¹⁷ - puts a limit to the steady-state pulse duration which is finally reached.

The modelocker can be a fast saturable absorber - exactly fulfilling the above definition through nonlinear absorption - or it can be an indirect mechanism like the even faster Kerr-lens effect, necessary to realize sub-20 fs pulses. A saturable absorber can be a two-level system with a transition energy matching the laser wavelength, like certain dyes. A sufficiently intense field brings the excited level population close to the ground level population, at which point absorption and stimulated emission processes start to compensate each other, so that the medium tends to become transparent. A similar effect can be realized using very common semiconductor saturable absorption mirrors (SESAM) where Pauli blocking forbids further absorption once the valence band is depleted by raising all electrons into the conduction band.

Kerr-lens mode-locking uses a nonlinear medium having an intensity-dependent refractive index (Kerr effect) which - in combination with the inhomogeneous transverse intensity profile of a (Gaussian) beam - leads to a thermal lens effect and stronger focusing of high-intensity beams. This geometrical effect can be used to indirectly introduce additional loss for the low-intensity beam by attenuating it with an aperture, or by tuning the cavity parameters for selective resonant enhancement of the high-intensity mode.

Every time the circulating pulse inside the laser cavity hits the output coupling mirror, an attenuated copy of it is emitted, so that the laser output consists of a train of pulses separated by the cavity round trip time T . If those pulses would be all exactly identical, the frequency-domain representation of the pulse train would be given by a Fourier series of frequencies that are all integer multiples of the inverse round-trip time, or repetition rate ω_r (Eq. 2.1b). However, due to chromatic dispersion inside the cavity leading to a difference between phase and group velocities, there will typically be a changing phase shift between the pulse envelope and the carrier wave. Since the laser output is coherent (meaning that the emitted pulses - originating from the single circulating pulse - have a fixed phase relationship), this phase shift will always be the same from pulse to pulse. Only the phase shift modulo 2π , called the *carrier envelope (offset) phase* (CEO phase) $\Delta\varphi$ is of interest. As illustrated in Fig. 2.1 this leads to a shift of the periodic frequency spectrum by the *carrier envelope (offset) frequency* ω_0 so that each “line” is given by the fundamental equation 2.1a.

$$\omega_n = \omega_0 + n\omega_r \quad (2.1a)$$

$$\omega_r = \frac{1}{T} \quad (2.1b)$$

$$\omega_0 = \frac{\Delta\varphi}{T}. \quad (2.1c)$$

¹⁷ Here we do have to think of the pulse frequency spectrum, and note that the inverse relationship between pulse duration and spectral bandwidth only allows pulses of a certain minimum length to be supported by stimulated emission in the active medium.

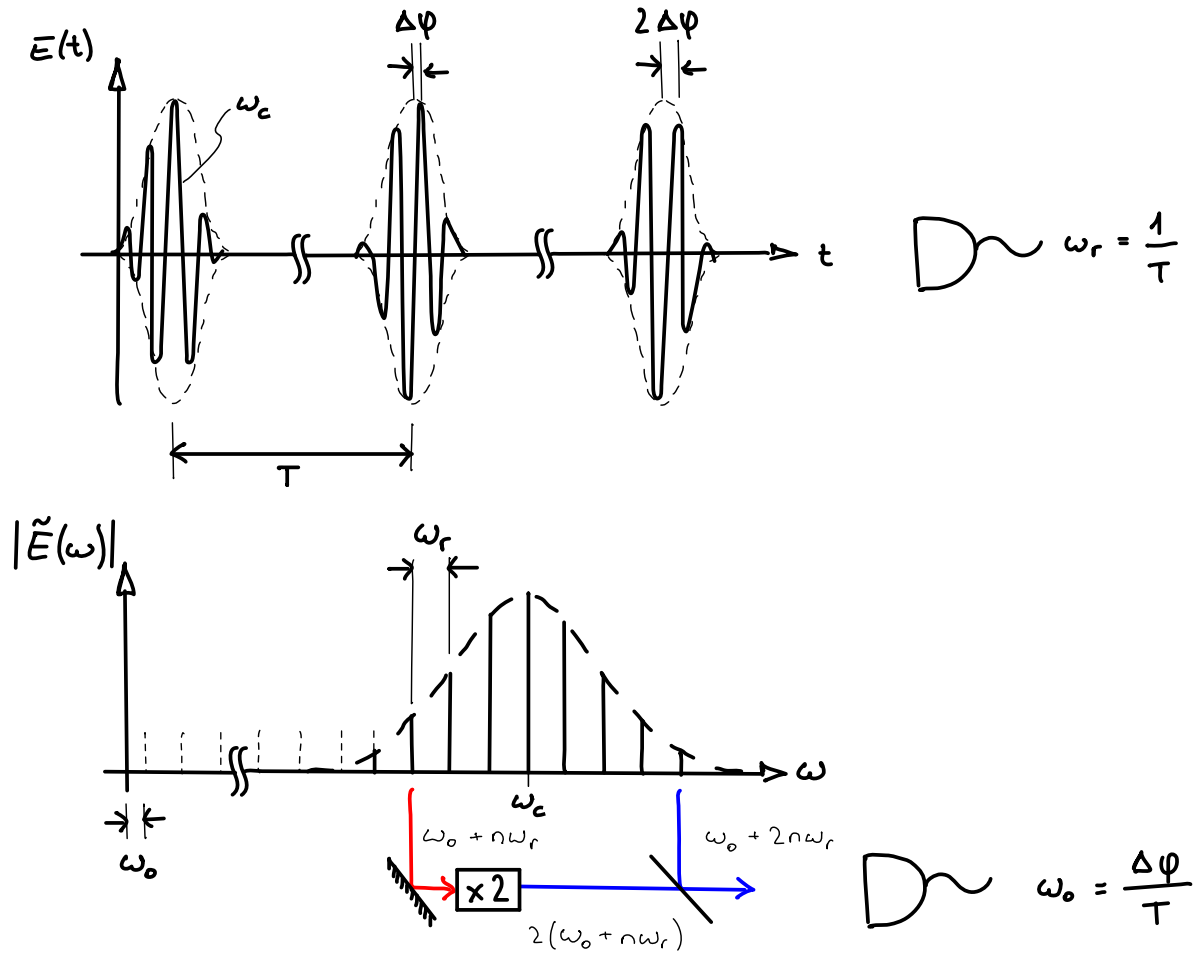


Figure 2.1 Relation between time and frequency-domain representations of a modelocked femtosecond oscillator. The main relations between the respective parameters are summarized in Eq. 2.1. The spectrum is centered around the carrier frequency ω_c and the spectral width (width of the spectral envelope) is inversely related to the pulse duration (width of the pulse envelope). The two degrees of freedom (ω_0 and ω_r) can be measured using two photodiodes (see Chap. 2.1.2). The line spacing is greatly exaggerated for illustration purposes.

The aforementioned shift of the frequency spectrum is obvious when mathematically describing the pulse train as product of a carrier wave of frequency ω_c and a periodic envelope function $A(t)$ (Eq. 2.2a) which can be written as a Fourier series with terms $n\omega_r$ (Eq. 2.2b).

$$E(t) = A(t)e^{-i\omega_c t} \quad (2.2a)$$

$$= \left(\sum_n A_n e^{-in\omega_r t} \right) e^{-i\omega_c t} \quad (2.2b)$$

$$= \sum_n A_n e^{-i(\omega_c + n\omega_r)t}$$

The simple relation Eq. 2.1c follows by comparing the last two lines of Eq. 2.3.

$$\omega_0 = \omega_c \bmod \omega_r \quad (2.3a)$$

$$\omega_0 T = \omega_c T \bmod \underbrace{\omega_r T}_{2\pi} \quad (2.3b)$$

$$\Delta\varphi = \omega_c T \bmod 2\pi \quad (2.3c)$$

While individual lines of a comb in the visible spectral range have frequencies of up to 100 THz, their spacing (given by typical cavity lengths of a few meters) is typically on the order of 100 MHz. The gain bandwidth of the laser medium (up to 300 nm for Ti:sapphire) determines the spectral width of the emitted pulses, relating to typical pulse lengths of a few tens of femtoseconds (Chap. 2.2.1), which implies the availability of a few million comb lines with exactly defined frequency.

In practice, building a good femtosecond oscillator is of course a bit more involved, with a delicate interplay of several processes like saturable gain, dispersion, self-phase modulation, self-amplitude modulation and mode coupling to consider. Especially for sub 20-fs pulses very precise dispersion management inside the resonator is required, through use of specially dielectric coated mirrors with controlled (negative) group delay dispersion (see Chap. 2.2.1). However, the important fact to stress is that, although such measures serve to make the pulse generation process possible at all, more efficient or more stable, they don't directly influence the intrinsic precision of the emerging comb line spectrum.¹⁸

2.1.2 Frequency comb stabilization

The frequency comb spectrum according to Eq. 2.1a is determined entirely by the two parameters ω_0 and ω_r . Both need to be measured and referenced to a known (radio frequency) standard (like a cesium clock) via an active feedback loop, to define the comb spectrum in absolute numbers. The repetition rate ω_r can be easily measured via a fast photodiode. The associated control variable is the resonator length. The offset frequency ω_r is not so easily accessible - it can be measured using a self-referencing scheme known as a *f2f-interferometer*¹⁹ illustrated in Fig. 2.1. A line from the low-frequency spectral part with frequency $\omega_0 + n\omega_r$ is frequency-doubled via second harmonic generation (SHG) in a nonlinear crystal to yield a signal of frequency $2(\omega_0 + n\omega_r) = 2\omega_0 + 2n\omega_r$. This signal is mixed with the closest frequency component $\omega_0 + 2n\omega_r$ from the original comb spectrum. The difference-frequency, which is detectable as a beat note on a photodiode, is exactly the offset frequency ω_0 . In practice, it would be hard to isolate individual comb lines for the process, so an entire low-frequency region of the spectrum is frequency-doubled

¹⁸ If it wouldn't be for that fundamental difference between engineering a great cavity and the previously described pulse forming in the active lasing process, one could directly use the resonance frequencies of a simple two-mirror optical cavity as absolute frequency markers of an "optical frequency comb".

¹⁹ The invention of the f2f-interferometer scheme was actually the crucial step in the realization of frequency comb technology, awarded with the Nobel Price in 2005.

and mixed with the entire comb spectrum. Since the preceding equations are correct for every value of n , this is however not an issue. If anything, the contribution of several line pairs with the same difference frequency causes the detectable beat signal to increase. By applying a low-pass filter to the diode signal to remove other beat frequencies larger than half the repetition rate (caused by pairs of “non-neighbouring” lines), its output can be directly used as the instantaneous value of ω_0 in the feedback loop. Feedback can be implemented via mechanisms which influence the dispersion inside the laser resonator (see Chap. 2.3). The only requirement for this scheme to work, is an octave-spanning spectrum of the comb. Given their broad gain bandwidth²⁰, this is in principle possible to realize with Ti:sapphire lasers [24]. If not available directly from the femtosecond oscillator, broadening of the spectrum can be achieved efficiently via self-phase modulation inside nonlinear fibers [25].

2.1.3 Frequency metrology with a comb

The most obvious use of a frequency comb is as a “ruler in frequency space” (Fig. 2.2). The frequency of a narrow bandwidth laser can be determined via an optical heterodyne detection, using a nearby comb line as a reference oscillator. The laser frequency ω is then given by the fundamental equation

$$\omega = \omega_0 + N\omega_r + \Delta\omega \quad (2.4)$$

where we define $\Delta\omega$ as ω minus the frequency of the closest comb line. Two difficulties arise in order to complete a measurement - the signs of both $\Delta\omega$ and ω_0 are not directly accessible, and the index N has to be figured out.

Measuring the lowest-frequency ($\leq \omega_r/2$) beat note with a photodiode, determines the absolute value of $\Delta\omega$, but not its sign. (There is no indication which one of the two involved frequencies is higher.) The same actually applies for the self-referenced measurement of the offset frequency ω_0 . However, the signs can quickly be determined by observing the change of $|\Delta\omega|$ for slight changes of ω_0 and ω_r . To this end, it is helpful to imagine the comb spectrum in Fig. 2.2 as a “rubber band” with frequency markers. Changing ω_0 corresponds to a translation of the band, while changing ω_r is equivalent to fixing it at ω_0 and pulling at the high-frequency end. The algorithm is as follows:

- Determining the sign of $\Delta\omega$: If $|\Delta\omega|$ decreases when ω_r is increased, then $\Delta\omega$ is positive - otherwise it is negative.
- Determining the sign of ω_0 , depending on the previous result:
 - If $\Delta\omega$ is positive: If $|\Delta\omega|$ decreases when ω_0 is increased, then ω_0 is positive - otherwise it is negative.

²⁰ The laser in Ref. [24] barely covers the range of 600 nm to 1200 nm at a level of 10^{-14} of the peak spectral density. Covering the same range within the FWHM of a Gaussian intensity spectrum, would correspond to a Fourier-limited pulse length on the order of one femtosecond (compare discussion of time-bandwidth product in Chap. 2.2.1).

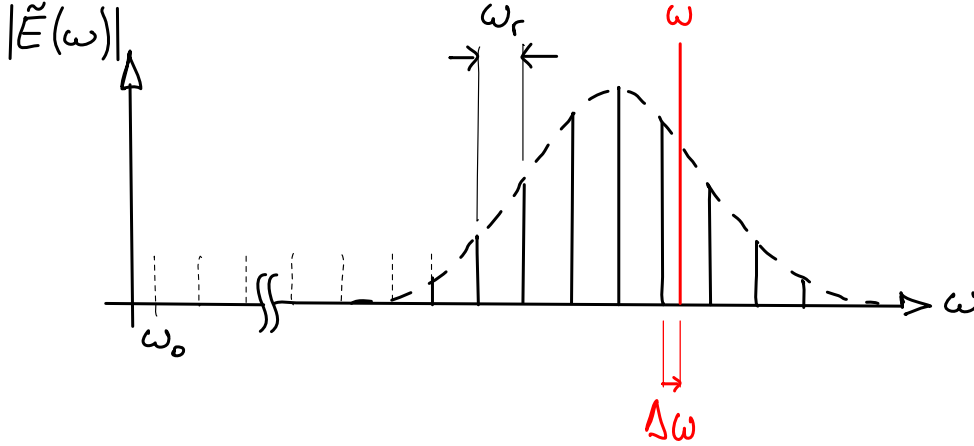


Figure 2.2 Measuring an unknown laser frequency. Over the entire bandwidth of the comb, there is always a reference line close enough to produce a beat note in the radio-frequency regime. The index of the closest line, and the sign of the frequency difference are not known a priori, but can be determined by combining different measurements for varying comb parameters.

- If $\Delta\omega$ is negative: If $|\Delta\omega|$ increases when ω_0 is increased, then ω_0 is positive - otherwise it is negative.

Several options exist to determine N : If a wavemeter of sufficient resolution is available to constrain ω to a precision of at least half the repetition rate in an independent measurement, N is immediately known. Otherwise N can be determined from two separate measurements of $\Delta\omega$ using different repetition rates. The equations

$$\omega = \omega_0 + N_1\omega_{r1} + \Delta\omega_1 \quad (2.5a)$$

$$\omega = \omega_0 + N_2\omega_{r2} + \Delta\omega_2 \quad (2.5b)$$

can be rearranged to

$$N_2 = N_1 \frac{\omega_{r1}}{\omega_{r2}} + C, \quad N_1, N_2 \in \mathbb{N} \quad (2.6)$$

where the constant C is given by

$$C = \frac{\Delta\omega_1 - \Delta\omega_2}{\omega_{r2}}.$$

A set of possible integer solutions to N_1 and N_2 can be determined from Eq. 2.6 as illustrated in Fig. 2.3. Technically, the smaller the difference between the two chosen repetition rates, the larger the difference between resulting valid solutions for N_1 and N_2 , which makes it easier to select the physically correct solution based on other information (e.g. low-resolution spectral analysis). However, the uncertainty in the measurement of $\Delta\omega$ (mainly given by the frequency stability of the measured laser over the timespan needed to complete the measurement procedure), imposes a limit on the minimum difference

$\omega_{r2} - \omega_{r1}$. If it is chosen too small, “clusters” of values for N (instead of single, separate ones) emerge as mathematically correct solutions, making discrimination among them impossible. For this reason, the measurement scheme fails entirely if the measurement uncertainty of $\Delta\omega$ approaches a value of half the repetition rate. A possible workaround to measure such instable lasers is to use a comb with larger repetition rate, or to use another more stable laser that can be tuned close to the unknown laser as an intermediate step. This auxiliary laser can then be calibrated by (or locked to) the frequency comb, while using it to measure the (fluctuating) beat note with the unknown laser - removing any ambiguity in the result.

A similar application of frequency combs is *optical frequency division*. Instead of referencing ω_0 and ω_r of the comb to an RF standard (like a cesium clock), an optical reference transition can be used to absolutely define the comb by locking a comb line to it (and stabilizing the offset frequency to zero or a fraction of the repetition rate). The comb then serves to divide the optical reference frequency by a factor of up to N , supplying a phase-locked RF signal, which can be used to exactly count the number of oscillation periods of the optical reference. This is exactly the “optical clockwork” needed to use and compare new optical frequency standards like the proposed clock based on thorium-229.

2.1.4 Direct frequency comb spectroscopy

Another application of optical frequency combs is to use them directly as an advanced light source to do (e.g. molecular) spectroscopy, where one could think of them as “a million narrow-linewidth stabilized continuous wave lasers” available for (potentially one-shot) high-precision measurements over a broad spectral range.

One strategy is to record the absorption signal of a sample, integrated over the entire bandwidth with a photodiode, repeat the measurement with changes to the offset or repetition frequency and try to computationally deconvolve the original absorption spectrum from the measurement series. For complicated spectra, it is unfortunately very likely that this deconvolution can’t be done unambiguously. This problem can be circumvented by doing a more sophisticated spectrally resolved analysis of the transmitted light in each of those individual measurements. The resolution only has to be sufficiently good to discriminate and identify the individual comb lines and to read out their amplitudes (which are modulated by the shape of the absorption spectrum). The order of magnitudes higher resolution of the final result is founded in the extraordinary precision to which the frequencies of the narrow comb lines are known. Several methods are available:

- In Fourier transform spectroscopy (FT, commonly used in the infrared as FT-IR) the spectrum is obtained by computing the Fourier transform of a first-order autocorrelation signal of the transmitted electric field, acquired by scanning one arm of a Michelson-Morley interferometer.
- A dispersive spectrometer like a virtually imaged phased array (VIPA) spectrometer can be used, if ω_r is large enough to resolve the individual comb lines. The line

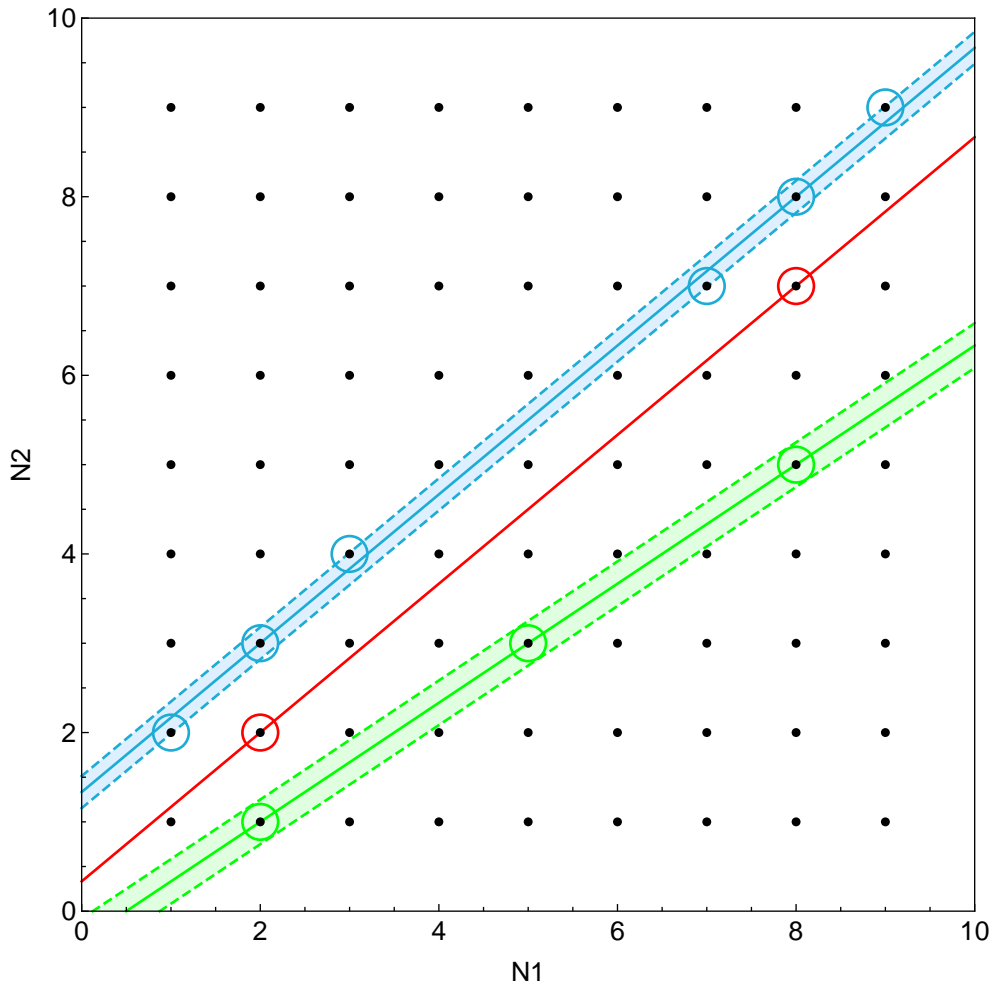


Figure 2.3 Graphical representation of comb line indices agreeing with the measurement. The relation between N_1 and N_2 from two different measurements defines a line according to Eq. 2.6. Possible solutions (open circles) are given by intersection points on the integer grid. The steepness of the line is given by the ratio of the two repetition rates. The red line has an angle of almost 45° relative to the axes, corresponding to very similar repetition rates, which leads to a large separation of the possible solutions for N_1 and N_2 . Consequently the mathematically possible solutions for ω will have a large difference according to Eq. 2.5, which makes it easy to select the physically correct solution among them (based on other criteria or measurements). However, at that angle, already a small uncertainty in the measured beat notes (typical fluctuation over the time of the two measurements) can lead to an ambiguous result, where directly neighboring solutions for N exist, as illustrated by the blue line. A larger difference between the repetition rates and less steep (green) line leads to a smaller distance between possible solutions in the best case, but can accept a larger measurement uncertainty.

separation can be increased by passing through a Fabry-Perot cavity of appropriate length to only transmit every n -th comb line.

- In dual comb spectroscopy, the light transmitted by the sample is analyzed using a second frequency comb with slightly different repetition frequency. The second comb

acts as a highly multiplexed heterodyne receiver, downconverting each line of the sampling comb to the radio frequency range where it can be analyzed using an (electronic) spectrum analyzer²¹. Compared to FT spectroscopy, recording times are considerably shortened, because no moving parts are required.

Compared to conventional spectroscopy with a tunable single-mode laser, a disadvantage of direct frequency comb spectroscopy is however the limited power per comb line, since the average power is divided between all (about 10^6) of them. This issue can partly be overcome through use of enhancement cavities, increasing the detection efficiency. Frequency combs are naturally perfectly suited for this method, since their comb structure often allows enhancement over their full spectral bandwidth inside a cavity with sufficiently low GDD (see Chap. 3.2.2). For this particular reason, frequency combs are even used as a general broadband light source in spectroscopy applications that are not interested in high-precision comb-mode resolved measurements as discussed above. By comparison, an incoherent light source with a continuous spectrum (“lamp”) can not be efficiently enhanced inside a cavity, since the overwhelming part of the spectral power will not be resonant. The use of enhancement cavities also opens the way for detection schemes like ring-down cavity spectroscopy, which can additionally improve the signal-to-noise ratio (SNR) of such measurements by orders of magnitude.

2.2 Short pulse diagnostics

2.2.1 Group delay dispersion, pulse chirp and transform limit

So far, only the amplitudes of individual frequency components in the emerging comb spectrum have been considered (compare Fig. 2.2). For a full description of the laser pulses in frequency domain, it is however necessary to take their relative phases into account as well, which will explain effects like pulse broadening and pulse chirp.

The effect of linear (superposition principle holds) and time-invariant processes on the spectrum can be described by a simple phase and amplitude change (complex multiplication factor) of each frequency component, since it follows from above preconditions that a sinusoidal input always yields a sinusoidal output of the same frequency, allowing no intermodulation²². It is instructive to look at a short proof of this fact, considering a

²¹ The slight offset of the two repetition rates is essential, since the shifting beat frequency for successive line pairs encodes their index position in the resulting RF spectrum. The fixed downconversion factor is given by $(\omega_{r1} - \omega_{r2})/\omega_{r2}$.

²² This also explains why frequency conversion processes like harmonic generation, sum and difference frequency generation, parametric oscillation or supercontinuum generation are only possible for a nonlinear system response, falling within the framework of nonlinear optics.

As a sidenote: The detection of a difference-frequency beatnote (as discussed in Chap. 2.1.2) is entirely different from difference frequency generation, and has nothing to do with optical nonlinearities. In the latter case a new frequency appears in the optical spectrum. In the former case, the optical field is just presented in time domain as a product (not the sum) of sum and difference of the individual frequency

sinusoidal input signal $u(t) = e^{i\omega t}$, its time-shifted version $u_\Delta(t) = e^{i\omega(t+\Delta)}$ and a linear time-invariant operator L . It holds that:

- $L[u_\Delta](t) = e^{i\omega\Delta} L[u](t)$ by linearity with respect to the constant $e^{i\omega\Delta}$.
- $L[u_\Delta](t) = L[u](t + \Delta)$ by time invariance of L .

We can therefore set $L[u](t + \Delta) = e^{i\omega\Delta} L[u](t)$ and perform a variable change $\tau = t + \Delta$ to see that $L[u](\tau) = e^{i\omega\tau} L[u](0)$, which completes the proof.

Many processes primarily lead to a change of the spectral phase (apart from some small overall attenuation of the intensity spectrum) due to frequency-dependent phase velocity and/or different optical path lengths for different frequencies. This includes propagation of light inside dispersive (but linear) transparent media, reflections from dielectric mirror coatings or very deliberate phase changes inside a prism compressor. Fig. 2.4 illustrates how different spectral phases $\varphi(\omega) = \arg(\tilde{E}(\omega))$ effect the time-domain representation $E(t)$ of a pulse, according to the Fourier transform pair²³:

$$E(t) = \int_{-\infty}^{\infty} \tilde{E}(\omega) e^{-i\omega t} d\omega. \quad (2.7a)$$

$$\tilde{E}(\omega) = \frac{1}{\sqrt{2\pi}} \int_{-\infty}^{\infty} E(t) e^{i\omega t} dt. \quad (2.7b)$$

The spectral phase $\varphi(\omega)$ is distinguished according to terms of different order in its Taylor expansion around a central frequency ω_0 :

$$\varphi(\omega) = \varphi_0 + \frac{\partial\varphi}{\partial\omega}(\omega - \omega_0) + \frac{1}{2} \frac{\partial^2\varphi}{\partial\omega^2}(\omega - \omega_0)^2 + \frac{1}{6} \frac{\partial^3\varphi}{\partial\omega^3}(\omega - \omega_0)^3 + \dots$$

The names of these terms originate from the general case of propagation in a homogeneous medium, where individual frequency components evolve according to $\sin(k(\omega)x - \omega t)$ with frequency-dependent phase velocity $c(\omega) = \omega/k(\omega)$ and the spectral phase given directly by the wavenumber $k(\omega)$ times the propagation distance:

components, which stay unchanged. The difference frequency is then actually measured as an electronic signal, because the intensity measurement itself (that is, the conversion to a time-averaged square of the electric field by the photodiode) is a nonlinear transformation.

²³ The electric field $E(t)$ is a real-valued function, such that its complex Fourier transform possesses the symmetry $\tilde{E}(\omega) = \tilde{E}^*(-\omega)$. The complex exponentials $\exp(-i\omega t)$ and $\exp(i\omega t)$ (clockwise and counter-clockwise phasor) always add up in pairs to a real-valued sinusoid of frequency ω . If these “negative frequencies” of the frequency spectrum $\tilde{E}(\omega)$ are neglected in the mathematical formalism, its inverse Fourier transform $E(t)$ will have an imaginary part (which then has to be ignored). However, negative frequencies can get a physical meaning and come in handy e.g. to intuitively understand how the two modulation sidebands appear in amplitude modulation (AM), when imagining the process as folding the spectra of a low-frequency signal and a high-frequency carrier wave.

- The zero-order term describes a common phase shift, which effects the carrier envelope offset.
- The first-order (linear) term leads to a translation in the time domain²⁴ by the group delay (GD) T_g :

$$\frac{\partial \varphi}{\partial \omega} = x \frac{\partial k}{\partial \omega} = \frac{x}{v_g} = T_g.$$

- The second-order (quadratic) term leads to pulse broadening and a linear pulse chirp²⁵ (linear change of the instantaneous carrier frequency over time) in the time domain. Since it is also the derivative of the group delay with respect to the angular frequency, it is called the *group delay dispersion* (GDD), typically given in fs²:

$$\frac{\partial^2 \varphi}{\partial \omega^2} = \frac{\partial T_g}{\partial \omega}.$$

If the GDD is specified as a material parameter per unit length, it is similarly called the *group velocity dispersion* (GVD), defined as the derivative of the inverse group velocity with respect to the angular frequency, typically given in fs²/mm.

- The third-order (cubic) term is called *third order dispersion* (TOD) and causes a non-linear pulse chirp (along with higher order terms).

Pulse broadening due to added second- or higher-order dispersion is an often unwanted effect. This is especially true in the context of external enhancement cavities (Chap. 3) where it poses a twofold problem: To achieve a high power density, pulses should already be as short as possible prior to the enhancement process. Inside the cavity pulse broadening is even more problematic, since it leads to an ever-increasing mismatch between circulating pulses. Very short femtosecond pulses are particularly “fragile” - being significantly distorted (broadened) by even small amounts of dispersion in standard optical components. Most optical media lead to a positive GDD, associated with a positive chirp (increase of the carrier frequency in time). It can be compensated for by anomalous (negative) dispersion in certain materials, or in specially engineered dielectric coatings of so-called “chirped mirrors”. A pulse with linear phase $\varphi(\omega)$ is said to be *transform limited*, since it realizes the shortest possible temporal duration for a given width (in frequency space) of the corresponding intensity spectrum, according to their inverse relationship given by the Fourier Transform. How close a pulse comes to this case, is often characterized by the product of those two values - the *time-bandwidth product* - which is roughly 0.44 for a Gaussian pulse, when based on the full width at half maximum (FWHM). It should be

²⁴ Time delay is illustrated in the Fourier transform of Fig. 2.4(f), and can be directly derived by observing that a time translation of each Fourier component by Δt according to $\exp(i\omega t) \rightarrow \exp(i\omega(t + \Delta t)) = \exp(i\omega t) \exp(i\omega \Delta t)$ leads to an additional phase $\exp(i\omega \Delta t)$ that is linear with frequency. This nicely motivates why the group velocity is actually defined as $v_g = \left(\frac{\partial k}{\partial \omega}\right)^{-1}$.

²⁵ Naming is by analogy to an acoustic “chirp” sound.

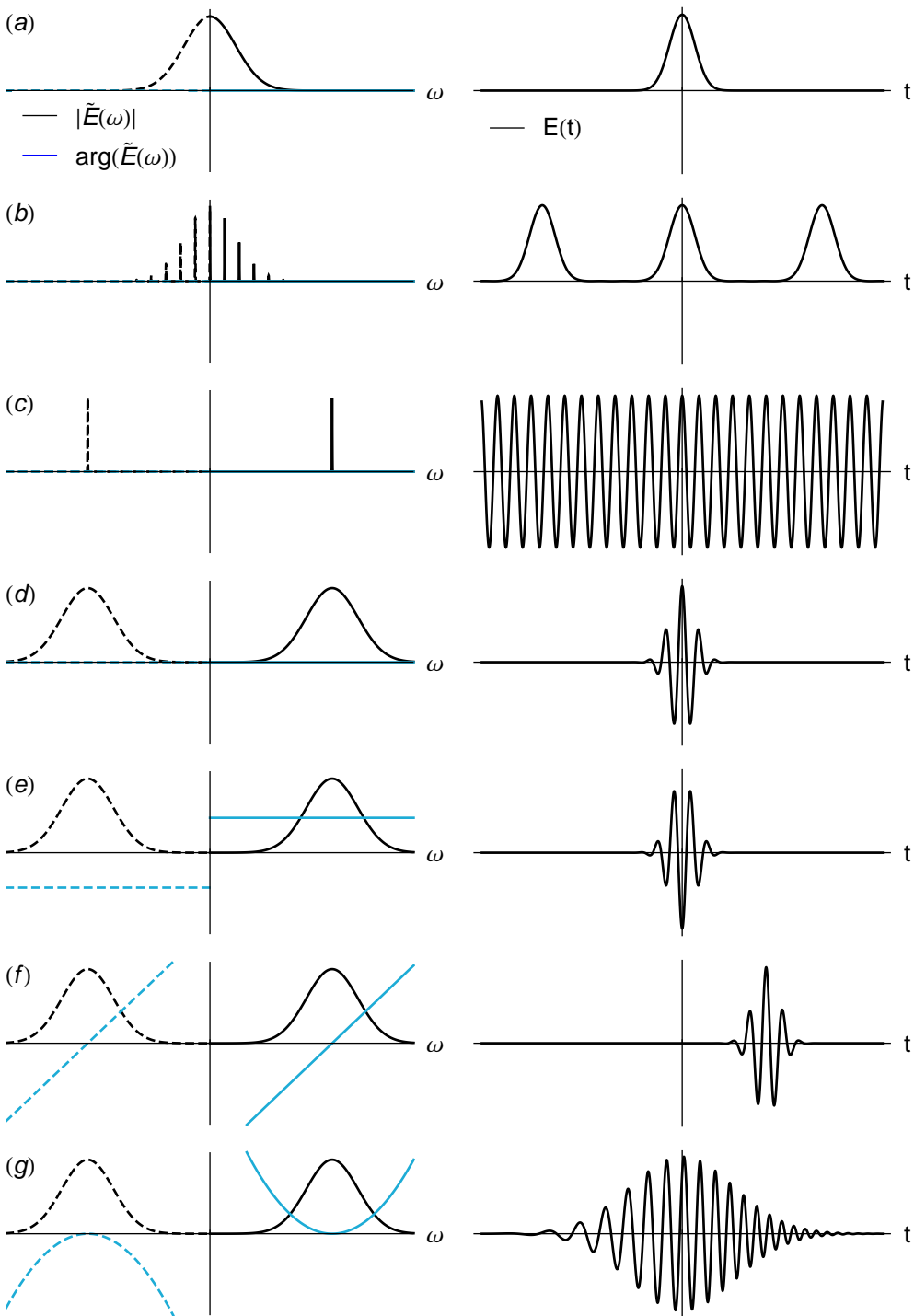


Figure 2.4 Correspondence between time- and frequency-domain representation of short pulses. The complex conjugate negative frequencies in the spectrum are dashed. (a) Gaussian envelope. (b) Periodic discretisation of the frequency spectrum of (a) leads to a periodic time domain signal. (c) Sine wave. (d) Transform-limited Gaussian pulse, resulting from a combination of (a) and (c) by multiplication in the time domain and folding in the frequency domain. (e) A constant phase shifts the carrier envelope offset. (f) A linear phase is equivalent to a translation in time without changing the pulse shape. (g) A quadratic phase leads to a broadened pulse with linear chirp.

noted, that dispersion does not lead to a distortion of a frequency comb spectrum, since only the spectral phase is affected.

2.2.2 SPIDER measurement scheme

Since no measurement equipment is fast enough to trace out the electric field of an optical pulse in the time domain, it can only be exactly characterized in the frequency domain. Once both intensity spectrum and spectral phase are known, the pulse shape can be reconstructed via a Fourier transform. The former can be easily measured using a spectrometer, while more complex schemes of *spectral interferometry* are necessary to derive the latter.

The basic principle of spectral interferometry involves the measurement of the intensity spectrum $|\tilde{E}(\omega)|^2$ resulting from the interference of two individual pulses with complex frequency spectra \tilde{E}_1 and \tilde{E}_2 , to derive information about their spectral phases. An essential detail is that one of the pulses is subject to a time delay τ which translates into an additional phase factor $\exp(-i\omega\tau)$. The measured intensity spectrum (interferogram) of the combined pulses is therefore given by:

$$\begin{aligned} |\tilde{E}(\omega)|^2 &= |\tilde{E}_1(\omega)e^{-i\omega\tau} + \tilde{E}_2(\omega)|^2 \\ &= |\tilde{E}_1(\omega)|^2 + |\tilde{E}_2(\omega)|^2 + 2|\tilde{E}_1(\omega)||\tilde{E}_2(\omega)| \cdot \underbrace{\cos(\varphi_2(\omega) - \varphi_1(\omega) + \tau\omega)}_{\varphi}. \end{aligned}$$

This is an oscillating function with an instantaneous angular frequency $\tau(\omega)$, according to the definition

$$\tau(\omega) = \frac{d\varphi}{d\omega} = \left(\frac{d\varphi_2}{d\omega} - \frac{d\varphi_1}{d\omega} \right) + \tau,$$

roughly given by the time delay τ and modulated by the group delay (first derivative of the spectral phase) difference of the two pulses. If the spectral phase of one pulse is exactly characterized, it can be used as a reference to reconstruct the spectral phase of the second pulse from the frequency variation of the interferogram²⁶.

The need for an external reference pulse can be eliminated by self-referencing the measured pulse. This can be achieved by generating two copies of the pulse and introducing a small frequency shift Ω between them (in addition to above time delay τ) before recording the interferogram, in a method called *spectral shearing interferometry*. The intensity spectrum is then given by

²⁶ A fit to the interferogram might be a naive method to extract this information. In practice, it is converted to pseudo-time via a Fourier transform (“pseudo”, because the phase information of the combined spectrum is not yet available) to extract the AC sideband, considering that the interferogram is a frequency-modulated carrier wave with carrier frequency τ .

$$\begin{aligned}
|\tilde{E}(\omega)|^2 &= |\tilde{E}_1(\omega)e^{-i\omega t} + \tilde{E}_2(\omega + \Omega)|^2 \\
&= |\tilde{E}_1(\omega)|^2 + |\tilde{E}_2(\omega + \Omega)|^2 + 2|\tilde{E}_1(\omega)||\tilde{E}_2(\omega + \Omega)| \cdot \underbrace{\cos(\varphi_2(\omega + \Omega) - \varphi_1(\omega) + \tau\omega)}_{\varphi}.
\end{aligned}$$

where the phase information now links the GD at frequencies ω to frequencies $\omega + \Omega$ so that its full reconstruction is possible (Fig. 2.5).

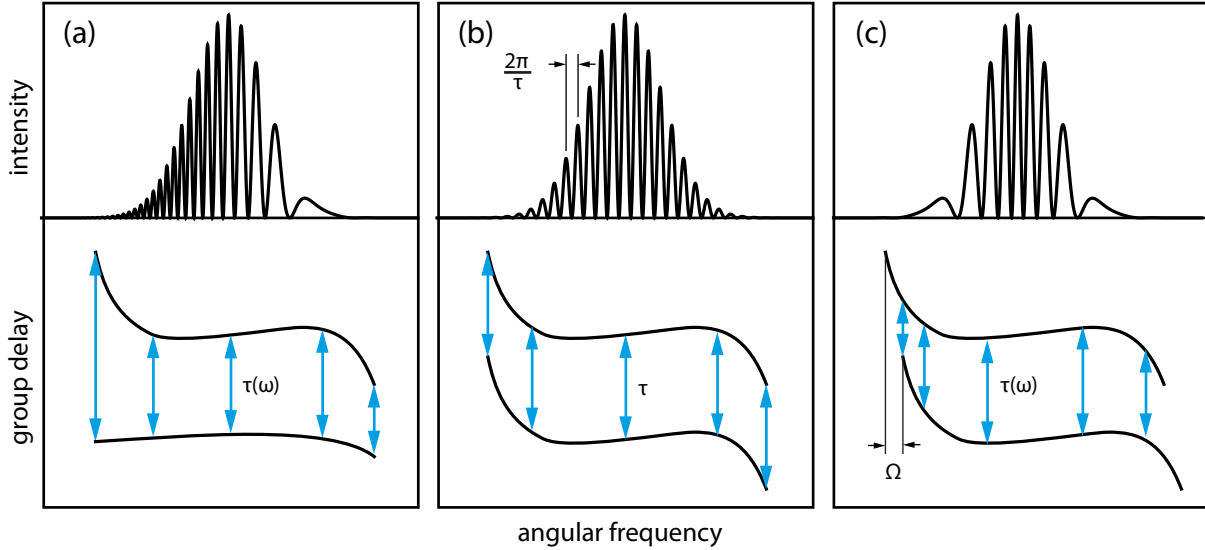


Figure 2.5 Spectral interferograms (top row) give access to the relative group delay $d\varphi/d\omega$ between two pulses (bottom row). (a) The spectral interferogram with a time-delayed reference pulse (bottom line) can be used to reconstruct the GD of the measured pulse (top line). (b) Two copies of the same pulse possess a constant relative phase - their interferogram with constant oscillation frequency contains no useful information. (c) Using the additional trick of frequency-shifting one of the pulse replicas allows self-referencing and reconstruction of the GD.

A robust practical implementation of this method is the *Spectral Phase Interferometry for Direct Electric-field Reconstruction* (SPIDER²⁷) [26], where the frequency shift is introduced by sum frequency generation in a nonlinear crystal, using mixing frequencies also derived from the pulse itself. The incoming pulse is split into three replica pulses. A significant temporal distance is introduced between two of them, so that they don't have any temporal overlap. The third one is strongly temporally broadened by sending it through a highly dispersive optical element, such as a long block of glass, and combined with the others in the nonlinear crystal. Since the two signal pulses overlap with different temporal portions of the chirped pulse, which have different optical frequencies, a spectral shear Ω between the two upconverted pulses (in the second harmonic frequency range) is introduced (Fig. 2.6).

²⁷ An APE FC SPIDER is available in our lab.

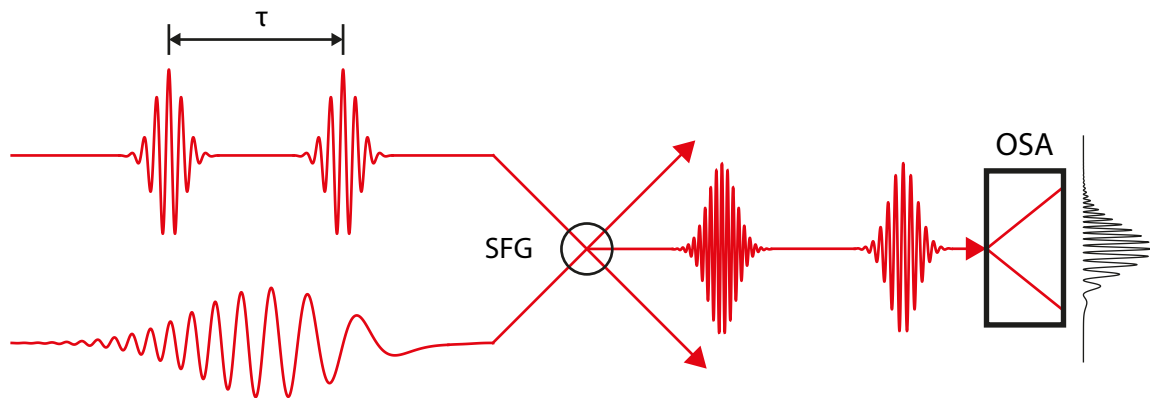


Figure 2.6 Spectral Phase Interferometry for Direct Electric-field Reconstruction (SPIDER) uses the following clever technique to achieve the spectral shear between the two pulse copies according to Fig. 2.5(c): Both pulses (top left) are frequency-shifted by a slightly different amount via sum frequency generation (SFG) in a nonlinear crystal. The different summing frequencies are derived from a third replica of the measured pulse itself, which is significantly stretched and chirped by a dispersive element. The short pulses both lie within the time window of the stretched pulse, however they interact with different parts of it (with different instantaneous carrier frequency) in the nonlinear crystal. The non-collinear SFG scheme makes it easy to isolate the resulting sum frequency pulses and guide them to an optical spectrum analyzer (OSA) which records the interferogram in a one-shot measurement. With the additional information of the intensity spectrum (recorded by a second OSA from a fourth pulse copy) the original pulse can be reconstructed in real time.

2.3 The Ti:Sa oscillator

The optical frequency comb setup used in our experiment (MenloSystems FC 8004) is based on a Kerr-lens mode-locked Ti:Sa femtosecond oscillator from FemtoLasers (Femtosource Scientific). It is pumped by the fundamental mode (TEM₀₀) from a frequency doubled Nd:YAG diode pumped solid state (DPSS) green laser at 532 nm (Coherent Verdi V8) with a maximum average power of 8 Watt.

The oscillator starts lasing in continuous wave operation - a small external cavity perturbation is needed to start mode locking, which is done by slightly moving one of the resonator mirrors via a rod guided to the outside of the enclosure. Initiation of mode locking can be observed through a brightness increase of the output and, most notably, disappearance of the speckle patterns. (The latter effect can be explained by the broad spectrum of the femtosecond pulses: Different speckle patterns form for each wavelength, so that the net contrast is greatly reduced [27].) The pulse train can also be observed on a fast positive intrinsic negative (PIN) photodiode (around 1 ns response time).

For roughly orthogonal control of both degrees of freedom of the generated comb spectrum, each of them has two actuators integrated with the oscillator (a slow, coarse, long-range and a fast, precise, short-range one). The repetition rate is controlled via the resonator length. The resonator end mirror is mounted on a piezo stack and a motorized translation

stage for this purpose. Coarse control of the CEO phase is realized via a pair of quartz glass wedges on a motorized translation stage, changing the amount of GDD inside the resonator. As the CEO is also sensitive to the pump power, an acousto optic modulator (AOM) is used for quick intensity modulation of the pump beam, by deflecting (and dumping) part of it into higher diffraction orders. The repetition rate is tunable between 108.056 and 108.529 MHz.

Coupling of the pump beam into the pre-aligned resonator needed at least weekly realignment via two external steering mirrors to reach the maximum average output power of 1 Watt. The output-coupler (OC) is wedged to prevent unwanted reflections from the rear side of the substrate which is additionally AR-coated. The angular dispersion introduced by the wedge is compensated by a compensating plate (CP) close to the OC. An extracavity chirped mirror pair is installed to compensate for GDD added by the OC and CP.

To achieve an octave spanning spectrum (Fig. 2.7) the effect of supercontinuum generation via self-phase modulation inside a microstructured nonlinear photonic crystal fiber (PCF) is exploited [25]. The 60 mm long PCF has a solid silica core with a diameter of approximately $2 \mu\text{m}$ surrounded by air holes and is spliced to a short piece of standard 780 nm fiber for easier incoupling. The fiber sits on a fixed mount. Two steering mirrors and an aspheric lens mounted on a (manually and piezo-actuated) three-axis translation stage are used for coupling to the fiber. The alignment procedure is best started by removing the collimation lens (microscope objective) after the fiber, to observe the initially faint transmitted signal, magnified at some distance on a piece of paper with an infrared viewer. A circular structure generated by light coupled to the fiber cladding is visible at first - the goal is then to maximize the signal within this region, indicating coupling to the fiber core. Once a certain power level is coupled in, straylight from the fiber appears in different colors (changing over the fiber length) due to the spectral broadening process. Interestingly, the spectrum generated by the PCF depends significantly on the orientation of the polarization axis (due to slight asymmetries in the fiber), requiring a half wave plate before the incoupling lens for finetuning.

An overview of the $f2f$ interferometer optomechanics and electronics is given in figures 2.8, 2.9 and 2.10. The two fast feedback loops for ω_0 and ω_r are referenced to an external 10 MHz source - a benchtop rubidium oscillator frequency standard (Stanford Research Systems FS725) in our case. A fixed 20 MHz signal is derived as a setpoint for ω_0 , while the repetition rate ω_r can be locked to a tunable frequency generated via a direct digital synthesizer (DDS).

To achieve long-term stable operation of the comb system, these fast feedback loops are complemented by computer controlled feedback loops which are slower, less precise but can access a broader parameter range. It is their job to keep the fast feedback loops from leaving their control range, by making occasional corrections to the slow actuators. Additionally a few other elements (like the half wave plate in one of the interferometer arms, the half wave plate in front of the fiber coupling lens, and the piezo stage of the lens itself) are remote controlled by the integrated control software, to maintain good

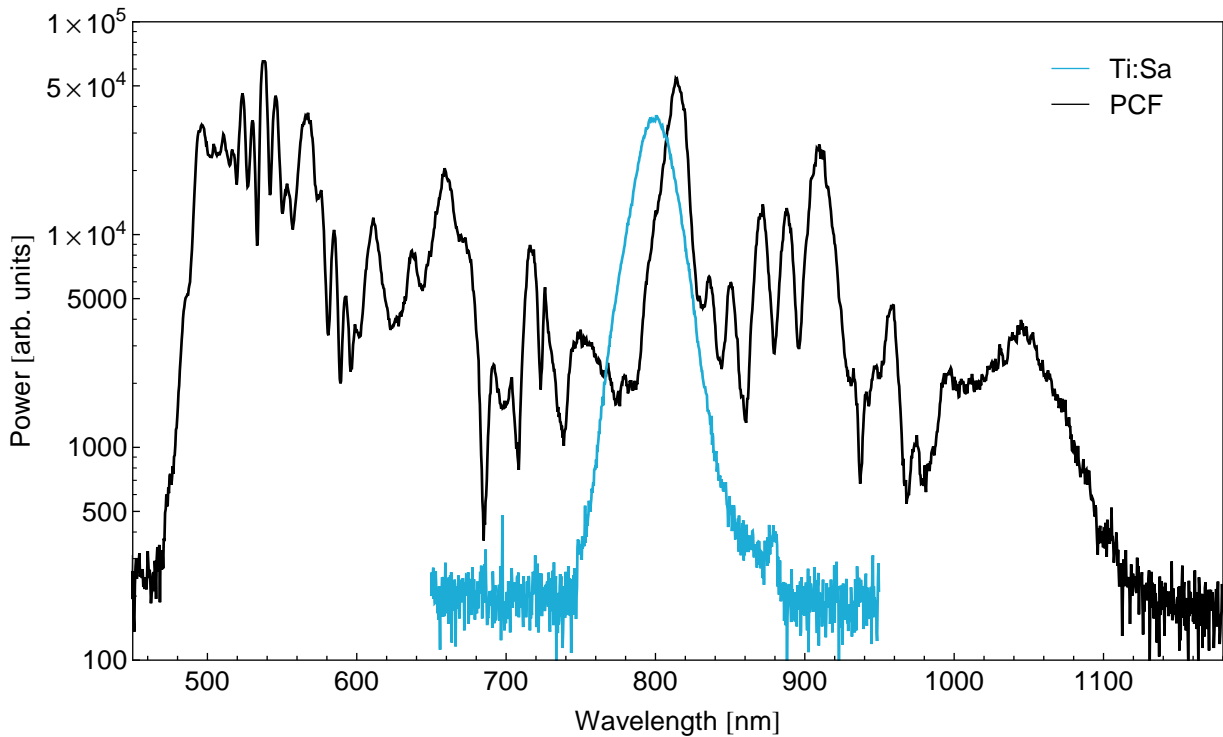


Figure 2.7 Spectrum of the Ti:Sa femtosecond laser before and after spectral broadening in the PCF fiber.

alignment and signal strength. This optimization is done according to a simple algorithm: At fixed time intervals (around 30 seconds), if the signal falls below a certain threshold, the individual actuators are changed in a random direction. If the signal increases, the direction is maintained in the next step, otherwise it is inverted.

2.4 Metrology experiments in the visible and near-IR spectrum

For high harmonic generation, the output of the Ti:sapphire femtosecond oscillator is directly routed to the passive enhancement cavity (Chap. 4), to make use of the maximum available power. Alternatively, the output can be routed to a second photonic crystal fiber, providing a broadened comb spectrum independent of the $f2f$ -interferometer, for metrology applications in the visible and near-IR spectral ranges.

The detection setup for typical beat note measurements is very similar to the $f2f$ -interferometer described in Fig. 2.8. If necessary, one of the beams should be attenuated, such that the interfering frequency components are of similar intensity. Precise spatial overlap of the beams is crucial, as is tuning of the half wave plate before the fiber which has a large influence on the final spectral distribution (Fig. 2.11).

2.4.1 Use of the comb as a real time high-precision wavemeter

In order to aid another (molecular spectroscopy) experiment, which required continuous frequency tracking of a tunable CW probe laser with precision better than 1 MHz, we

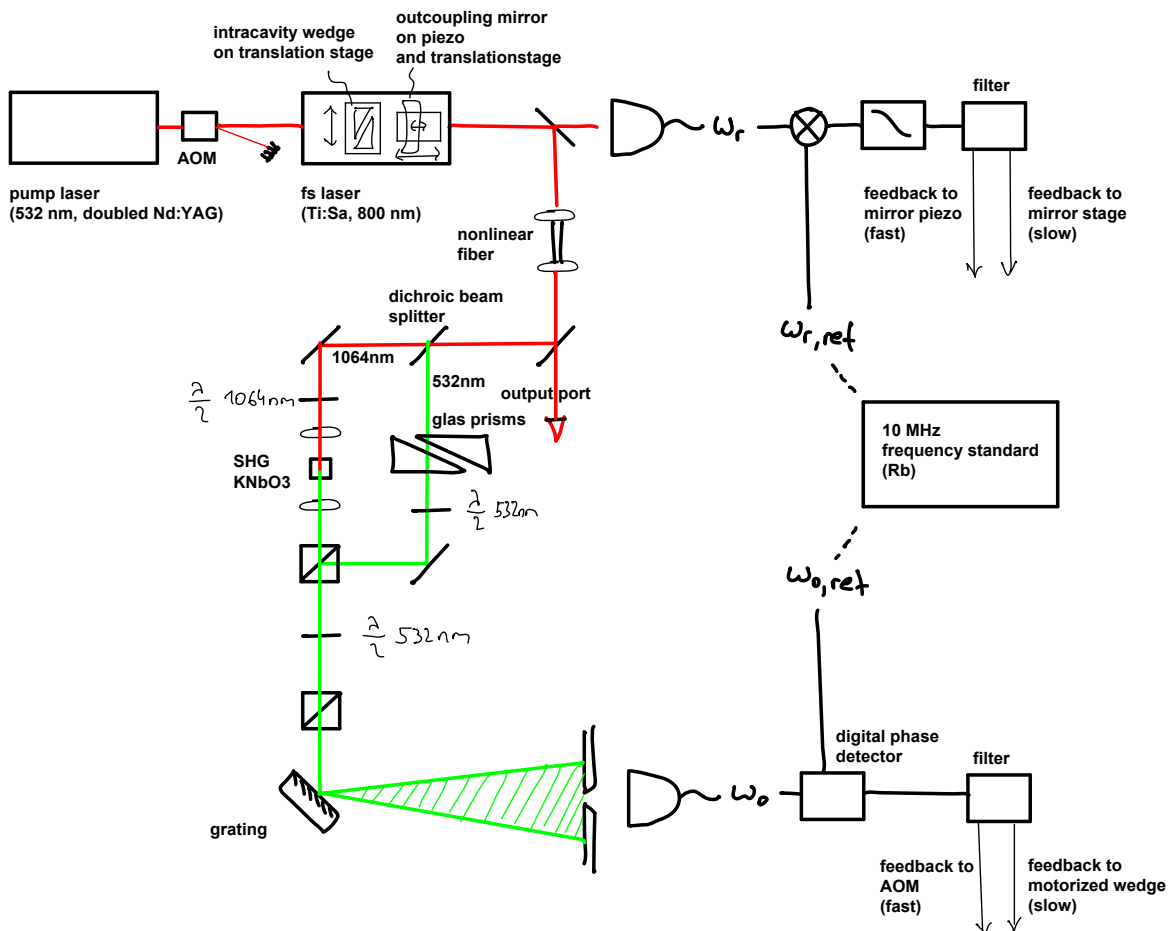


Figure 2.8 Schematic of the f2f interferometer including the feedback loops. Spectral parts around 532 nm and 1064 nm are split at the first dichroic mirror of the interferometer. The infrared part is frequency doubled in a 5 mm long KNbO₃ crystal. In order to measure an offset beat signal, the pulses from the two interferometer arms have to overlap in time, which is achieved by two BK 7 prisms serving as a variable delay line. After being superimposed in the first polarizing beam splitter cube (PBS), the second harmonic and the fundamental beam have orthogonal polarization axis (s and p) so that they can not interfere. For this reason, the following half wave plate is positioned to rotate both polarization axes by 45 degrees, so that they both have a common component projected onto the p-axis after passing the second PBS. The grating before the photodiode is only needed to avoid saturation of the detector by parts of the spectrum that don't contribute to the beat signal. The only interfaces to the electronics on the “output side” of the optical setup are the two photodiodes.

developed an automated system to use the frequency comb as a real time high-precision “wavemeter”.

For this application, it was not simply possible to perform a series of absolute frequency measurements according to Chap. 2.1.3. Since the probe laser was swept, it was by definition insufficiently stable over the time period (of several seconds) needed to complete a single measurement. (Even without a deliberate frequency sweep, its intrinsic frequency drift of at least 0.1 MHz per second was prohibitive.)

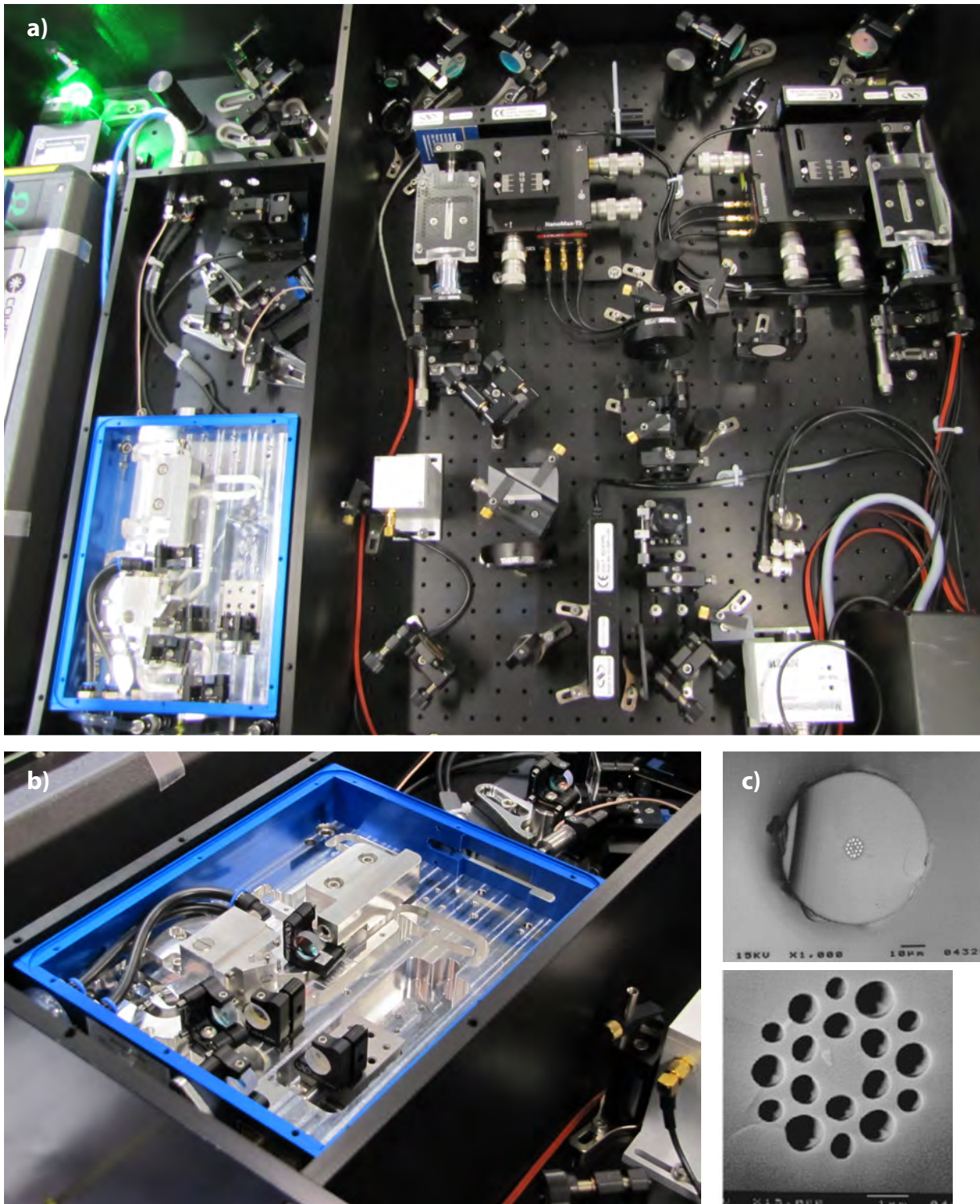


Figure 2.9 (a) Optical setup, consisting of pump (green laser left), femtosecond oscillator (blue box and surrounding black enclosure), and f2f interferometer (right half). Thin-film pellicle beam splitters are used throughout the assembly due to their insignificant GDD contribution. (b) View into the opened femtosecond oscillator. Flexure bearings are machined into the monolithic aluminum base plate for fine-adjustment of several elements. The mount for the tiny Ti:Sa crystal (left aluminum block) is water cooled. (c) Scanning electron microscope (SEM) images of a typical PCF.

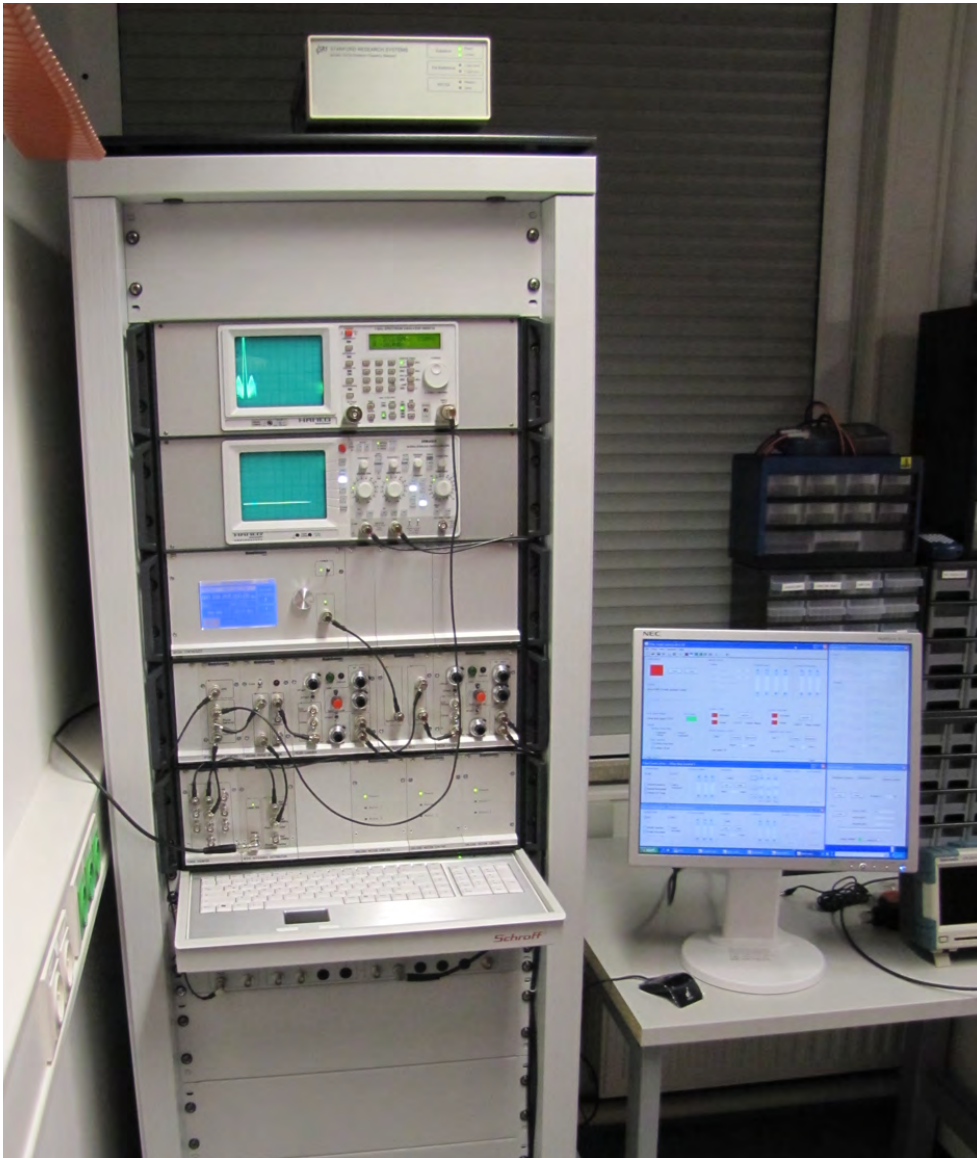


Figure 2.10 Electronics rack for comb stabilization with the following components (top to bottom): rubidium frequency reference (standalone box), spectrum analyzer displaying the offset beat note, oscilloscope displaying error signals for both feedback loops, digital frequency generator, phasedetectors and PID feedback electronics, reference frequency outputs and counter inputs, PC-based control software (to the right).

However, at least the relative frequency changes could be reliably monitored, by recording the beat spectrum between the probe laser and the frequency comb with a sensitive spectrum analyzer (Anritsu MS 2718B) every few seconds (Fig. 2.12). These spectra were automatically analyzed to reconstruct the time-dependent probe laser frequency. As the probe laser frequency moves relative to the comb spectrum, ambiguity in the interpretation of the spectrum arises in increments of half the repetition frequency, whenever the probe laser “crosses” a comb line or midpoint between two comb lines. If small regions around these points are excluded, and a certain continuity in the frequency evolution of

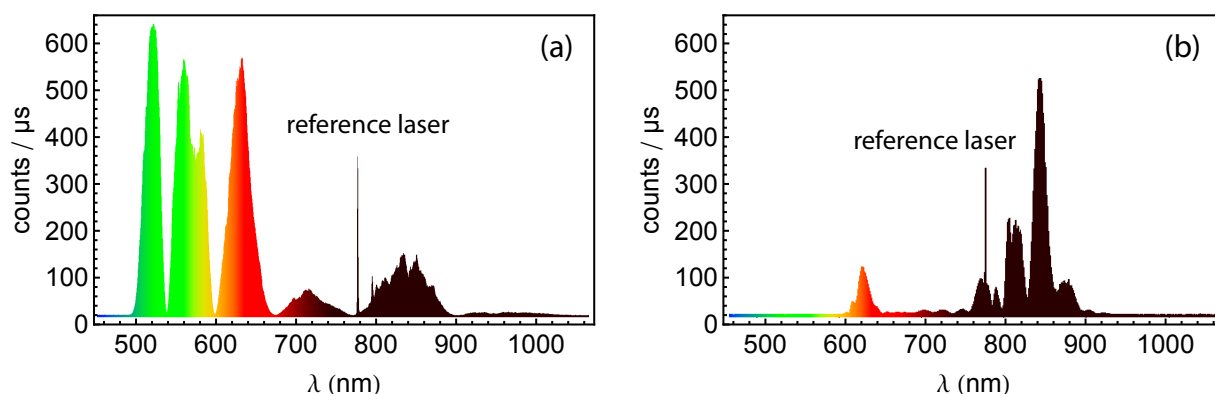


Figure 2.11 Broad comb spectra, measured with a grating spectrometer after passing through the PCF. Very different spectral distributions can be achieved by changing the polarization of the input and tuning of the fiber coupling. The shown reference laser line is a diode laser locked to the $5D_{5/2} \rightarrow 5S_{1/2}$ two-photon transition of rubidium at 778.1 nm, which was used to check the integrity of the comb measurement procedure. (a) Strong spectral components between 500 and 700 nm, and an unfavorable dip around 778 nm for beat-note detection of the reference laser. (b) Optimized spectrum.

the probe laser is assumed, its reconstruction is still possible (Fig. 2.13), providing a very precise frequency reference for spectroscopic measurements.

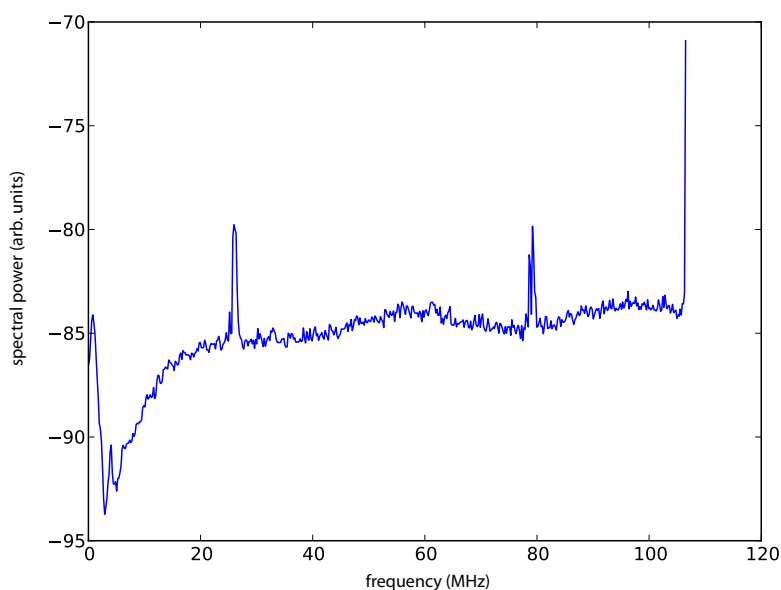


Figure 2.12 Beat spectrum recorded by a spectrum analyzer. Here, the repetition rate of the comb was 108 MHz, as indicated by the strong (clipped) peak on the right (which corresponds to interference of all comb lines with their respective neighbours). The two small symmetric peaks correspond to the difference frequency signal between the probe laser and the closest comb lines. Whenever they come close to crossing each other, or the the limits of the 0-108 MHz range, it is not a-priori clear if the crossing “has already happened” or “is about to happen” (for given assumptions about the sweep rate of the probe laser, and the time delay between individual measurements).

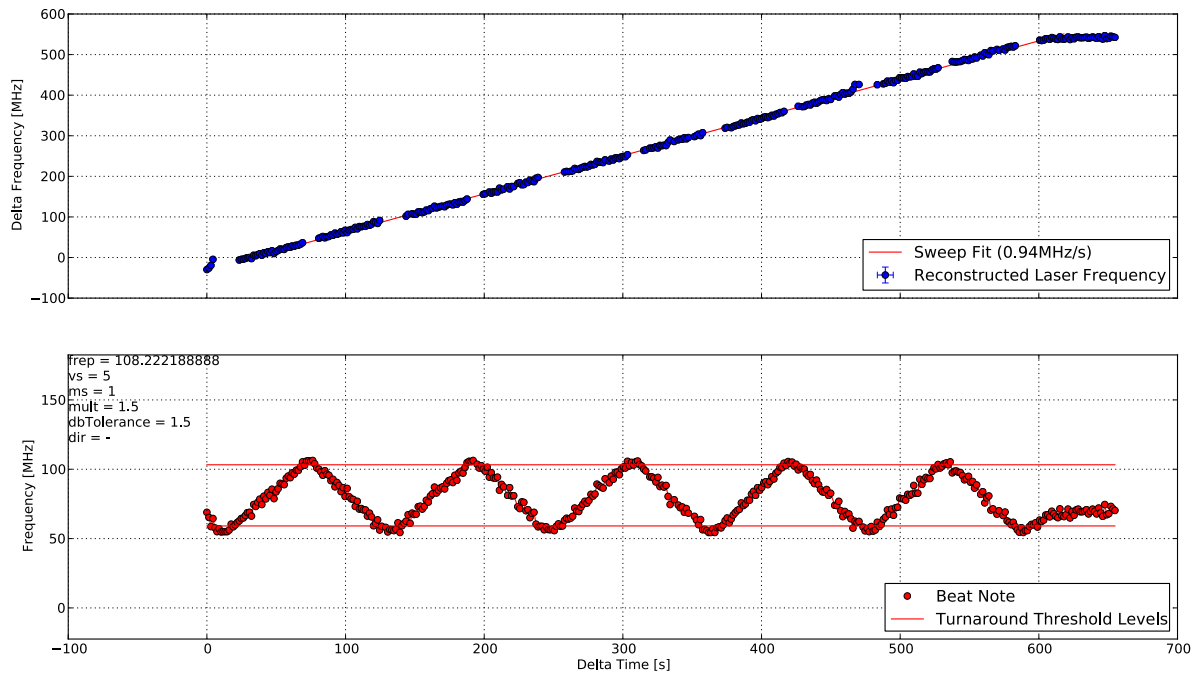


Figure 2.13 Top: Reconstruction of the frequency sweep. Bottom: Result of fits to the higher-frequency beat note (right peak in Fig. 2.12) as a function of time. Data points in the vicinity of 108 MHz (comb repetition rate) and 54 MHz (half the repetition rate) are rejected. The threshold values are marked by red lines.

3 A novel non-planar passive femtosecond enhancement cavity design

3.1 Pulse amplification for nonlinear conversion applications

Currently, femtosecond laser sources which are the basic building block of optical frequency combs, are only available directly in visible to near-infrared spectral regions owing to the limited choice of suitable gain media. However, it is possible to extend the accessible wavelength range via non-linear conversion processes. The method of choice to attain wavelengths in the VUV/XUV range is high-harmonic-generation (HHG) in gaseous media which requires an especially high peak power density of the fundamental radiation well above 10^{13} W/cm² [28–29]. However, in this regime usual amplification techniques like chirped pulse amplifiers (CPA) or regenerative amplifiers typically imply a significant reduction of the pulse repetition rate (originally in the range of 100 MHz). This renders the comb spectrum unusable for the intended frequency measurements as it reduces the spectral separation of the individual comb lines. Another possibility is to recycle the unconverted pulse fraction in an external femtosecond enhancement cavity (fsEC).

3.2 Enhancement cavity basics

The following treatment is focused on ring cavities due to their favorable features in the context of HHG, as outlined in Chap. 3.3. However, all derivations equally apply to linear cavities with minor modifications.

3.2.1 Resonance, power enhancement and impedance matching

The power buildup in multi-mirror ring cavities can be modeled by generalizing the theory of two-mirror Fabry Perot cavities [30]. Let's consider a simple three-mirror ring cavity as in Fig. 3.1. The treatment can be easily extended to more mirrors.

For simplicity we ignore details of cavity stability and transversal mode shapes for now and only consider beam propagation of plane waves and plane mirrors. The electric field incident on the resonator input mirror $M1$ with specific frequency ν is described by the complex amplitude E_0 . After passing through the input mirror, experiencing an attenuation given by the input coupling mirror power transmission T_1 and a phase shift ϕ' , the amplitude is changed to E_1 . The effect of each further (n-1)th roundtrip inside the cavity can be summed up by multiplication with the round-trip attenuation factor ρ and through a phase change ϕ , which yields amplitudes $E_{2..∞}$. Contributing to ρ are the reflectances $R_{1..3}$ of all mirrors and the absorption loss factor L_A accounting for absorption or scattering losses (in air, samples or coatings) and diffraction losses at mirror boundaries²⁸. All

²⁸ L_A essentially accounts for all energy removed from the defined intra- or extra-cavity spatial mode of the light field.

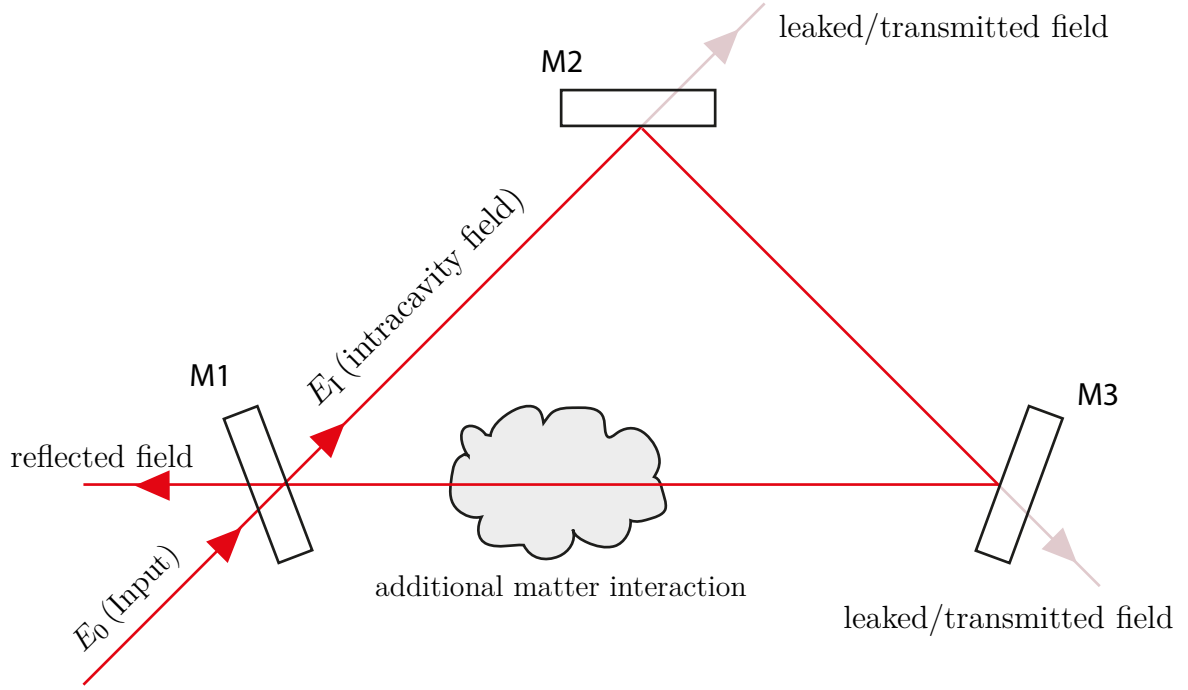


Figure 3.1 Schematic of a ring cavity. All mirrors M are characterized by a transmittance T , reflectance R and possibly some additional loss factor L which satisfy $T + R + L = 1$. Additional loss is introduced through interaction with matter (sample, atmosphere, additional optical elements) inside the cavity. The intracavity field is not exactly the same everywhere inside the cavity due to several loss mechanisms being distributed along the optical path. Strictly speaking, E_1 is defined as the intracavity field directly behind the incoupling mirror.

quantities which represent a reflectance, transmittance or loss appear under a square root, because they are defined with respect to the field intensity, not amplitude. The effective field E_1 inside the resonator can be determined by summing up the infinite geometric series formed by all E_n leading to the result given by Eq. 3.1b

$$\begin{aligned}
 E_1 &= E_0 \sqrt{T_1} e^{i\phi'} \\
 E_2 &= E_1 \underbrace{\sqrt{R_1 R_2 R_3 (1 - L_A)}}_{\sqrt{\rho}} e^{i\phi} \\
 &\vdots \\
 E_n &= E_0 \sqrt{T_1} e^{i\phi'} (\sqrt{\rho} e^{i\phi})^{n-1} \\
 E_1 &= \sum_{n=1}^{\infty} E_n = E_0 \sqrt{T_1} e^{i\phi'} \sum_{m=0}^{\infty} (\sqrt{\rho} e^{i\phi})^m \tag{3.1a}
 \end{aligned}$$

$$= E_0 \sqrt{T_1} e^{i\phi'} \frac{1}{1 - \sqrt{\rho} e^{i\phi}}. \quad \text{using: } \sum_{n=0}^{\infty} q^n = \frac{1}{1 - q} \quad (3.1b)$$

From this, one can derive the power enhancement factor \mathcal{P} defined as the ratio of intracavity power to incident power:

$$\begin{aligned} \mathcal{P} &= \frac{|E_1|^2}{|E_0|^2} = \frac{T_1}{1 - 2\sqrt{\rho} \cos(\phi) + \rho} \\ &= \frac{T_1}{(1 - \sqrt{\rho})^2 + 4\sqrt{\rho} \sin^2(\frac{\phi}{2})}. \quad \text{using: } \cos(2\alpha) = 1 - 2\sin^2(\alpha) \end{aligned} \quad (3.2a)$$

As follows from the sine term, \mathcal{P} is periodically modulated as a function of the round trip phase shift ϕ with constructive interference leading to distinctive maxima (resonances) at integer multiples of 2π (Fig. 3.2).

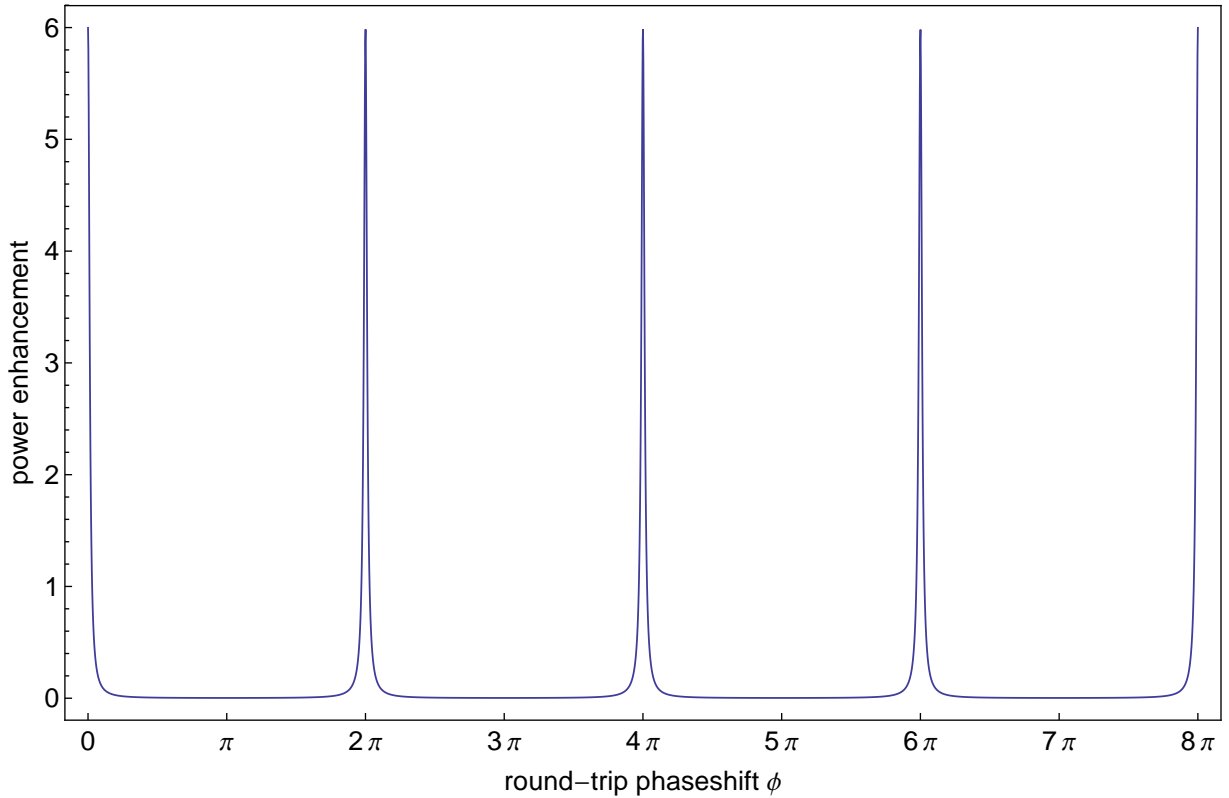


Figure 3.2 Dependence of the power enhancement \mathcal{P} on the round-trip phaseshift ϕ according to Eq. 3.2a. Intracavity power and cavity transmission are directly proportional. Resonances occur at 2π -intervals of the round-trip phaseshift, when the complex phase vectors corresponding to individual round-trips line up for maximum constructive interference.

By setting $\phi = 0$ we get the amount of the maximum resonant enhancement:

$$\mathcal{P}_{\text{onres}} = \mathcal{P}(\phi = 0) = \frac{T_1}{(1 - \sqrt{\rho})^2} = \frac{T_1}{\left(1 - \sqrt{\underbrace{R_1}_{1-T_1} \underbrace{R_2 R_3 (1 - L_A)}_{1-L'}}\right)^2} \quad (3.3a)$$

$$= \frac{T_1}{(1 - \sqrt{(1 - T_1)(1 - L')})^2}. \quad (3.3b)$$

Here we repartitioned the round trip attenuation factor ρ into the input mirror reflectance R_1 and the residual cavity loss (factor) L' which combines all remaining contributions to round trip loss. By setting $R_1 = 1 - T_1$ we further make the implicit assumption that the input mirror itself is free of absorption losses (in order not to unnecessarily complicate the mathematical treatment)²⁹. We can now analyze how the magnitude of the resonant enhancement depends on the balance of the two parameters T_1 and L' . A graphical representation of the interrelation is given in Fig. 3.3.

For a given residual loss L' the enhancement is maximized by choosing an equal value for T_1 which is called the mode-matched condition:

$$\mathcal{P}_{\text{onres, modematched}} = \mathcal{P}(T_1 = L') = \frac{1}{T_1} = \frac{1}{L'}. \quad (3.4)$$

This means that, theoretically, even the full available optical power (incident on the cavity) can be converted by a conversion process driven inside the cavity, independent of its intrinsic efficiency η , if the process itself is the only source of residual "loss" ($L' = \eta$), because a factor $1/\eta$ higher power is then sustained inside the cavity. To put it in other words, the effective efficiency of the process (yield measured relative to the full available power incident on the cavity) could be enhanced to up to 100 percent. This is the basic motivation to use a resonator as an "enhancement cavity", be it for increased efficiency of nonlinear conversion processes or increased sensitivity to sample absorption (as in cavity-enhanced absorption spectroscopy). Of course the requirement $L' = \eta$ is hard to be entirely fulfilled in practice, because it implies that all mirrors except the input mirror are ideal mirrors, and that there are no additional absorptive losses except the process under consideration.

For a given input mirror transmittance T_1 however, less residual loss always yields higher enhancement, with the maximum enhancement reached for zero residual loss:

$$\mathcal{P}_{\text{onres, lossless}} = \mathcal{P}(L' = 0) = \frac{T_1}{(1 - \sqrt{(1 - T_1)})^2}.$$

This last value, however, does not hold practical relevance, since the presence of some "lossy" process is the reason to use an enhancement cavity in the first place. The strategy is rather to suppress "unnecessary losses" (such as scattering from dirty mirrors) and only then match the input coupling mirror to L' .

²⁹ The assumption is reasonable, as the incoupling mirror is typically only one out of many mirrors and a large fraction of the overall loss budget is attributed to propagation through material in the cavity anyways.

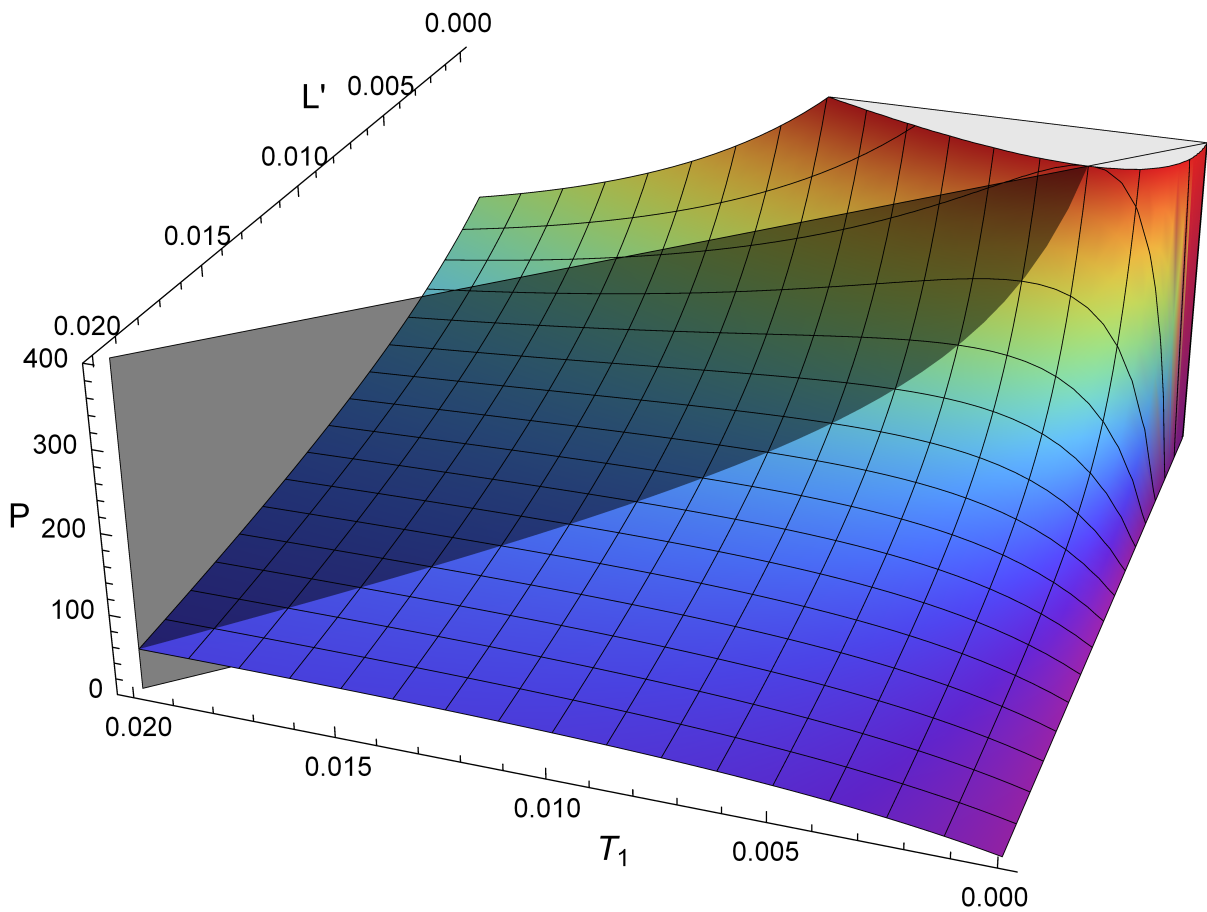


Figure 3.3 Dependence of the power enhancement \mathcal{P} on the distribution of loss contributions between the input mirror transmittance T_1 and all other loss sources L' . For a given value of T_1 , smaller residual losses L' always yield higher enhancement. For a given value of L' however, maximum enhancement is reached in the impedance-matched case of $T_1 = L'$ (marked by the grey diagonal). It can be seen that deviating from this condition with a slightly too small value of T_1 can be more critical than a slightly too large value.

For practical reasons it can still be beneficial to deviate from the ideal mode-matched condition and sacrifice some enhancement. Since losses typically vary during operation, the deliberate choice of an overcoupled regime ($T_1 > L'$) can prevent the risk of entering the undercoupled regime ($T_1 < L'$) with much stronger associated penalty on intracavity power, as is obvious from Fig. 3.3.

The amount of light leaking outside the cavity through individual mirrors is directly proportional to the intracavity power (with the respective mirror transmittance as the proportionality factor), which makes \mathcal{P} easy to measure indirectly once the mirror transmittance is known. Only the input mirror takes a special role - the power measured in its "exit path" is determined by interference of two field contributions - leakage from the cavity and the reflected part of the incident light. Under steady state conditions energy conservation must hold, which means that the total power exiting the cavity minus absorptive losses defined by L_A must equal the incident power.

To make a stronger statement about how this power is distributed, let's define the transmission \mathcal{T} of the cavity as the sum of the power leaking through all mirrors except the input mirror, normalized by the incident power. If we consider the case where leakage through the mirrors is the only source of loss ($L_A = 0$) we can state $\mathcal{T} = \mathcal{P} \cdot L'$. If we further assume the input mirror to be modematched it follows from Eq. 3.4 that $\mathcal{T} = \frac{1}{L'} L' = 1$ on resonance, signifying that the full incident power is transmitted through the cavity and accordingly zero power is reflected at the cavity input. According to Fig. 3.2 the power enhancement approaches zero for the off-resonant cavity, essentially causing the ratio of transmitted to reflected power to reverse. Such operating conditions are therefore particularly suitable when using the cavity as a sensitive frequency filter, analyzer or reference³⁰. The behaviour is typically exploited in the form of a simple Fabry Perot cavity with two parallel mirrors of equal reflectance ($T_1 = T_2 = L'$), as single input (reflection) and output (transmission) ports³¹.

3.2.2 Finesse, dispersion effects and spectral mode matching

The previous chapter was mainly concerned with the maximum value of the on-resonance power enhancement. Now we will take a more detailed look at its frequency dependency and related cavity parameters. The round-trip phase shift ϕ in Eq. 3.2a can be expanded like

$$\phi(\omega) = \frac{L\omega}{c} + \delta\phi(\omega) \quad (3.5)$$

with the first trivial term due to free space propagation (in vacuum) over the cavity (round trip³²) length L and the second, generally non-linear, term $\delta\phi(\omega)$ contributed by interaction with mirror coatings or material inside the cavity. Let's assume first that $\delta\phi(\omega)$ is negligible. Then, ϕ is proportional to ω , and the resonance peaks (also called spectral modes) of Fig. 3.2 remain equidistant when transitioning to frequency space (Fig. 3.4). The corresponding distance is called the free spectral range $\Delta\omega_{\text{FSR}}$:

$$\Delta\omega_{\text{FSR}} = \frac{2\pi c}{L}.$$

We also note how the resonance peaks get "sharper" for decreasing round trip loss (larger ρ). This property is quantified by the cavity finesse \mathcal{F} , defined as the ratio of the free spectral range to the FWHM³³ of the spectral modes:

³⁰ The phase shift ϕ and therefore the resonance condition is dependent on the frequency ω of the incident field. (See Chap. 3.2.2 for details).

³¹ Non-negligible intracavity loss L_A or imperfect mode-matching reduces the "contrast" of this filtering effect.

³² In the discussion of ring cavities L denotes the full round trip length, even when considering the special case of only two mirrors, whereas it denotes only half that length (the two-mirror separation distance) in the typical treatment of Fabry-Perot cavities, which easily leads to confusion.

³³ The FWHM in phase space is obtained by solving $\mathcal{P}(\phi = \frac{\phi_{\text{FWHM}}}{2}) = \frac{\mathcal{P}(\phi=0)}{2}$.

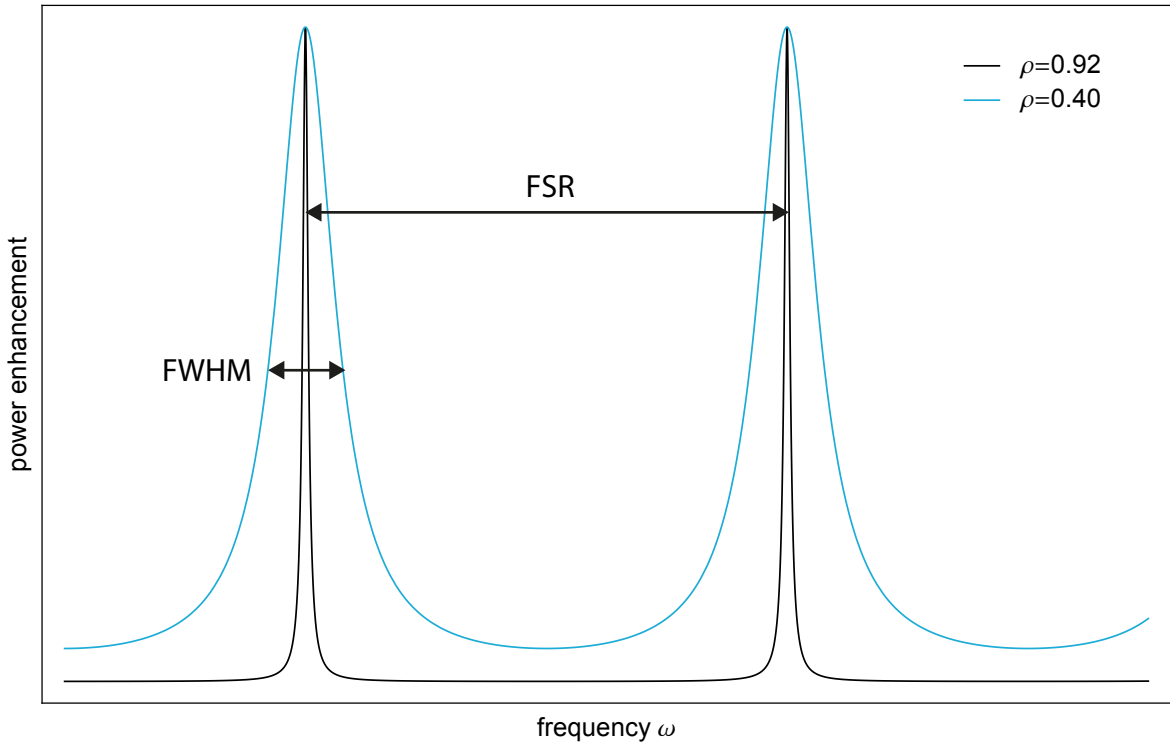


Figure 3.4 The spectral cavity response according to Eq. 3.2a, with the power enhancement \mathcal{P} now plotted as a function of circular frequency ω . The width of the spectral modes increases with growing round trip attenuation factor ρ .

$$\begin{aligned}\mathcal{F} &:= \frac{\Delta\omega_{\text{FSR}}}{\Delta\omega_{\text{FWHM}}} = \frac{2\pi}{\Delta\phi_{\text{FWHM}}} \\ &= \frac{\pi}{2 \arcsin\left(\frac{1-\sqrt{\rho}}{2\sqrt{\rho}}\right)} \approx \frac{\pi}{1-\sqrt{\rho}} \approx \frac{2\pi}{1-\rho}\end{aligned}$$

where the last approximations hold for low round-trip losses (e.g., 10%), i.e., only for high finesse values. Increasing the finesse is a typical goal when using a resonator for optical spectrum analysis (e.g. with a Fabry Perot interferometer) and is achieved by increasing the reflectivity of all mirrors³⁴. For the sake of highest possible intracavity enhancement however, the impedance-matching criterium of the previous chapter applies. In addition, one has to consider that for efficient coupling of a continuous wave (single frequency) source to the cavity, the source linewidth should be smaller or at least comparable to the width of the cavity modes - otherwise a significant part of the input spectrum won't be fully resonant/enhanced inside the cavity.

³⁴ The finesse is only given by resonator losses, and independent of resonator length. Therefore the absolute linewidth can be made smaller simply by increasing the cavity length, which is typically done for stable external laser reference cavities.

When taking into account a significant term $\rho(\phi)$ in Eq. 3.5 the nonlinear dependence of the cavity round trip phase on frequency (intracavity dispersion) distorts the regular mode structure (Fig. 3.5) and leads to a frequency-dependent FSR. To a first approximation, this distortion is described by the second derivative of $\phi(\omega)$ - the group delay dispersion (GDD).

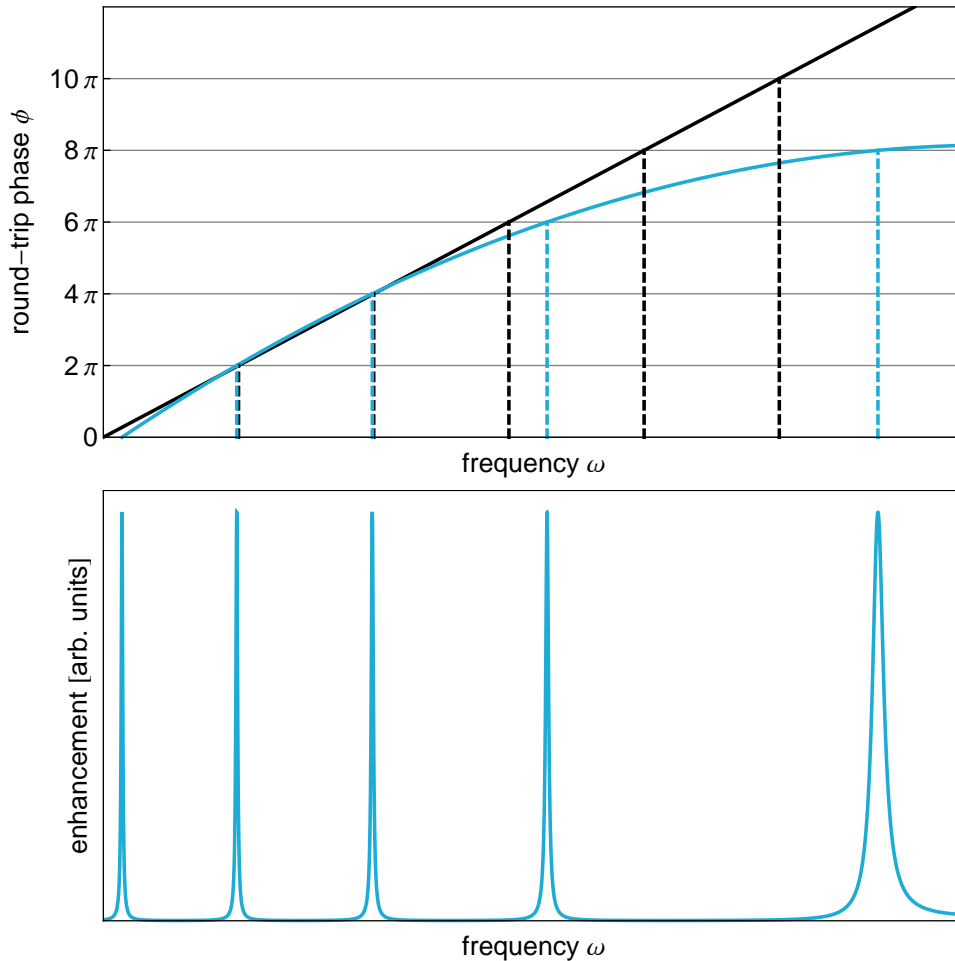


Figure 3.5 Cavity dispersion. The mode-spacing or FSR changes with frequency as a result of the nonlinear dependence of the cavity round trip phase on frequency. The amount of asymmetry visible in the rightmost broadened mode can be used as a direct indicator to quantify GDD inside the cavity.

To guarantee resonant enhancement of the output of a mode-locked laser, the regular comb spectrum of the source must overlap with the cavity eigenmodes. It is therefore critically important to assure zero intracavity dispersion at least over the relevant bandwidth. One of the most critical (and typically bandwidth-limiting) aspects is to design the dielectric stacks of the resonator mirror coatings accordingly. This requirement is a key difference between a passive external enhancement cavity and a mode-locked laser resonator. In the latter case the active medium intrinsically guarantees perfectly equidistant spacing of the resonant frequencies (making it the precision measurement tool that it is). The general

procedure for proper adjustment of all free parameters in cavity-comb coupling is outlined in Fig. 3.6.

3.2.3 Transversal modes, stability and spatial mode matching

In the two previous chapters the electric fields propagating inside the resonator have been approximated as plane waves to derive the main results related to multi-beam interference inside the cavity. Of course, a real-world resonator with finite-size mirrors calls for propagation of slightly more complex solutions of the free-space wave equation that have confined (typically Gaussian) transverse intensity profiles. (In other words: A solution that represents an actual beam of light is required.) In order for such a beam to stay confined to the cavity, its electric field distribution has to be self-consistent upon propagation - it has to be the same after one complete round trip in the cavity. Here, by field distribution we don't mean the absolute values of phase and amplitude³⁵, but the relative phase and amplitude in a plane perpendicular to the propagation axis, which defines how the intensity profile evolves upon further propagation (the "geometry" of the beam). This requirement can only be satisfied by certain restricted mirror configurations, which are then called a *stable cavity*. The corresponding self-consistent field distribution inside the cavity is called a *spatial mode* of the cavity.

The following reasoning will be based on Gaussian beams as the most fundamental and commonly encountered beam type. The propagation of Gaussian beams through an optical system³⁶ can be treated in paraxial approximation using a very convenient matrix formalism [31] very similar to ray transfer analysis known from geometrical optics. At any specific position z along the propagation axis, the beam is represented by its complex beam parameter $q(z)$ which can be related to its beam radius w and wavefront radius of curvature R (both at position z) or to the waist radius w_0 and waist position z_0 :

$$\frac{1}{q(z)} = \frac{1}{R(z)} - i \frac{\lambda}{\pi w(z)^2} \quad (3.7)$$

$$q(z) = (z - z_0) + i \frac{\pi w_0^2}{\lambda}. \quad (3.8)$$

For each optical element there exists a transfer matrix M which relates the beam parameter at the output (q_2) to the one at the input (q_1) like

$$\begin{pmatrix} q_2 \\ 1 \end{pmatrix} = k \underbrace{\begin{pmatrix} A & B \\ C & D \end{pmatrix}}_M \begin{pmatrix} q_1 \\ 1 \end{pmatrix} \quad (3.9)$$

where k is a normalisation constant chosen to keep the second component of the ray vector equal to 1. A sequence of interactions with different elements in an optical system can

³⁵ The absolute values of phase and amplitude is exactly what has been abstracted away (from beam geometry issues) in the treatment within the two preceding chapters.

³⁶ A Gaussian beam still stays a Gaussian beam after interacting with standard optical elements.

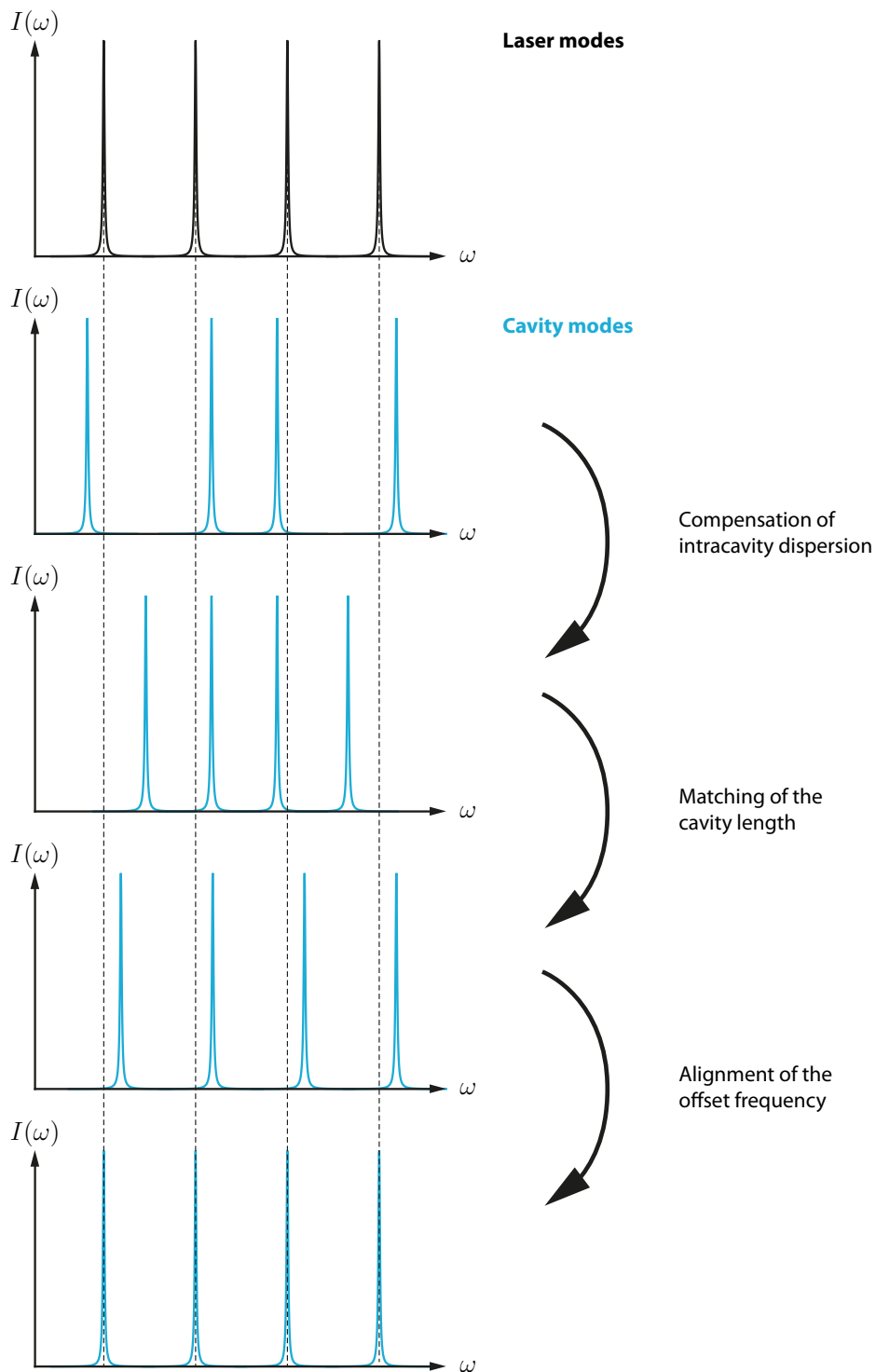


Figure 3.6 Cavity-comb coupling. Several parameters have to be controlled (and feedbacked) to assure a perfect alignment of comb and cavity modes over a broad spectral range.

always be condensed to a single *system matrix* according to the laws of matrix multi-

plication. Expanding the above matrix equation and eliminating k leads to the *ABDC law*

$$q_2 = \frac{Aq_1 + B}{Cq_2 + D}. \quad (3.10)$$

To express the requirement of self-consistency in this formalism, one builds the system matrix M corresponding to one cavity roundtrip (starting at an arbitrary point inside the cavity) and demands $q_1 = q_2 = q$ for Eq. 3.10. Solving the resulting quadratic equation for $\frac{1}{q}$ yields:

$$\begin{aligned} \left(\frac{1}{q}\right)_{1,2} &= \frac{D - A}{2B} \pm i \frac{\sqrt{-4BC - (A - D)^2}}{2B} \\ &= \frac{D - A}{2B} \pm i \frac{\sqrt{4 - (A + D)^2}}{2B}. \quad \text{using: } \det(M) = AD - BC = 1 \end{aligned}$$

In the last line the unitary property of transfer matrices was used. By comparison with Eq. 3.8 one can conclude that the square root has to be real, otherwise the imaginary part of $1/q$, and therefore the beam radius w would be zero, which would not be a physically meaningful solution. This stability criterion is usually stated as

$$-1 < \frac{1}{2}(A + D) < 1. \quad (3.12)$$

Not only can we now determine stable cavity configurations³⁷, but also calculate the exact corresponding mode shapes for arbitrarily complex resonators simply based on their system matrix M . After selecting the sign of the second term (again by comparison with Eq. 3.8) the final result for allowed values of q reads:

$$\frac{1}{q} = \frac{D - A}{2B} - i \frac{\sqrt{4 - (A + D)^2}}{2|B|}. \quad (3.13)$$

In order for the calculated stable field distribution to actually build up inside the cavity, the field distribution of the incoming Gaussian beam has to be exactly matched to the field distribution of the stable mode. This requires an equal waist size of the incoming beam and the first "Gaussian beam segment" of the cavity mode after the incoupling mirror (referred to as *modematching*) as well as collinear propagation axes and overlapping position of the beam waists (referred to as *beam alignment*). Under these conditions all results derived in the previous two chapters essentially still hold. However, a Gaussian beam acquires a slightly different phase shift along its propagation direction compared to a plane wave. This difference, called the Gouy phase shift ϕ_G [32], has to be considered as a minor (and often irrelevant) correction:

³⁷ The same criterion for stable resonators alone can also be derived from geometric optics by requiring paraxial beams to be periodically refocused upon multiple cavity roundtrips in order to stay confined to the cavity [31]. (By comparison, beams get more and more dispersed for unstable cavities.)

$$\phi_G = \arctan \frac{z}{z_R} \quad (3.14)$$

where $z = 0$ corresponds to the beam waist position and z_R is the Rayleigh length.

If we want to understand the consequences of imperfect modematching and alignment on the intracavity field, we have to take the concept of cavity modes a bit further. Gaussian modes are not the only solutions for stable cavity modes. Under less restrictive assumptions on the beam shape, an infinite set of Hermite-gaussian modes [33] can be calculated with the lowest order mode being equal to the Gaussian mode already derived. These modes, which are also called the *normal modes* of the resonator are mutually (power-)orthogonal and form a complete set of basis functions for expanding any propagating fields inside the resonator³⁸. Thanks to this property one can expand the incoming field as a linear combination of those normal modes, and describe imperfect modematching/alignment as an excitation of higher-order modes, with the respective coupling coefficients determined by a simple overlap integral (that can be evaluated at any point inside the cavity). Higher order modes typically have a Gouy-phase that is much higher than that of the fundamental (Gaussian) mode, which means that they also have different resonance frequencies. This can be observed as small side-maxima to the main resonance peaks in the frequency scan of a badly modematched/aligned cavity.

3.3 Counteracting astigmatism in fsECs

3.3.1 Conventional cavity design

The typical fsEC for high repetition rate, high-power non-linear conversion applications like HHG is the bow-tie cavity similar to Fig. 3.7 consisting of two identical spherical mirrors of focal length f at a distance d and at least two folding mirrors in a symmetric planar arrangement. The cavity length L is given by the repetition rate of the seeding laser.

As a stable resonator it fulfills the requirement for significant power enhancement. Cavities consisting of only two spherical mirrors are unsuitable for the following reason: The round-trip optical path length of such resonators is on the order of a few meters (to match a typical pulse repetition rate of about hundred MHz). The laser beam waist inside the cavity however, must be of the order of a few tens of micrometers (to drive nonlinear processes with a sufficiently high power density). For a two-mirror cavity these two requirements could only be fulfilled in a concentric configuration (Fig. 3.8), entailing a very high alignment sensitivity [34][35].

³⁸ Strictly speaking, this is only true if we only consider fields that are sufficiently localized around the axis of the optical system, so that losses due to absorption or diffraction at the edges of apertures or optical elements can be neglected [33]. If this is not the case, a more complex formalism using biorthogonality relationships has to be used.

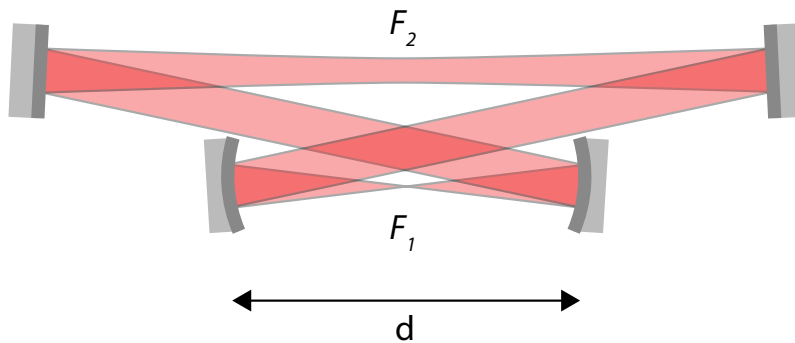


Figure 3.7 Bow-tie resonator in standard planar layout. The primary and secondary foci are labeled F_1 and F_2 .

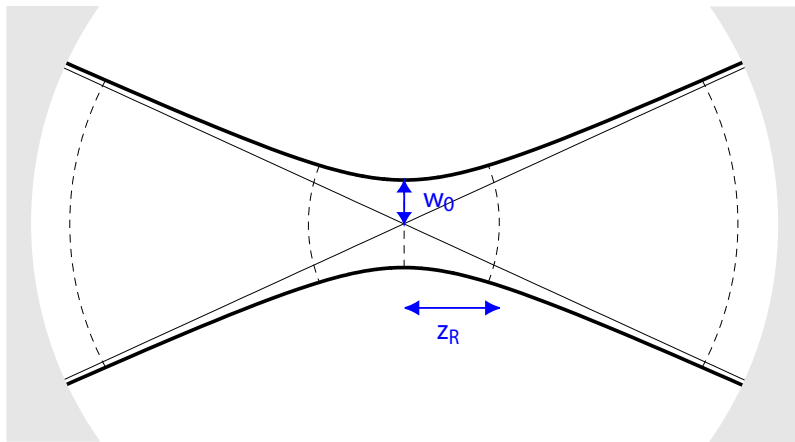


Figure 3.8 Concentric resonator with two spherical mirrors. The Wavefront radius of curvature of the Gaussian beam is infinite at the focus position, reaches a minimum value at a distance of the Rayleigh range and becomes asymptotically proportional to the distance from the focus. A tight focus with a corresponding Rayleigh range significantly shorter than the mirror separation therefore implies a (mechanically sensitive) concentric geometry

Implementation as a ring-resonator avoids a double pass through the non-linear material (which for example would cause emission of high harmonics in opposite directions), eliminates optical feedback into the source and allows straightforward separation of the reflected beam from the seeding beam to derive a locking signal. The bow-tie type folding of the intracavity beam path with at least four mirrors allows small incidence angles on the focusing mirrors which, together with the symmetry of the setup, helps to minimize astigmatic and other optical aberration effects.

Constraints for stable resonator configurations and properties of the associated Gaussian modes can be derived from the round-trip propagation matrix M according to Chap. 3.2.3.

If we first make the idealizing assumption that the concave mirrors are illuminated on-axis (which would technically only be possible if they were lenses with equal focal length instead), we find:

$$M_1 = \begin{pmatrix} 1 & 0 \\ -1/f & 1 \end{pmatrix} \cdot \begin{pmatrix} 1 & d \\ 0 & 1 \end{pmatrix} \cdot \begin{pmatrix} 1 & 0 \\ -1/f & 1 \end{pmatrix} \cdot \begin{pmatrix} 1 & L-d \\ 0 & 1 \end{pmatrix}. \quad (3.15)$$

The index refers to the fact that position P_1 in Fig. 3.7 (just before the second curved mirror in propagatin direction) has been chosen as the arbitrary starting point for a round trip. M is assembled (right to left) from the individual transfer matrices for free-space propagation over a distance d :

$$M_{\text{freespace}} = \begin{pmatrix} 1 & d \\ 0 & 1 \end{pmatrix} \quad (3.16)$$

and for a lens or (orthogonally illuminated) curved mirror of focal length f :

$$M_{\text{lens}} = \begin{pmatrix} 1 & 0 \\ -1/f & 1 \end{pmatrix}. \quad (3.17)$$

It follows for the stability criterion 3.12:

$$-1 < \frac{dL + 2f(f - L) - d^2}{2f^2} < 1$$

This implies a single interval of allowed values for the separation d of the focusing mirrors, defining the stability region, for a given cavity length L and a choice of focal length f for the two identical spherical focusing mirrors. Solving for d at both limits, while taking into account that $L/2$ is the maximum geometrically possible extent of d , yields the exact boundaries

$$2f < d < \frac{L}{2} - \frac{L - \sqrt{L^2 - 8fL}}{2} \quad (3.18)$$

valid for $f < L/8$. For $f > L/8$ there is no real solution for the upper boundary, which means that the cavity is stable up to a maximum separation of $d = L/2$.

Two intracavity focii are necessary in a ring cavity to enable periodic refocusing of the beam. The two intracavity beam waists can be calculated³⁹ from Equations 3.13 and 3.7 - their dependence on d is plotted in Fig. 3.9.

For $f < L/8$ the spot size of the primary focus (F_1 in Fig. 3.7) asymptotically approaches zero at both edges of the stability range, only limited by the finite size of the cavity mirrors. In the secondary cavity arm the beam waist shrinks as well on the outer stability edge (where d is larger), forming a pronounced but weaker secondary focus (F_2), but diverges on the inner edge, leading to a more or less collimated beam.

³⁹ Inserting M_1 into Eq. 3.13 will give a beam parameter q_1 associated with with the Gaussian beam segment in the primary cavity arm (between the two focusing mirrors). To arrive at a beam parameter q_2 for the secondary cavity arm, one could use a slightly rearranged matrix M_2 corresponding to the round-trip starting position P_2 or use Eq. 3.10 to directly relate q_1 and q_2 via the focusing mirror transfer matrix.

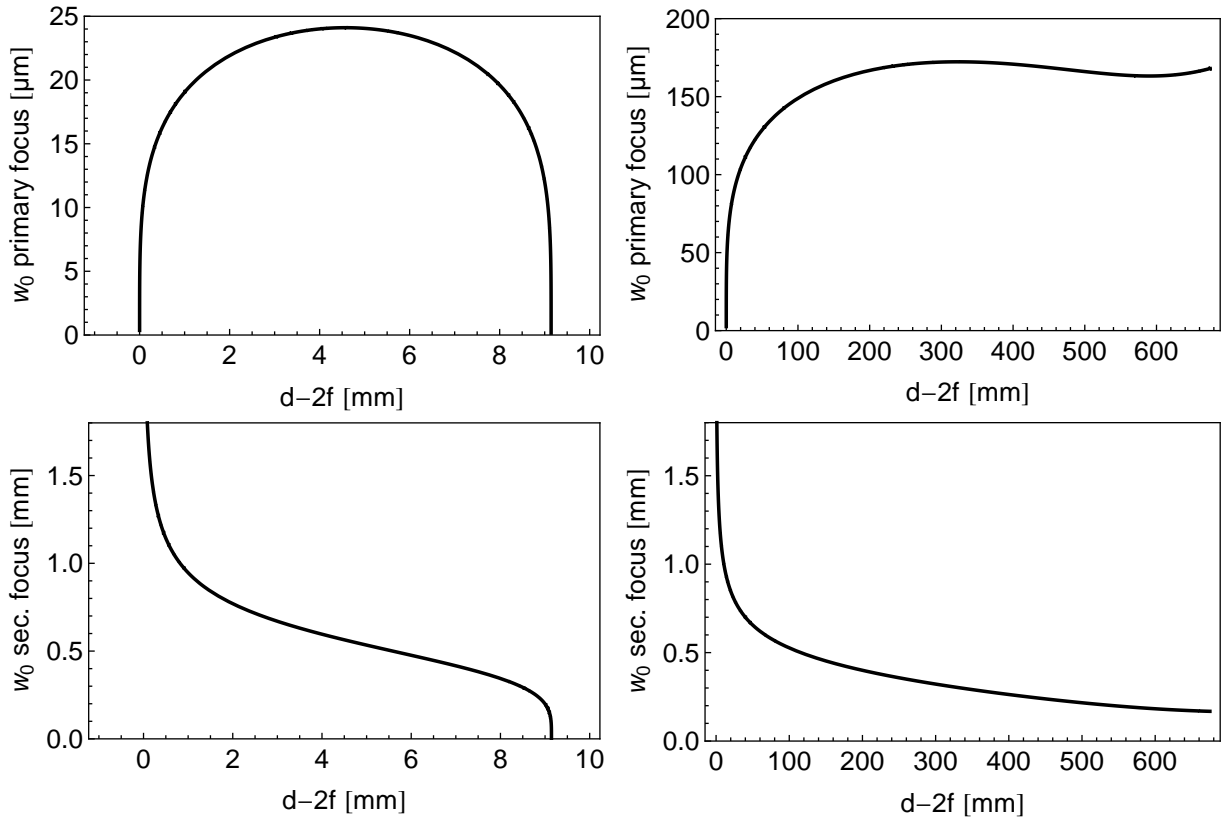


Figure 3.9 Comparison of stability zones for $f < L/8$ and $f > L/8$.

For a real-world fsEC Gaussian beam propagation has to be considered separately for the horizontal and vertical plane. Due to the unavoidable oblique incidence angle on the focusing mirrors, the focal length f in Eq. 3.15 has to be replaced by two effective focal lengths that depend on the orientation relative to the plane of incidence like

$$f_{\parallel} = f \cdot \cos \theta$$

$$f_{\perp} = f / \cos \theta$$

with θ denoting the angle of incidence (AOI). This leads to shifted stability limits for the two planes (blue curves in Fig. 3.11), narrowing the overall accessible stability range and causing increasingly elliptical beam profiles as the stability edges are approached. As can be seen from the plots of the beam profiles in Fig. 3.11, the astigmatic aberration manifests itself as pure ellipticity since the positions of the beam waists in both planes still overlap, which obviously follows from the symmetry of the mirror arrangement.

This effect limits the minimum attainable focus size and thereby the peak power density in the focus. Likewise, it restricts the maximal beam cross-section on the cavity mirrors, which is a major concern for high-power systems, where the damage threshold of the resonator optics becomes the limiting factor [36]. The achievable maximum diameter is reduced in particular by the fact that larger beam diameters necessitate larger incidence angles on the focusing mirrors, increasing the amount of unavoidable astigmatism.

Due to the passive nature of fsECs, the necessity for precise dispersion management of the broadband pulses and high power enhancement (low losses), as little material as possible should be introduced into the cavity. The astigmatic aberrations introduced by oblique incidence on the focusing mirrors, therefore can not be readily compensated by Brewster plates. Several other options have been proposed to address this problem, including additional cylindrical mirrors [36], parabolic focusing mirrors [34], or non-planar cavities [37].

In the following chapter, a straightforward non-planar configuration of the standard bow-tie cavity configuration is introduced, which significantly relaxes the before-mentioned aberration-related limitations, without introducing significant additional complexity or additional elements.

3.3.2 Non-planar cavity design

The basic idea put forward in this work is to counteract these limitations by rotating the plane of incidence for one of the focusing mirrors to the vertical plane by 90 degrees (Fig. 3.10), so that for both horizontal and vertical mode equations there is one mirror with increased and one with reduced effective focal length to consider [38].

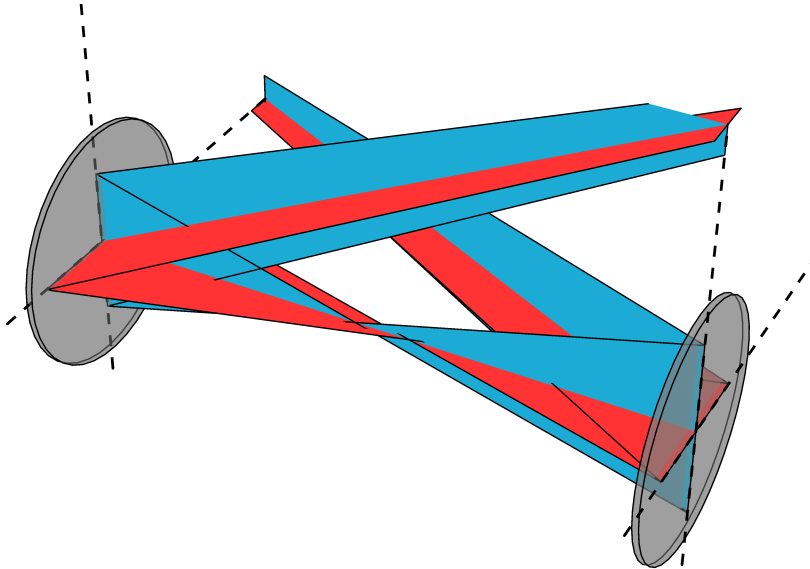


Figure 3.10 Detailed view of the orthogonally folded beams around the two focusing mirrors of the non-planar geometry, with vertical (blue) and horizontal (red) optical planes.

This way the beam waists in both planes are of the same size, however for both planes the symmetry of the setup around the midpoint between the two focusing mirrors is broken, slightly shifting the position of the beam waists along the optical axis - in different directions for different planes, due to switched order of appearance of the effective focal lengths. This again introduces a small astigmatism. The crucial advantage is that now the beam profiles are always circular both at the midpoint where the circle of least confusion

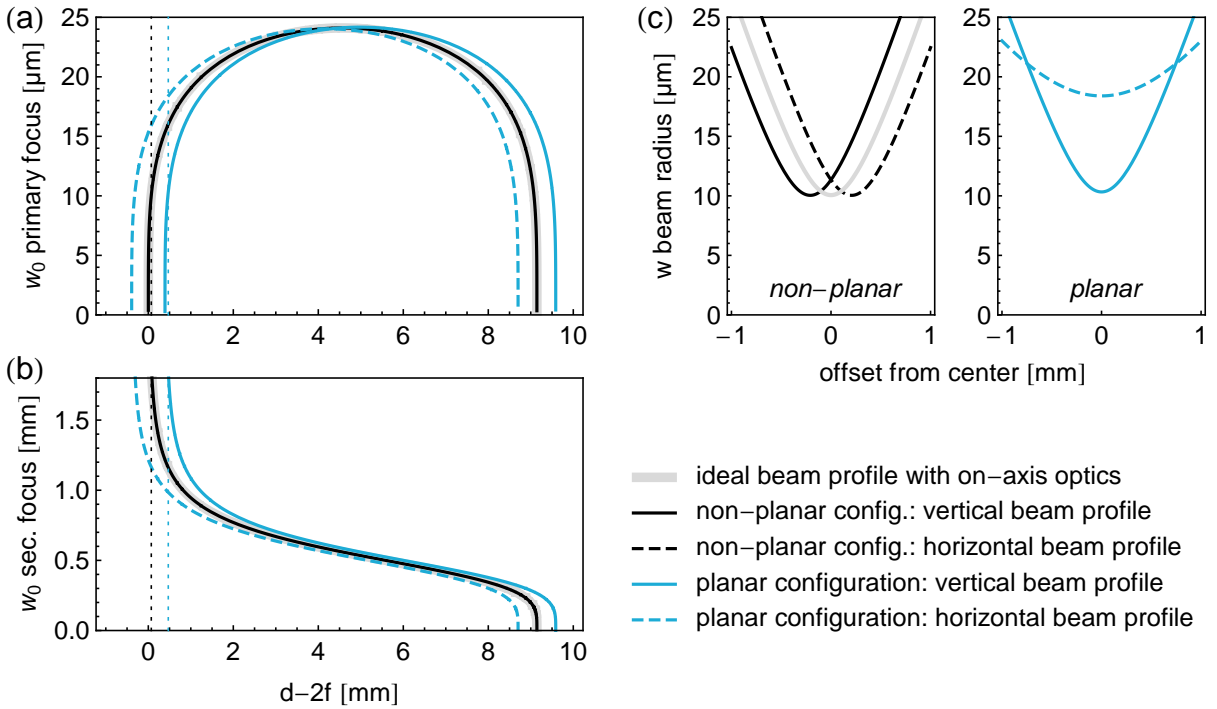


Figure 3.11 Stability diagram and focus profiles. The calculation is based on the experimental parameters given in Chap. 4, that is $f = 75 \text{ mm}$, $\lambda = 800 \text{ nm}$, $L = 2.77 \text{ m}$, $AOI = 4.2^\circ$. (a) The primary and (b) secondary beam waist size is plotted over the entire stability region. The values for the horizontal and vertical plane differ in case of the planar layout (blue), whereas they are the same for the non-planar one (black), coinciding with the value for the ideal case of zero incidence angle (grey). (c) The corresponding Gaussian beam.

occurs, as well as - to very good approximation - further away from the focus. Compared to the elliptical beam profiles of an equivalent planar setup, the power density is decreased on the cavity mirrors and increased in the focus under typical conditions (Fig. 3.11). The ratio of the two cross-sections, signifying the amount of focusing improvement, reaches a maximum at a position very close to the stability edge. Only when moving even closer to the stability edge (in which case the cavity would be hard to stabilize anyway), will the astigmatism become noticeable. Since the separation distance of the beam waists in the different planes remains almost constant over the entire stability range, degradation of the focusing geometry is mainly due to the larger divergence of an even tighter focus (Fig. 3.12). The separation distance shrinks for smaller angles of incidence and shorter focal lengths, so that minimizing those can still be beneficial to attain the smallest possible focal spot. In general this does not mean that the non-planar scheme becomes less effective when moving to longer focal lengths, since also the beam ellipticity exhibited by the equivalent planar setup would increase in this case, at comparable points in the stability diagram.

For the enhancement cavity to be practically useful, the (linear) polarization state of the resonating field has to be conserved, which is not guaranteed for arbitrary non-planar layouts, since the polarization main axes before and after a reflection are defined with respect

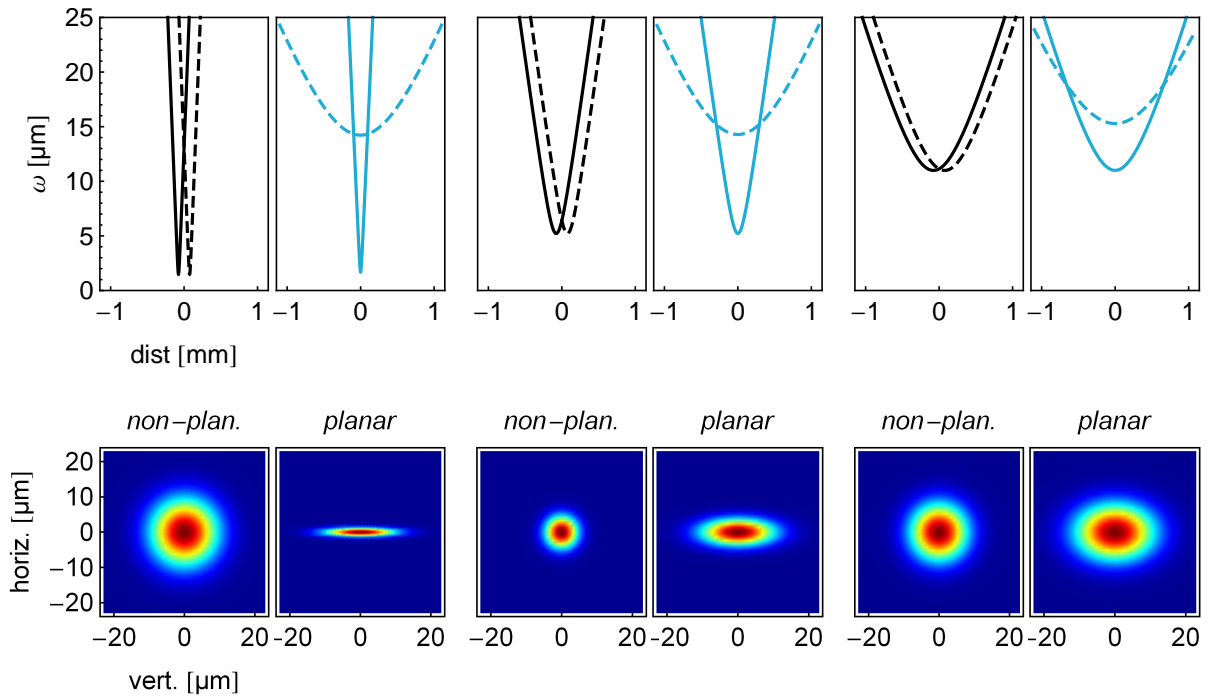


Figure 3.12 Comparison of primary focus geometries for increasing distance ($< 1 \mu\text{m}$, $5 \mu\text{m}$ and 0.1 mm respectively) from the stability edge. The beam profiles are plotted solid for the vertical plane and dashed for the horizontal plane. The bottom cross sections apply to the symmetry point at position zero. All calculations are done based on the same parameters as in Fig. 3.11, except for a more typical AOI of 2.5° . The middle pair represents a configuration where the non-planar setup is performing optimally.

to the plane of incidence, which can easily lead to geometric rotation of the polarization after a single roundtrip. As detailed in the Chap. 4, the resonator presented here has been folded in a way to preserve the polarization similar to a planar one. The scheme requires a minimum of 6 folding mirrors.

4 Experimental realization of the EC

4.1 Overview of the resonator setup

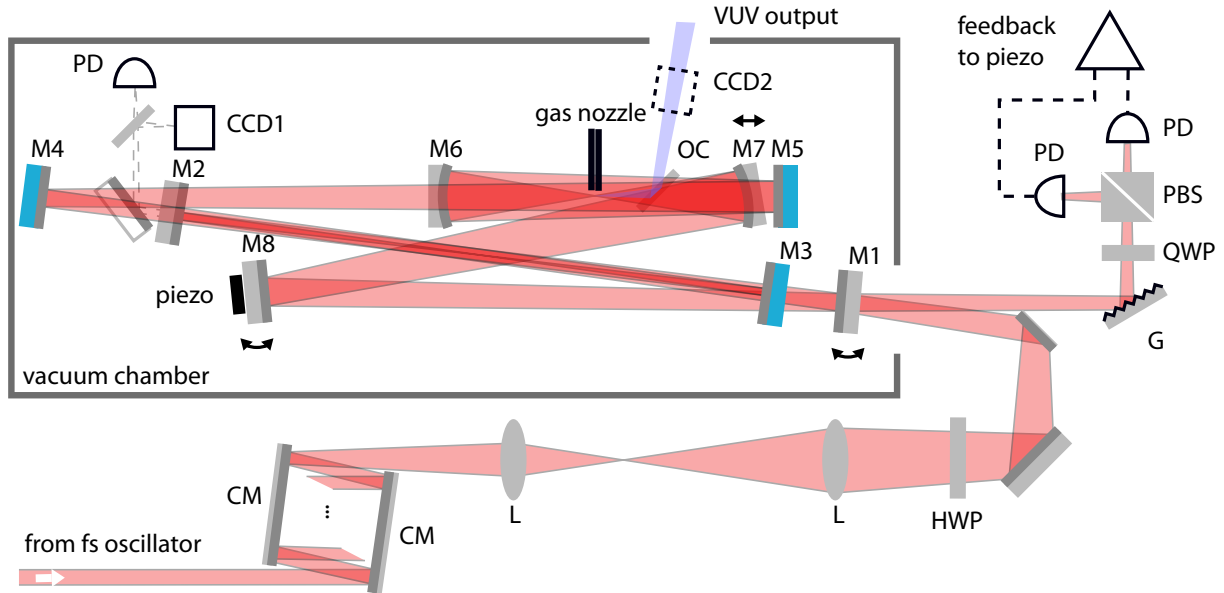


Figure 4.1 Schematic of the fsEC experimental setup. M1-M8: cavity mirrors (those depicted in blue are aligned on a second horizontal level), CM: chirped mirrors, L: lenses for mode-matching, PD: photodiode, OC: output coupler, PBS: polarizing beam splitter, QWP: quarter wave plate, HWP: half wave plate, G: grating.

An overview of the experimental setup is provided in Fig. 4.1. We seed the fsEC with the Ti:Sapphire oscillator-based frequency comb described in Chap. 2, which generates 25 fs-long pulses centered around 800 nm with 900 mW of average power at a repetition rate of 108 MHz (FC8004, Menlo Systems). This system was chosen in order to directly obtain the 160 nm target wavelength as the fifth harmonic of the fundamental wavelength.

A two-lens telescope is used for spatial mode matching to the fsEC (see Chap. 4.3). Multiple reflections on pairs of chirped mirrors pre-compress the seed pulses to compensate for group delay dispersion (GDD) introduced by air propagation, optical elements and windows before the cavity (see Chap. 4.4).

The cavity length of 2.77 m is matched to the seeding laser repetition rate and brought to a manageable footprint using 6 folding mirrors (M1-M5, M8 in Fig. 4.1). The spherical focusing mirrors M6 and M7 have a focal length of 75 mm. All mirrors are broadband high reflectors, except for the input coupling mirror M1 with a transmission of one percent. The total amount of 8 mirrors further allows to realize the non-planar bowtie layout discussed in Chap. 3.3.2 by folding the beam path in a way that does not introduce a geometric rotation of the polarization axis upon one cavity roundtrip (see Chap. 4.2).

To be able to experiment with other more bulky outcoupling elements, a rather large angle of incidence of 4.2° on the focusing mirrors is chosen.

The cavity itself is built inside a vacuum chamber (see Chap. 4.6) to avoid reabsorption of the generated VUV signal by oxygen in air. All mechanical mounts requiring adjustment during operation therefore need to be remote-controlled. Direct drive piezoelectric steppers (Newport Agilis series) were chosen which provide several millimeter travel range at 50 nm resolution. The driver electronics were custom-built to minimize single-step overshoot for most precise alignment (detailed wiring diagram and PCB layout in appendix A).

4.2 3D beam folding

Efficient HHG strictly requires a linearly polarized driving laser field. Since transverse components of the electrical field prevent the electrons from returning to the ion core after ionization, the mechanism of HHG is remarkably sensitive to the ellipticity of the driving field [39] (see Chap. 5.1). This fact is exploited for example in the short-pulse generation technique of polarization gating, where conventional multicycle laser pulses are manipulated such that only a single optical cycle can contribute to HHG [40].

As a consequence, the eigenmodes of an EC used for HHG need to be linearly polarized. However, in the most general case, a non-planar ring cavity, as discussed in the previous chapter, causes a geometric rotation of the polarization axis upon one round-trip (Fig. 4.2). This effect is exploited for example in monolithic Nonplanar Ring Oscillator Lasers (together with birefringence of the laser medium) to avoid spatial hole burning [41]. The polarization change per round-trip can be described by a Jones Matrix - more specifically a simple rotation matrix in the case of our cavity, since reflections on the cavity mirrors cause a rotation of the polarization axis, but no change of its ellipticity⁴⁰. The polarization state of the eigenmodes follows from an eigenvector-analysis of the Jones Matrix [42], which, for a rotation matrix, yields complex eigenvectors, meaning elliptical polarization. A four-mirror non-planar fsEC cavity has been reported in [37], however its eigenmodes are circularly polarized, as required by the particular application (of creating a longitudinally polarized positron beam by Compton scattering of a high-intensity circularly polarized laser beam).

With a total of 8 mirrors constituting the cavity, a very straightforward and easy-to-align approach has been chosen to entirely avoid a rotation of the polarization axis upon a cavity round-trip. All mirrors are arranged in two horizontal planes and whenever a segment of the beam path is connecting mirrors at different height, it is made sure that the preceding and subsequent segments lie in the same vertical plane. Therefore a set of four mirrors aligned in a vertical plane is required to raise (M1-M4) or lower (M4-M7) the beam in a

⁴⁰ As a side note, a slight rotation of the polarization axis even occurs for standard planar ring cavities due to different s- and p-wave reflectivities of the mirror substrates. This effect can be used for Hänsch-Couillaud locking (Chap. 4.5) even without another strongly polarization-selective element inside the cavity such as a Brewster plate. For the high-energy physics experiment described in [37] this effect was deliberately counteracted in the design of the four-mirror non-planar cavity.

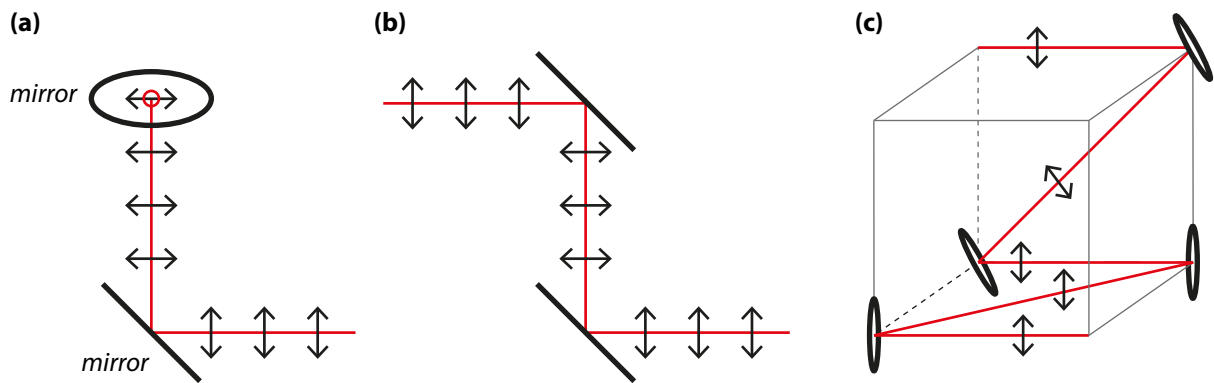


Figure 4.2 As soon as an optical beam leaves a single defined plane, a geometric rotation of the polarization axis can occur. (a) Even a simple beam periscope that rotates the output beam by 90° with respect to the input beam can change the polarization state from p-polarized to s-polarized, for example. This can be an easy pitfall in common setups. (b,c) The polarization state is however conserved if the input and the output beam lie in the same (vertical) plane.

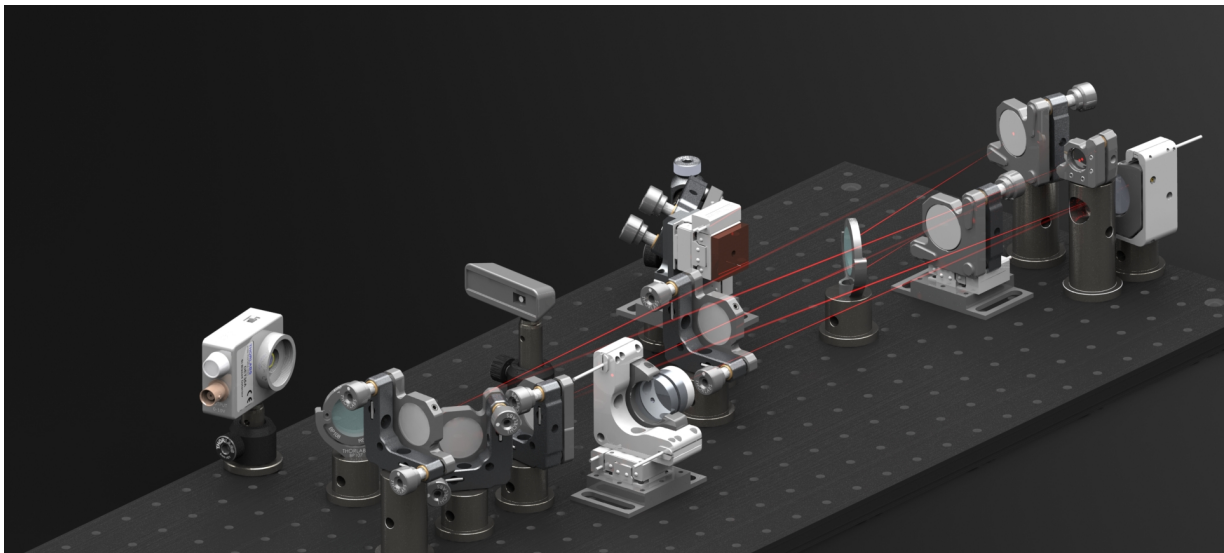


Figure 4.3

Z-shape, that can be thought of as "non-rotated" polarization-preserving beam periscope (Fig. 4.2).

4.3 Geometrical alignment

Several degrees of freedom need to be controlled individually for the cavity:

- The cavity round-trip length (which needs to match the repetition rate of the femtosecond oscillator) is controlled mainly by translating M8 using a translation stage and a fast piezo actuator.

- The primary intracavity focus size is controlled primarily via the separation distance of the two focusing mirrors using a translation stage for M7.
- Beam shift and tilt are changed via remote-controlled mirror mounts for M1 and M8, to ensure that the optical axis of subsequent round trips inside the cavity are collinear⁴¹.

As opposed to a linear cavity, none of these degrees of freedom are independent for a ring cavity. This makes it significantly more challenging to establish and maintain proper alignment and requires a structured approach for iterative adjustments.

The steps for the cavity alignment starting with the initial setup were as follows:

- All mirrors were positioned approximately according to Fig. 4.1, with critical distances (especially the total cavity length) determined using a tape measure. Apart from the three-dimensional geometry described in chapters 3.3.2 and 4.2, an additional design constraint for the placement of the folding mirrors was to locate them at sufficient distance from the secondary intracavity focus in order to avoid damage to the dielectric coatings.
- All mirrors after the input coupling mirror were adjusted in succession, to steer the input beam through the cavity while making sure to
 - maintain consistent beam heights (using a movable reference marker)
 - illuminate mirrors close to center
 - adjust for appropriate (and equal) incidence angles on both focusing mirrors
 - avoid beam clipping with some safety margin (to leave room for future fine adjustments and parameter changes).
- Coarse collinearity of all further cavity round-trips was assured with the help of two pinhole apertures. The apertures were aligned to the intracavity beam on its path between M1 and M8, then those mirrors were used to align the second round-trip through the apertures (Fig. 4.4).

It can be a useful trick to chop the beam somewhere after the second pinhole (e.g by periodically blocking it manually with a paper card) to more easily distinguish the spot of the second pass from that of the first pass on the pinholes. Due to space constraints of the three-dimensional layout making it potentially challenging to position the first pinhole, a slight variation of the scheme was sometimes implemented: The incoupling mirror was temporarily replaced by an aperture with dimensions equal to the mirror substrate, and used to adjust M8 in a single step. After that the incoupling mirror was reinstalled and adjusted for collinearity of the second and first pass. A simple piece of lens cleaning paper could often be used successfully as a makeshift “aperture”

⁴¹ The statement is equivalent to requiring that the optical axes of the incoming light and the cavity eigenmode building up inside the cavity are collinear.

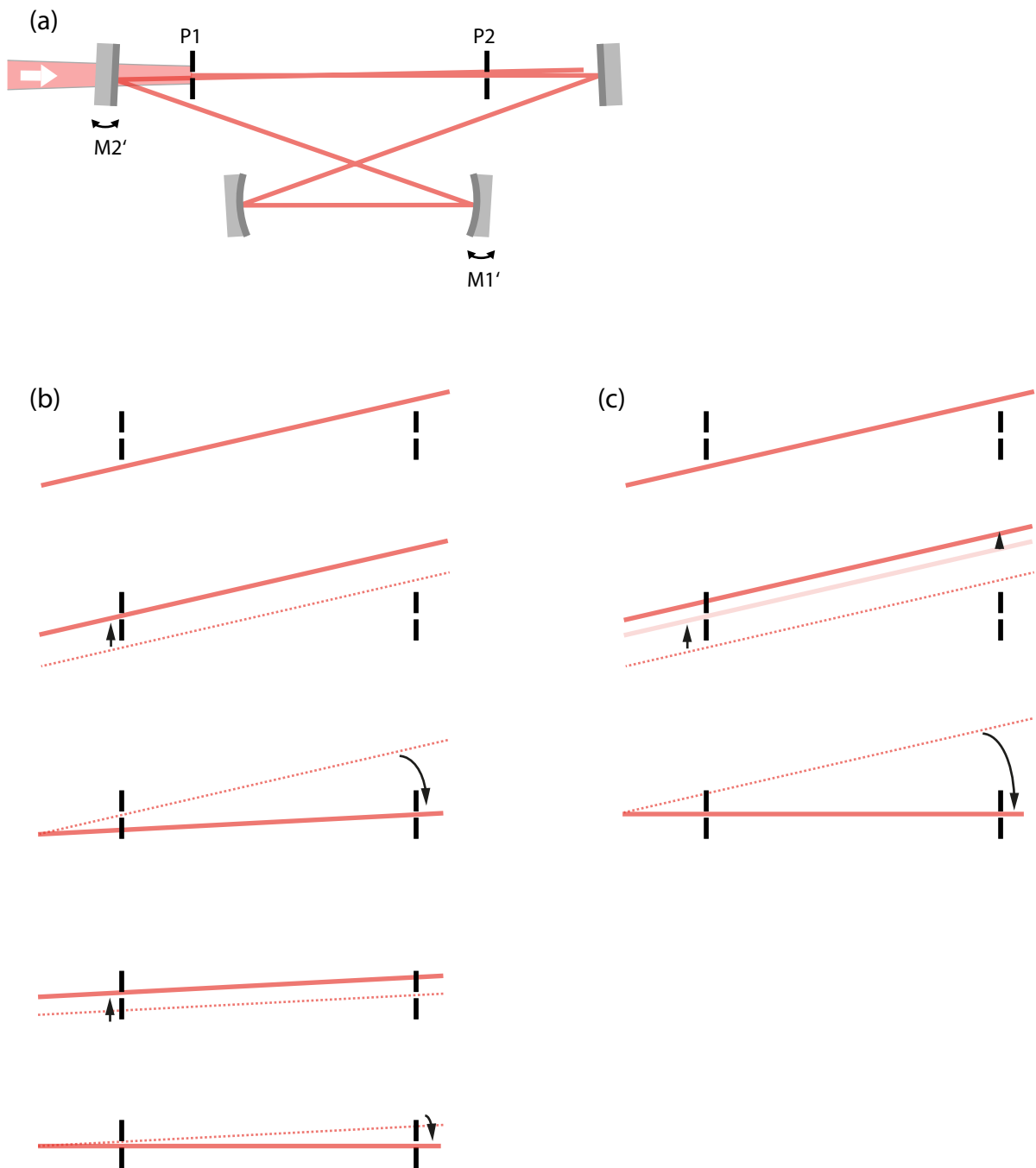


Figure 4.4 (a) Schematic illustration of coarse cavity alignment using two apertures (with mirrors M1' and M2' taking the roles of M8 and M1 in Fig. 4.1). Mirrors M1' and M2' are used to align the second pass beam through pinholes P1 and P2 which are placed coaxially with the first pass beam. (b) Conceptual illustration of efficient beam-walking. To a first approximation the distant mirror M1' causes a translation of the beam whereas the close mirror M2' only causes a tilt of the beam. The alignment procedure converges if M1' is used to target P1, and M2' is used to target P2 in an iterative fashion (separately for both horizontal and vertical planes). (c) The convergence rate can be increased (number of necessary steps decreased) if the alignment with M1' is always slightly "overdone" in the direction of increasing distance from P2.

(even very close to mirrors) since it allows part of the laser beam to pass, while making successive passes visible through diffuse scattering at the same time.

- To spatially mode-match the input beam to the cavity eigenmode, a two-lens telescope is used, which focuses the input beam to match the secondary intracavity waist at its correct position between mirrors M2 and M3.

As a starting point, appropriate focal lengths and lens positions have been calculated using Gaussian beam propagation, based on the beam parameters of the frequency comb output. Those have been determined by measuring beam profiles at different distances from the exit aperture with a CCD-based beam profiler (WinCamD Series) and fitting them with an axial Gaussian beam profile. (The respective values are as follows. Focal lengths of the lenses: 1000 mm, 750 mm; distance of the first lens to the femtosecond oscillator: 920 mm; distance between the lenses: 2430 mm; distance of the second lens to the secondary intracavity waist: 890 mm).

Since the position of the focus inside the cavity is especially critical, it was adjusted by placing an IR viewer card at the correct position of the secondary intracavity focus and moving the second telescope lens longitudinally until the smallest possible cross-section became visible.

- At that point, overlap between the cavity eigenmode and the incoming beam was sufficiently good to observe the resonance condition being fulfilled if the Ti:Sa oscillator is operated in continuous wave mode. Constructive interference occurred periodically with changing cavity length (Fig. 3.2) which was randomly modulated through vibrational noise. The corresponding variation of the intracavity power could be observed as “flickering” of the light scattered from the cavity mirrors through an IR viewer.

When the Ti:Sa oscillator is modelocked however, search for the resonance condition is more involved. The correct cavity length exactly matching the comb repetition rate has to be found, and the comb offset frequency has to be adjusted appropriately (Fig. 3.6). Since it is unlikely that the second requirement is exactly fulfilled when searching for the correct cavity length, the resonance peak will potentially be very weak. (The fact that it is observable at all, is owed to the resonance peaks of the rather low-finesse enhancement cavity having a much larger linewidth than the comb modes.) Therefore, the cavity alignment must first be optimized much more thoroughly to increase the chances of detecting a resonance peak when scanning the cavity length in the next step.

For further alignment, the quality of the coupling to the cavity eigenmode was monitored (off-resonance) by imaging the secondary intracavity focus. This could be easily done by picking up the low-intensity leak signal of mirror M2 to image the intracavity focus directly onto a CCD sensor outside the cavity (CCD1 in Fig. 4.1), without the need for further imaging optics which might introduce aberrations. A standard webcam (Logitech HD Webcam C270) with the infrared filter removed, has been used as a very low-cost sensor for this purpose (Fig. 4.5). The optimization was done off-resonance (Ti:Sa in modelocked operation and cavity length still unmatched) to observe a stable

signal, by walking mirrors M1 and M8 as well as the telescope lenses. Compared to the use of an integrating detector, the visual feedback provided helpful additional clues for reliable and quick realignment (Fig. 4.6). This is especially true for the evacuated chamber, where access and remote control is very restricted (Fig. 4.7) and when changes to the focusing mirror separation significantly disturb the alignment.

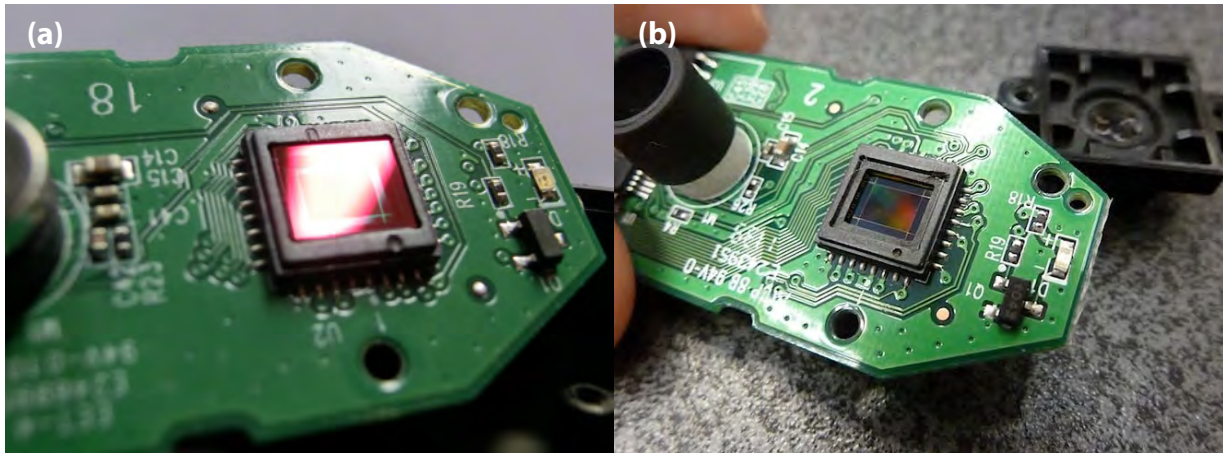


Figure 4.5 (a) Disassembled Logitech HD Webcam C270 with infrared filter still in place. The filter is visible as a very thin brittle reddish plate directly glued to the sensor frame at very small distance from the sensor. (b) View at the CCD sensor - which is intrinsically very sensitive to wavelengths around 800 nm - after the filter has been removed. Sensors have been damaged on a few attempts to heat the glue with hot air and pry away the filter glass with sharp tools. It proved to be a much more reliable method to glue some similarly sized rod/stamp to the filter (preferably with fast-curing epoxy glue) and remove the filter in one piece using a pull-and-tilt motion.

- The cavity length was scanned by moving M8 in small steps while modulating its length via the ring piezo. Several resonance peaks of increasing intensity occur when approaching the cavity length which realizes perfect spectral mode matching (see Chap. 4.5). This can be most directly understood in the time-domain picture: The pulse “copies” from different round trips start to overlap (due to the pump repetition rate increasingly matching the EC length) as their carrier wave periodically realizes the 2π phase shift (Fig. 3.2) needed for constructive interference. Since the spatial length of the 25 fs pulses is only about $7.5 \mu\text{m}$ compared to a typical error of the cavity length after initial setup of 5 – 10 mm, the scan of the cavity length with the discontinuous piezo-actuated translation stage needs to be done in very small steps and takes some time. An example of an automated cavity length scan over the resonance is shown in Fig. 4.8.

In earlier attempts, the correct cavity length was alternatively determined using an autocorrelation measurement intended to detect pulse overlap without being overly sensitive to perfect spectral and spatial modematching inside the EC. The input coupling mirror was replaced by an uncoated substrate, so that pulses reflected at the input and transmitted after a single round trip were of similar intensity. Both were focused onto a BBO crystal, to detect pulse overlap (and thereby the correct cavity length) via an increase in the second harmonic signal.

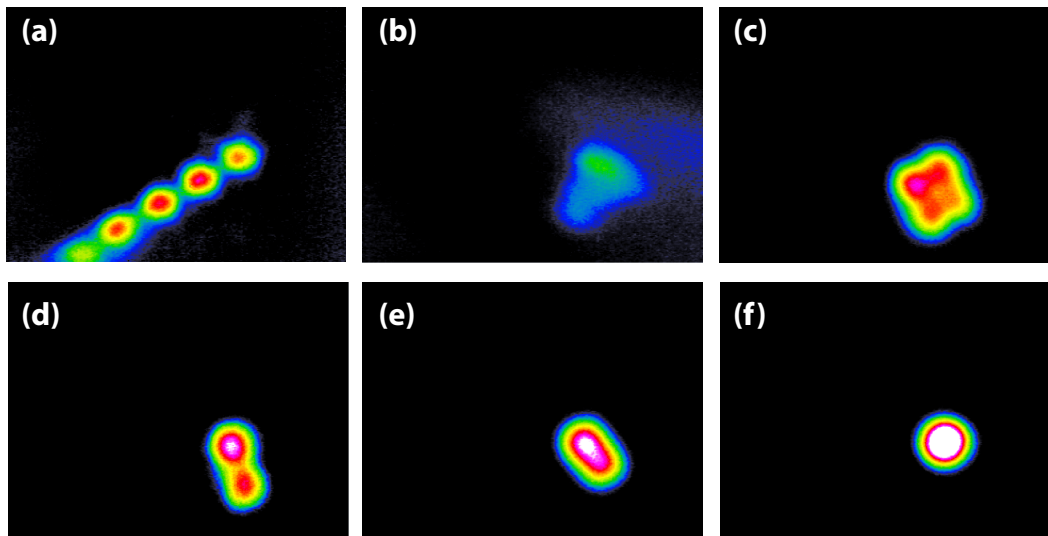


Figure 4.6 Using a live view of the secondary intracavity focus, remote-controlled alignment of the cavity can be performed reliably, with clear clues towards the axis and direction requiring adjustment. (a) For a somewhat misaligned cavity, subsequent round trips of the beam are visible as distinctively separated spots. Their relative size can be used to judge the quality of the mode matching while adjusting the telescope lenses - equal size and many visible roundtrips indicate good mode matching. Once adjusted to the same size, the sensor position can be moved longitudinally to minimize their size to make sure that the actual waist is being imaged, which increases the precision of the following steps. Alignment of the beam axis this far from optimum would be hard to recover when using only an integrating detector (photodiode). (b) Example of bad mode-matching. Light from subsequent round trips is completely blurred out. (c) Misalignment in both orthogonal planes is visible. (d,e) Getting close to proper alignment. The eigenmode of the cavity is building up, marked by the brightest spot which now stays stationary while moving around the “tail” by walking mirrors M1 and M8. Its intensity increases as overlap and parallelism of the incoupled beam with the eigenmode is improved. Since only one plane inside the cavity is observed, the required direction of the mirror adjustments is not known in advance (as in Fig. 4.4(a)), but obvious from the immediate feedback if following this procedure: First maximize the intensity by adjusting all axes of both mirrors independently. Then, iteratively for both horizontal and vertical plane, closely oscillate around the current optimum position using one mirror while adjusting the other one to further maximize the brightness at that position. To reliably judge small intensity changes, it is helpful to regularly readjust the camera gain, so that the brightest spot at its current optimum just barely starts clipping. (f) Perfectly aligned cavity

Yet another indication of approaching the cavity resonance can be changes in the transmitted spectrum (see Fig. 4.12).

4.4 Dispersion management

Every pass through an optical medium, or reflection from dielectric mirror coating introduces a certain amount of (mostly positive) GDD - and thereby temporal broadening - to laser pulses. With respect to the experiment design, there are two aspects to this: Firstly,

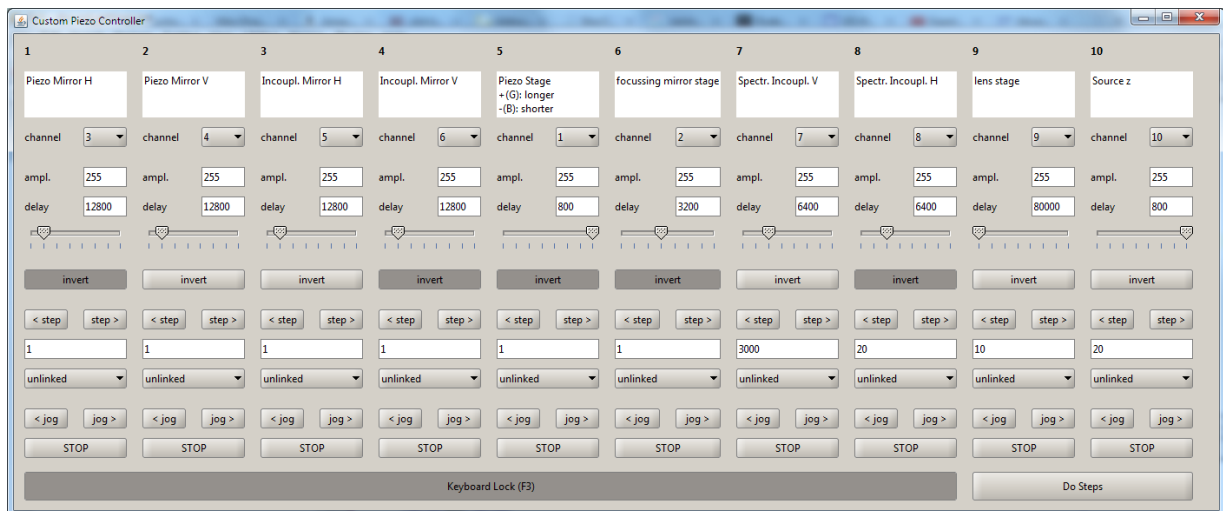


Figure 4.7 Custom software interface for the remote-controlled actuators. A configuration of intuitive key-bindings allows for convenient beam-walking using only a (wireless) keyboard.

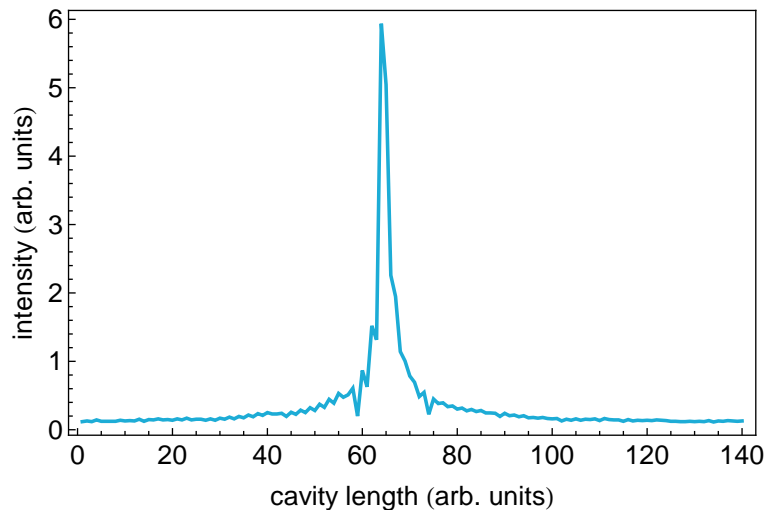


Figure 4.8 Increase in intracavity power when approaching the resonant cavity length. In an automated scan of the cavity length at the smallest possible step size of the translation stage (~ 50 nm) a signal trace over a full piezo modulation period (~ 100 nm) is recorded and the maximum value plotted, giving the envelope of the individual resonance peaks. This way, even with discrete steps of the translation stage, the main resonance is not easily missed.

in order for the pulses exiting the femtosecond oscillator to keep their shortest possible (Fourier-limited) pulse length, we needed to compensate the cumulative GDD of about 570 fs^2 added before entering the EC by mode-matching optics, vacuum chamber window, incoupling mirror substrate and propagation in air, as summarized in Table. 4.1. Secondly, the GDD per round trip inside the EC needs to be as close to zero as possible, to avoid pulse broadening for each subsequent round trip (equating to a frequency-dependent FSR in the frequency-domain picture of Fig. 3.6) which would severely reduce the coupling efficiency to the cavity.

element	GVD	L	GDD (fs ²)
BK7 lens 1	44.7 fs ² /mm	2.2 mm	98.3
BK7 lens 2	44.7 fs ² /mm	2.2 mm	98.3
FS mirror	35.9 fs ² /mm	6.35 mm	227.9
FS window	35.9 fs ² /mm	1 mm	35.9
FS filter	35.9 fs ² /mm	2 mm	71.8
air	20 fs ² /m	2 m	40
chirped mirror	-40 fs ²	14 bounces	-560
Σ			12.3

Table 4.1 Contributions to pulse broadening through added GDD.

Initially, pre-compression of the pulses was done using a prism-compressor (Fig. 4.9) which allowed to finetune the amount of negative GDD. However, for ease of alignment and a smaller amount of third-order dispersion (TOD), the prism-compressor was later replaced by using multiple reflections on chirped mirrors (Layertec), introducing a GDD of -40 fs^2 per bounce (see Fig. 4.1).

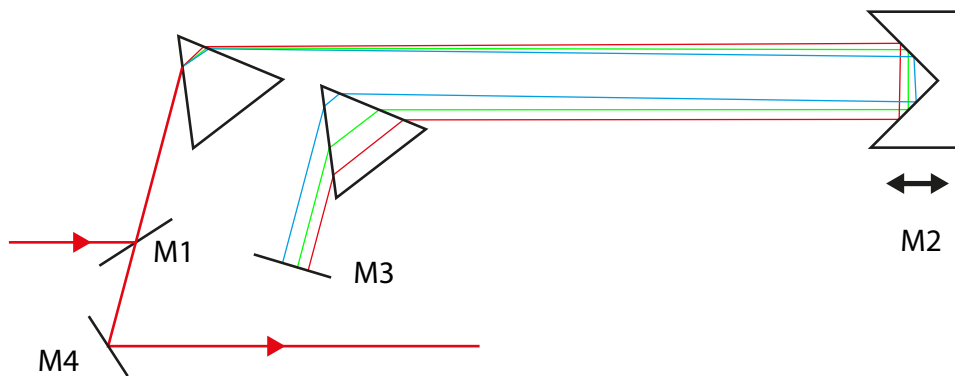


Figure 4.9 Prism Compressor with wide adjustment range. The typical number of four Brewster angle prisms to angularly disperse, collimate and refocus the beam is reduced to two, by symmetrically folding the beam path using the end mirror M3. The amount of GDD can be adjusted (in principle without further alignment) by moving the retroreflecting mirror pair mounted on a translation stage, which changes the optical path length between the prism pair for both passes. The returning beam is aligned slightly out-of-plane, so that it can pass above the input mirror M1.

The cavity mirror coatings were specifically chosen to yield zero GDD per round trip. Typically they were specified for a GDD of $< 20 \text{ fs}^2$ which leaves a certain range of variation. After a bit of trial and error in selecting (and mixing them with mirrors of slightly negative GDD, if necessary) while accounting for the dispersion of the HHG outcoupling element, the original goal of zero net GDD could be realized. In this respect it was very useful to use the potential asymmetry of the resonance peaks (Fig. 4.10) as a direct (and signed) indicator of the amount of residual GDD. Final proof of a successful end result was the observation of the full seed spectrum being coupled into the cavity (see Fig. 5.7(a)).

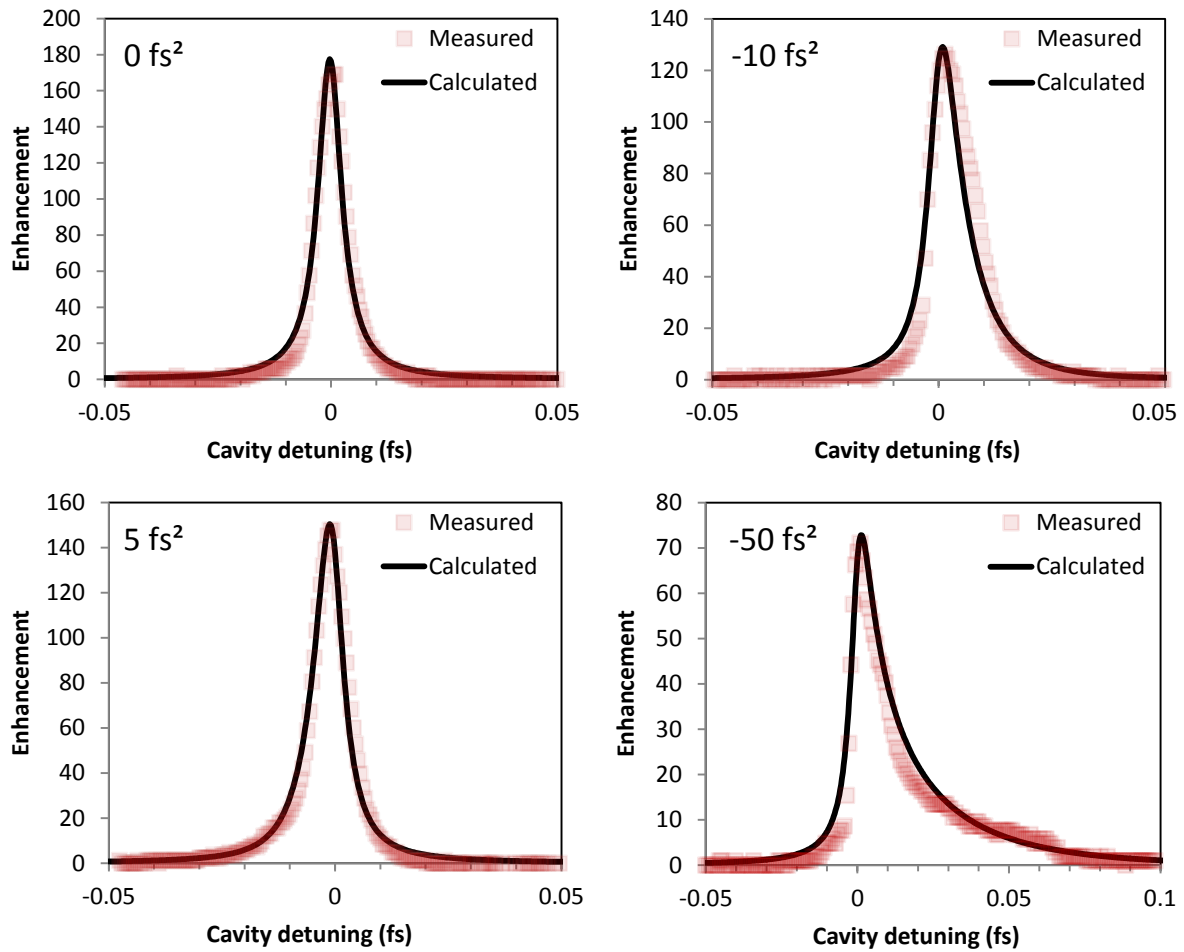


Figure 4.10 Measured resonance peaks for different amounts of intracavity GDD fitted according to Chap. 3.2.2. Both amount and sign of the deviation from zero GDD is directly obvious from the cavity length scans. (The cavity length detuning from resonance Δx is plotted as a time delay $\Delta x/c$.)

4.5 Spectral mode matching and cavity lock

To ensure best spectral overlap of the EC with the frequency comb according to the requirements summarized in Fig. 3.6 the cavity length was actively locked to the comb repetition rate, while the carrier-envelope offset (CEO) frequency of the comb was manually tuned for maximum intracavity power.

Exploiting the presence of the outcoupling plate as a strongly polarization selective element a Hänsch-Couillaud scheme [43] was used to derive the error signal (Fig. 4.11) for feedback to the cavity length via the ring piezo of mirror M8. The comb repetition rate itself was stabilized to a fixed 108 MHz, derived from the external rubidium RF reference.

The carrier envelope offset of the oscillator was stable enough to be manually adjusted for optimal power enhancement.

The influence of those two degrees of freedom on the intracavity spectrum could be nicely observed, as demonstrated in Fig. 4.12.

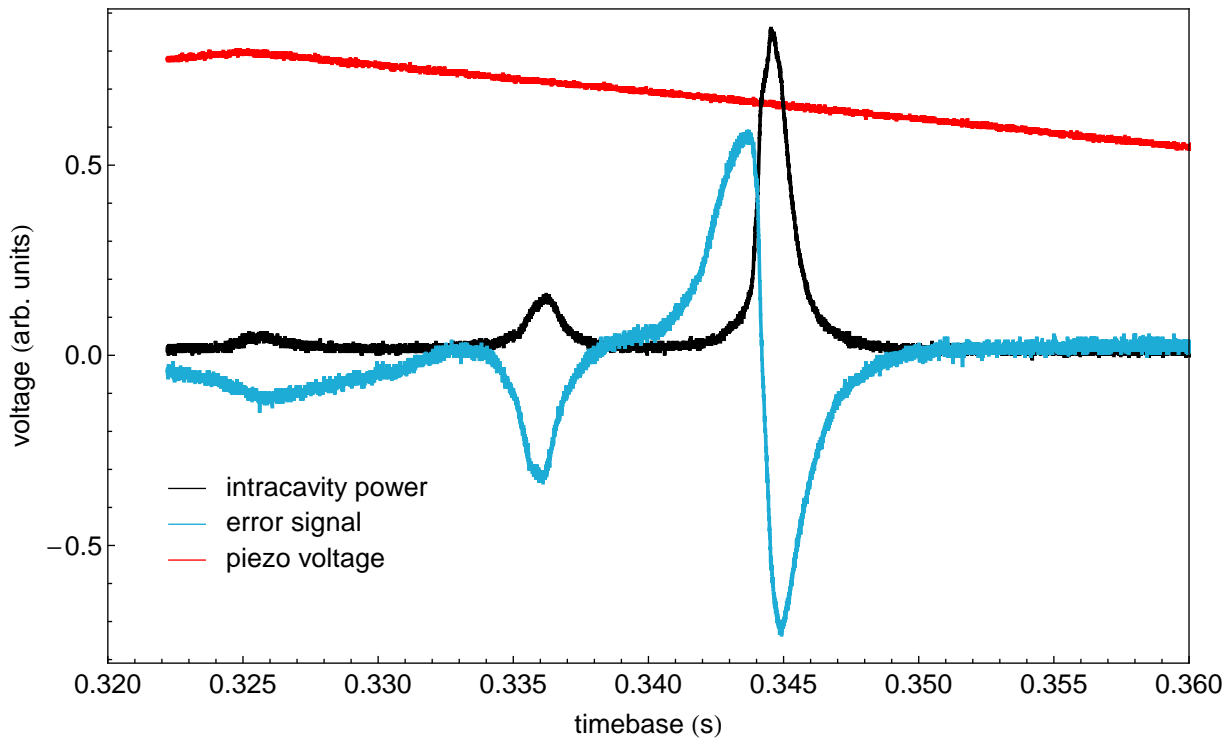


Figure 4.11 Linear (sawtooth) cavity length scan showing a resonance peak of the intracavity power and a typical error signal. The secondary peaks are caused by the excitation of higher-order modes which have different resonance frequencies.

4.6 Vacuum system and vibration isolation

In retrospect, quite a large amount of planning, troubleshooting and reconfiguration went into the design of the connection between vacuum chamber, optical table (Thorlabs/Nexus T1230D with pneumatic legs), vacuum pumps and optical assembly, to suppress effects of mechanical vibrations as good as possible. Initially, the custom-made stainless steel chamber with inner dimensions of $330 \times 780 \times 145$ mm was designed with 5 feed-through holes in the bottom, so that a breadboard inside the chamber could be connected directly to the optical table via 2-inch pillars, as illustrated in Fig. 4.13. Disconnected from the breadboard, the chamber itself rested on the optical table on a total of 10 SorbothaneTM rubber feet to absorb residual vibration coming from the vacuum pumps. The turbo pump (Pfeiffer HiPace 300) was directly flanged to the chamber wall and connected to the roughing pump (Pfeiffer ACP15 roots pump) via a flexible corrugated hose. Typically, the cavity was operated with a background pressure on the order of 10^{-4} mbar.

Operating the EC inside an evacuated cavity provides excellent isolation against direct airborne acoustic disturbances, so that no further shielding should be required. However, as evidenced by the time traces of Fig. 4.14, it turned out that the stability of the intracavity power was much worse than expected, especially for power enhancement values above 100. Based on the assumption that mechanical instabilities in the setup (including

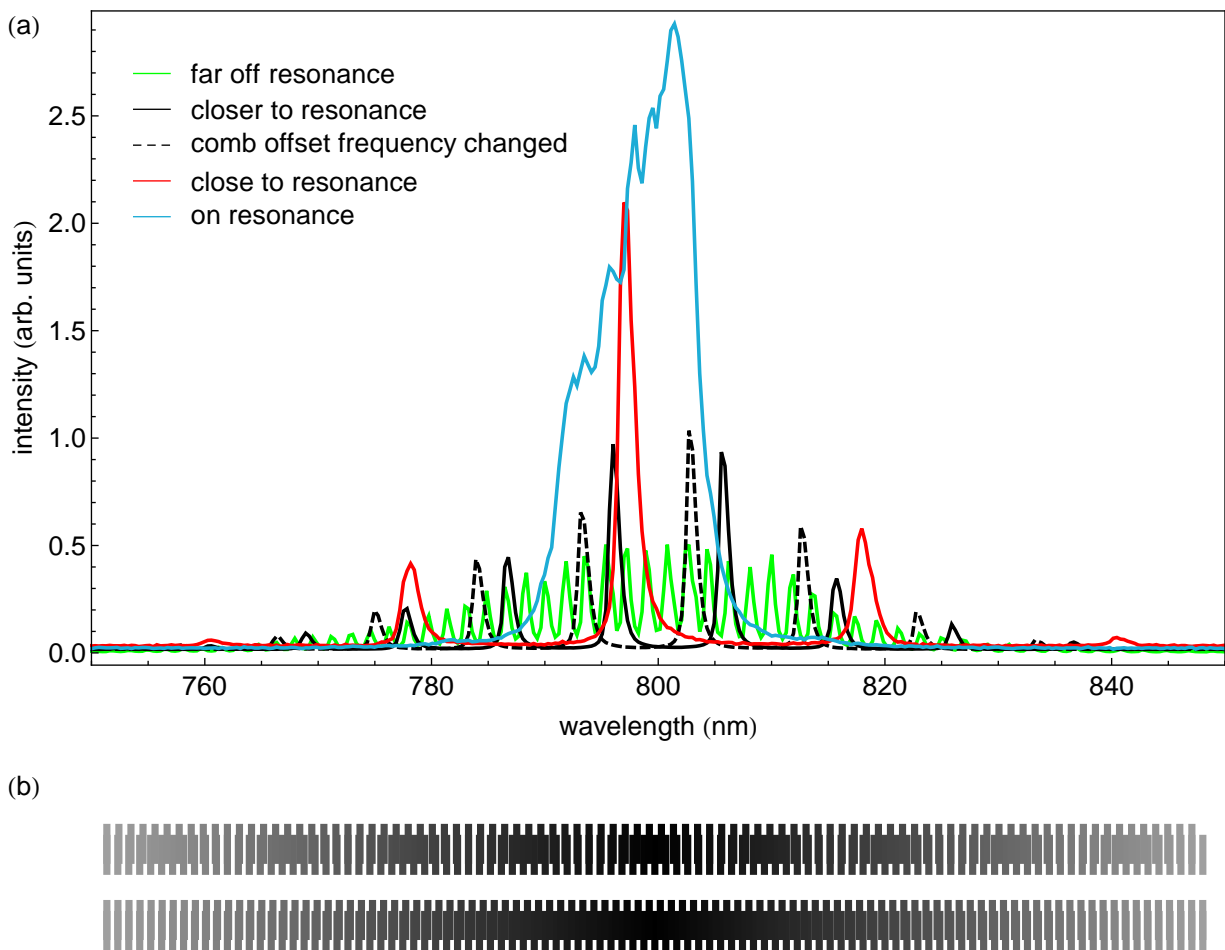


Figure 4.12 (a) Intracavity spectrum measured for varying deviation from the optimal resonant cavity length. Peaks in the spectrum increasingly space out for improved spectral modematching until the full frequency comb spectrum centered at 800 nm is coupled into the cavity under optimal conditions. The position of the peaks is changed collectively when changing the frequency comb offset. (b) Moiré pattern resulting from overlaying two line patterns with slightly different periodicity. The effect can serve to visualize how a mismatch between the cavity modes and the frequency comb modes leads to spikes in the enhanced spectrum defined by their overlap integral.

the elevated separate breadboard) were the source of the problem, several iterations of the design were tested:

- We reduced the height of all optical posts as much as possible and replaced remaining variable-height 1-inch posts by solid fixed-height 2-inch posts. The “second-level” mirror M2 was initially mounted from the side, so that its post does not obstruct the beam coming from mirror M1. We switched to mounting it from below using a 2-inch post as well, but drilled a sufficiently large hole to allow the beam below to pass.
- The thin aluminum breadboard was reinforced using solid 3cm × 3cm iron beams.

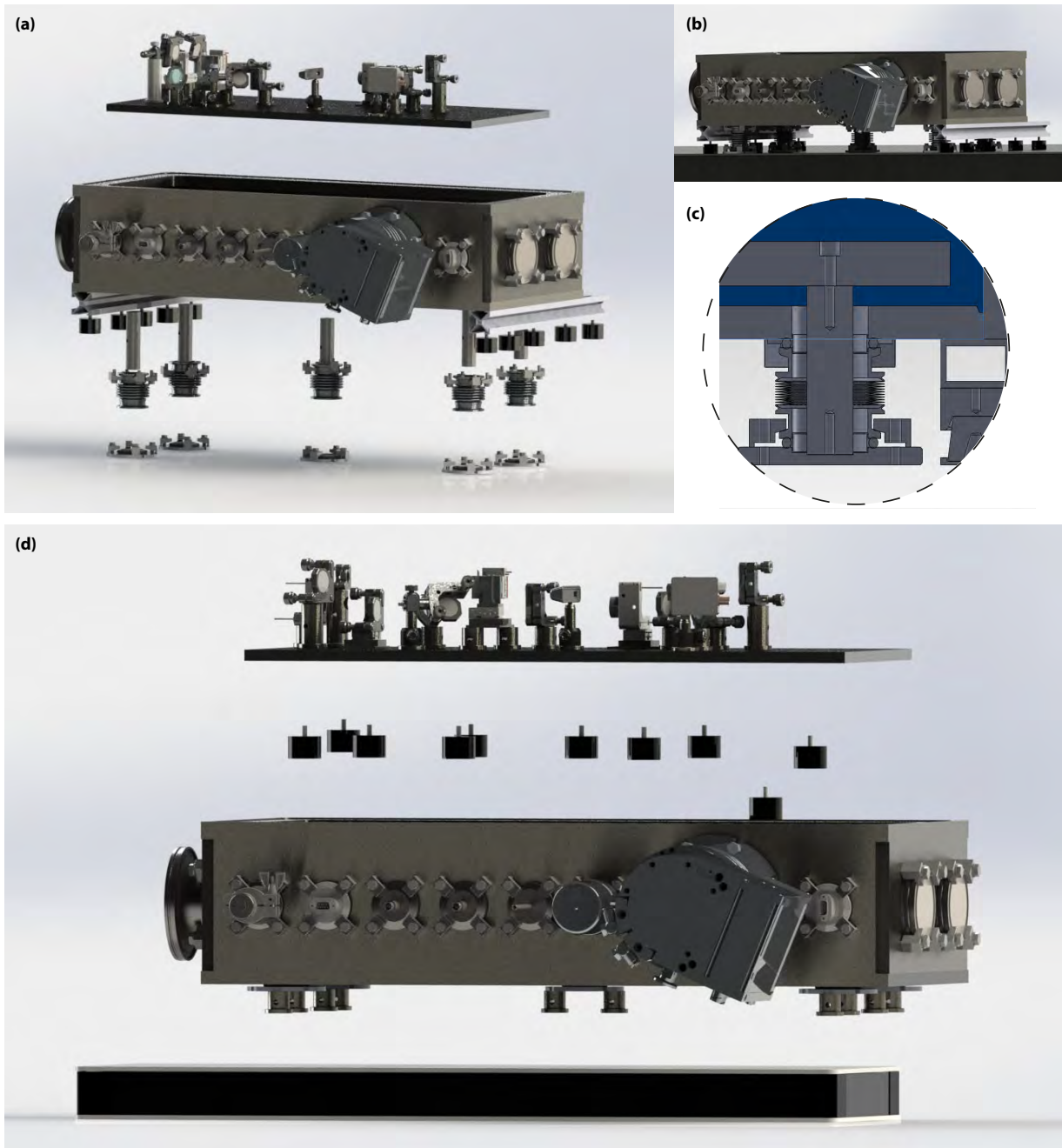


Figure 4.13 (a, b) Vacuum chamber design as initially planned. The 5 pillars supporting the breadboard pass through holes in the chamber bottom which are vacuum-sealed by vibration-isolating bellows. The chamber rests on two aluminum beams with Sorbothane rubber feet. The beams are slightly protruding to balance the weight of the turbo pump and prevent the chamber from tilting by keeping the center of mass of the assembly centered with respect to the rubber feet. The lid was fabricated out of a 2 cm thick transparent acrylic glass plate with two handles. The vacuum seal is formed by the polished metal rim of the chamber and an O-ring clamped inside a dovetail groove cut into the lid plate. (This design is practically very useful, as the contact surface of the softer plastic is protected from scratching by the O-ring which itself is prevented from falling out thanks to the groove geometry, when opening and closing the chamber.) The chamber features numerous general-purpose flanges (of which there can never be enough), to allow connection of diagnostics, actuators, sensors and gas lines. (c) Detail view of the bottom feedthrough. (d) Final reconfiguration of the chamber assembly: The chamber was mounted directly to the optical table with an additional breadboard as a spacer to maintain the initial beam height. The breadboard with the optical setup was simply placed on the rubber absorbers inside the chamber.

- It was tried to dampen vibrations by strategic positioning lead weights at vibration antinodes of the breadboard.
- The entire optical setup was rebuilt on a much stiffer honeycomb breadboard. However it would not have been possible to use it inside the vacuum chamber due to size constraints and vacuum compatibility issues.
- The aluminum pillars supporting the breadboard were replaced with custom-made versions, fabricated out of more ductile nylon material.
- For comparison, a simpler planar cavity was built, to further rule out mechanical instabilities or alignment sensitivity specific to the three-dimensional layout as the problem source.
- Finally the EC was rebuilt directly on the optical table.

All measures entailed only insignificant improvement - even when combined. This observation led us to look more closely at the actual vibration characteristics of the optical table.

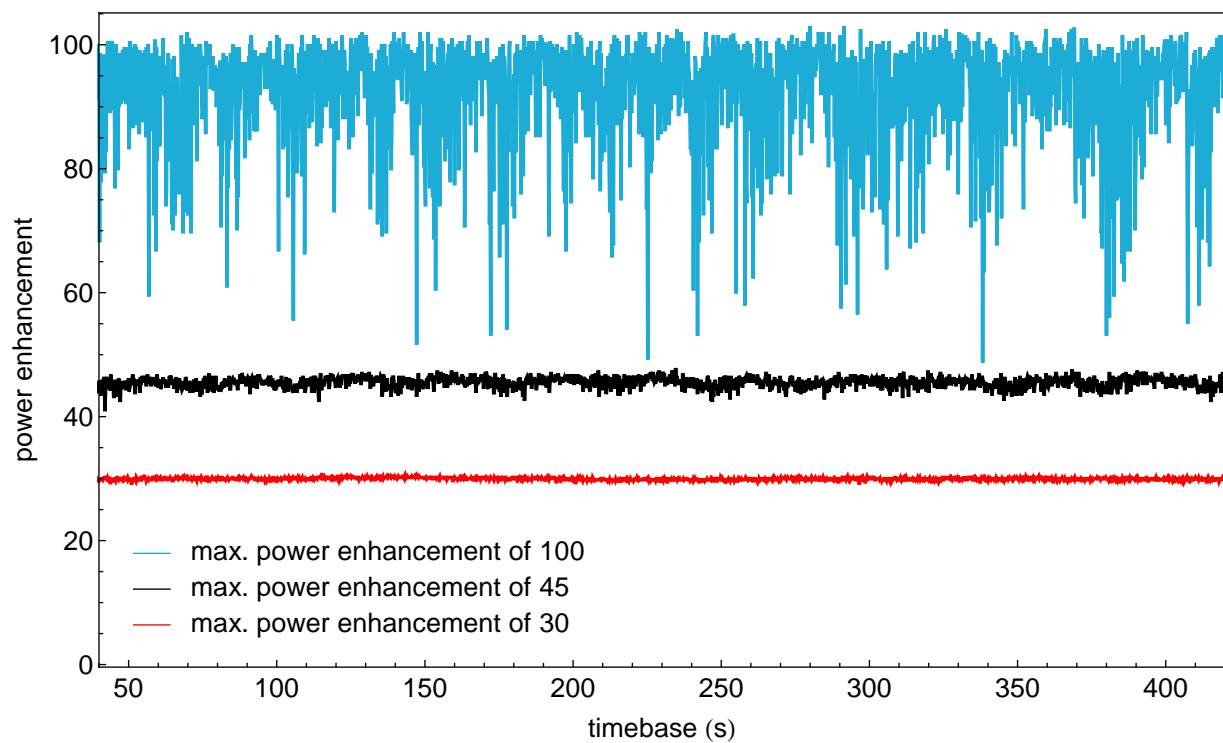


Figure 4.14 Fluctuations of the intracavity power for the initial chamber design when the cavity is locked and the chamber evacuated.

An accelerometer-based transducer connected to a vibration signal-analyzer (OROS Systems) was used to investigate them quantitatively. As it turns out, while the optical table

is good at damping (seismic) frequencies below 50 Hz (in agreement with its specifications), it exhibits self-resonances at higher frequencies and a very obvious susceptibility to picking up acoustic vibrations from the noisy lab environment. With the sensor head directly fixed to the surface of the optical table, a strong frequency peak around 360 Hz could be observed (Fig. 4.15). The same peak was evident in the frequency spectrum of the intracavity power, obtained by a fast Fourier transform (FFT) of the recorded oscilloscope trace. Since the peak could not be significantly reduced by getting rid of any particular noise source in the lab, but could be amplified by random excitation (knocking) of the optical table, it is most likely an eigenresonance of the optical table. Other frequencies could be unambiguously excited by generating sine tones at corresponding frequencies via a loudspeaker inside the lab. It could be excluded that this response was due to the measurement probe operating like a microphone - if lifted from the table, or mounted with some rubber material in between, the frequency peaks immediately vanished from the spectrum.

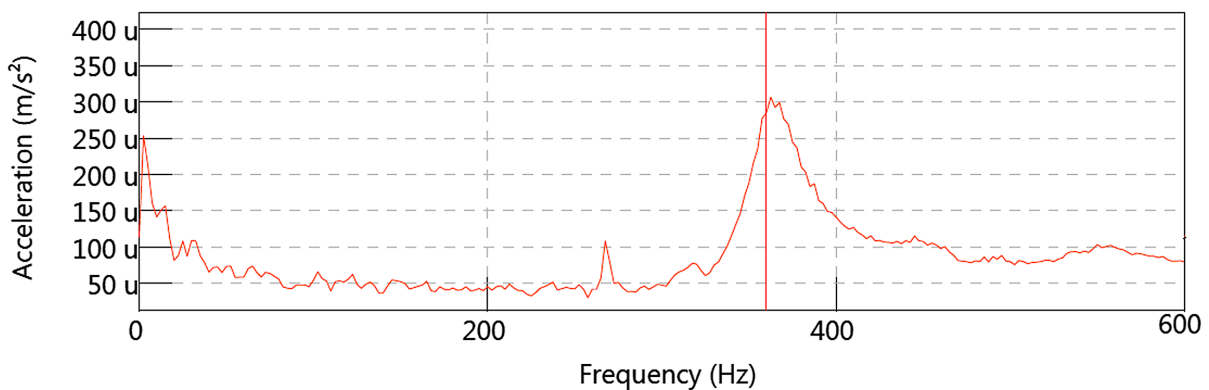


Figure 4.15 Frequency spectrum of vertical vibrations recorded with an accelerometer directly on the surface of the optical table.

Seemingly the optical table worked as a resonator picking up acoustic disturbances over its large surface and propagated them into the vacuum chamber via the metal pillars of the breadboard (which itself is acoustically isolated from the chamber walls by vacuum). From these findings we concluded that a stiff connection between the optics assembly and the optical table is not necessarily the best option and completely rearranged the initial setup: As illustrated in Fig. 4.13 we sealed the bottom feedthroughs and mounted the chamber directly on the optical table. To achieve additional isolation of the optics setup from the optical table, the rubber dampers were reused to support the breadboard inside the chamber. The fact that the EC was then kind of “floating freely” with respect to the input beam originating from the optical table proved to be no issue once it reached an equilibrium position, and peak-to-peak fluctuations of the intracavity power could be reduced to the 10 percent level for power enhancement factors of up to 250.

To put it in other words, the absence of vibration in the EC is much more critical than perfect beam pointing stability of the input laser⁴². To better understand this result, one

has to keep the following in mind: For a fundamentally stable resonator⁴³ fluctuations in intracavity power are either due to fluctuations in the pump, deviation from the resonant cavity length (which can be avoided using a fast-enough feedback loop) or from changing spatial mode matching. Vibrations of the table which are absorbed in the rubber dampers lead to a common-mode movement of all cavity mirrors on the breadboard relative to the optical table, while individual mirrors are excited to vibrate independently in the case of stiff coupling to the optical table. In the latter case, individually changing tilt angles of the cavity mirrors can cause drastic changes to the orientation of the cavity eigenmode with corresponding degradation of the spatial mode matching, whereas a tilt or translation of the entire EC assembly in the former case, has a very predictable, small effect on overlap with the input beam.

No noise contribution by the turbo pump was observed, and the low-frequency vibration of the roughing pump could be very efficiently dampened by tightening its connection hose to large lead weights on the floor⁴⁴.

To summarize, our final findings were more or less the exact opposite of our initial intuitive approach based on the assumptions that “the optical table is the best place to put optics” and “all vacuum pumps need to be mechanically decoupled from the optical table”. However, as we later found out, putting simple additional foam or rubber layers on expensive optical tables to improve the vibration isolation of small optical arrangements is not completely unheard of (see e.g. Ref. [44], chapter 4.3.12)!

4.7 Cavity characterization

We locked the frequency comb to the enhancement cavity at different positions in the stability zone (by varying the focusing mirror separation distance d) and measured the beam waist geometry of both intracavity foci as well as the intracavity power. The secondary focus was directly imaged onto CCD1 via the convergent beam leaking from mirror M2 before the focus. The primary focus was indirectly determined by recording a profile of the divergent beam at known distance after the focus on CCD2 and calculating the corresponding Gaussian beam waist. The measured beam waists in Fig. 4.16(a) show good agreement with the theoretical prediction. We were able to produce a focus with a $1/e^2$ radius as small as $10\ \mu\text{m}$ and an average ellipticity of the beam profile $1 - w_x/w_y$ less than 6 percent, although using a rather large AOI of 4.2° on the focusing mirrors.

⁴² The beam pointing stability is often not great anyway, if large optical paths between the pump source and the external resonator and many steering mirrors are involved.

⁴³ Stability refers to the existence of an eigenmode solution. In practice this requires the distances of the optical elements to comply with the theoretically derived stability criterion Eq. 3.12, as well as sufficiently good pre-alignment to avoid clipping of the eigenmode (derived under the assumption of sufficiently large apertures).

⁴⁴ Similar simple solutions observed in other labs involve the corrugated hose passing through concrete-filled plastic containers.

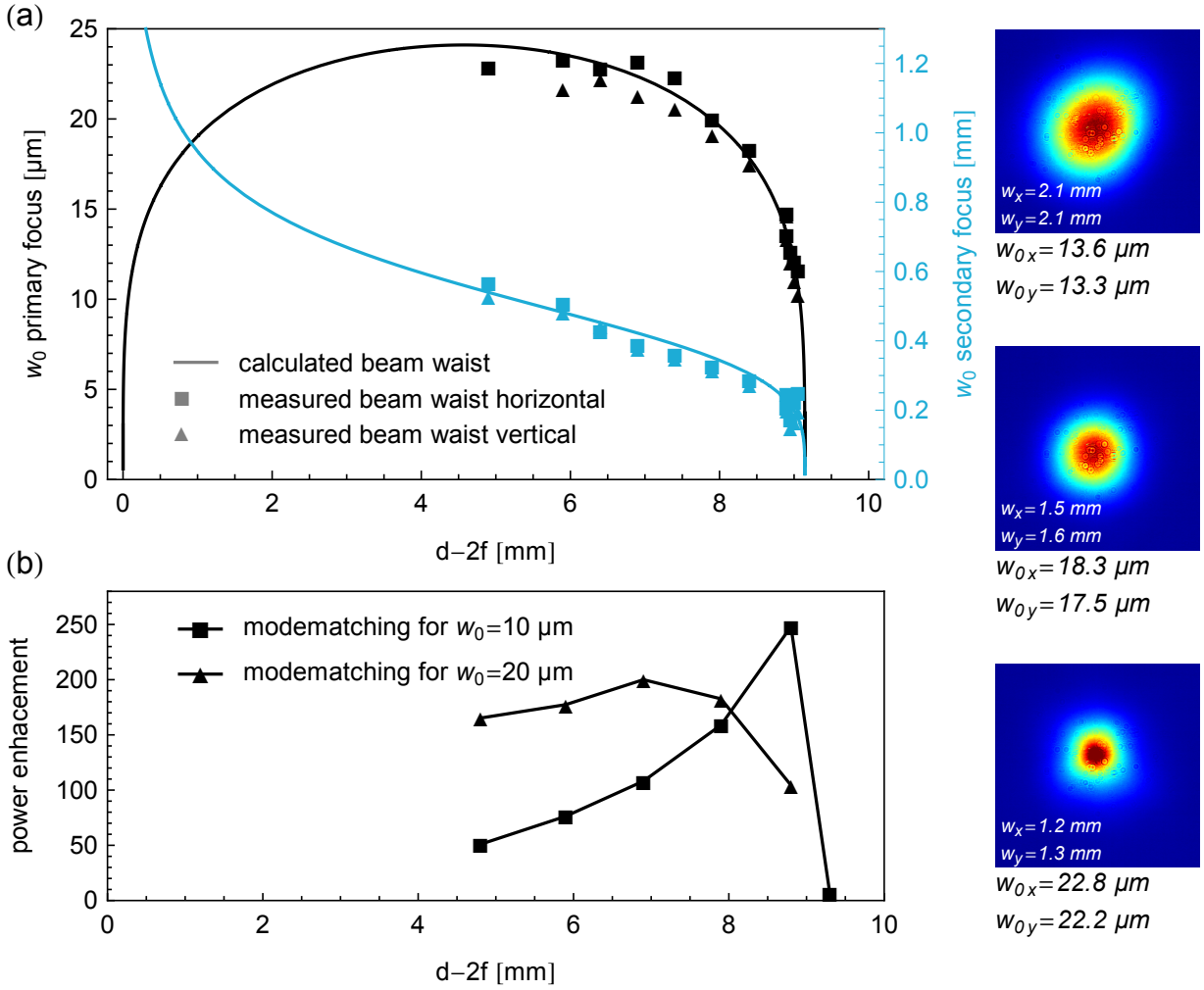


Figure 4.16 Measured beam waists in vertical and horizontal planes for (a) both intracavity foci and (b) corresponding power enhancement. The enhancement factors are given for two different input beam configurations which were kept constant during the measurement. The depicted beam cross sections were measured at a constant distance of 11 cm from the primary focus.

An enhancement factor of 250 was reached (see Fig. 4.16(b)), defined as the ratio of circulating intracavity power P_{circ} to incoming power P_{in} . It is related to the incoupling mirror transmission T_{M1} and the round trip power loss factor L' accounting for all other losses (leakage of all mirrors except the incoupling mirror as well as absorption, scattering and diffraction inside the cavity) by a variation of Eq. 3.3b

$$\frac{P_{circ}}{P_{in}} = \eta_{spectral} \cdot \eta_{spatial} \cdot \frac{T_{M1}}{(1 - \sqrt{(1 - T_{M1})(1 - L')})^2}. \quad (4.1)$$

The added coupling efficiencies η quantify the amount of spectral and spatial overlap of the comb and cavity modes.

We determined the power enhancement by comparing (background-corrected) measurements of the leak signal power P_{M2} behind mirror M2 when the cavity is on resonance

($P_{M2,onres}$), and when the beam is blocked inside the cavity after a single pass behind M2 ($P_{M2,single}$) according to

$$\frac{P_{circ}}{P_{in}} = \frac{P_{M2,onres} T_{M1}}{P_{M2,single}}.$$

For our given enhancement, it was thereby sufficient to measure a power ratio on the order of 10^4 instead of precisely characterizing the transmission of a few parts-per-million of high-reflector M2⁴⁵.

As follows from Eq. 4.1, the measured enhancement is already close to the theoretical limit of about 400, given an input coupler transmission T_{M1} of 1 percent. The pronounced peak in the measured enhancement curves is due to the fact that (spatial) mode matching was not reoptimized for every datapoint.

Based on an additional measurement of the power P_{refl} reflected at the input coupling mirror, it was determined that $L' = 0.16\%$ according to

$$L' = \frac{P_{in} - P_{refl}}{P_{circ}}$$

which follows from energy conservation under steady-state conditions. The low intracavity loss further evidences that the non-planar cavity geometry does not introduce a geometric rotation of the polarization axis, since the polarization selective Brewster outcoupling plate would otherwise have contributed significantly to the loss. From L' follows a cavity finesse of approximately 540 and a combined coupling efficiency $\eta_{spectral}\eta_{spatial} = 84\%$ via Eq. 4.1.

The result for L' also suggest a potential to improve the enhancement by impedance matching the cavity with an incoupling mirror transmission of equal magnitude. Nevertheless it was decided to deliberately accept a slightly decreased enhancement in the overcoupled regime ($T_{M1} > L'$) in order not to risk entering an undercoupled regime ($T_{M1} < L'$) with much stronger associated penalty on intracavity power, when L' increases during operation as a consequence of the nonlinear effect and ionization in the gas used for HHG.

The fsEC did not require realignment for at least 24 hours, which was the longest observation period. Continuous operation was only limited by the long-term stability of the seed frequency comb.

⁴⁵ The Ti:Sa oscillator had a small peak in the infrared in its emitted spectrum, which was not resonant in the EC due to low reflectivity of the mirror coatings at this wavelength. To perform the above measurement reliably, it therefore had to be filtered out before entering the EC.

5 A frequency comb at 160nm via HHG

5.1 High harmonic generation theory

High harmonic generation (HHG) is an extreme form of nonlinear frequency conversion, where an intense laser pulse, focused into a gas, produces very high (odd) harmonics. The required optical intensities are on the order of 10^{13} W/cm² but only a very tiny fraction in the range of 10^{-5} of the fundamental power can currently be converted in a best-case scenario [45–48]. Despite these complications, HHG holds a lot of promise to realize useful tabletop sources of highly coherent short wavelength radiation down to the X-ray region. This hard to reach spectral region is typically only accessible using “bulky” technologies like synchrotrons or free-electron lasers, which also have unfavorable coherence properties for many applications. HHG is entirely unique in its ability to generate optical frequency combs at these wavelengths as precision measurement tools.

The typical structure of a HHG spectrum is illustrated in Fig. 5.1, showing a rapid intensity decrease of the first lower harmonics (perturbative region), followed by many harmonic orders of close to constant intensity (plateau region) that ends with a sharp cut-off. Harmonics above the order of 200 [49] have been observed. Usually noble gases are used for HHG due to their non-reactive nature. High harmonics are emitted co-linearly with the driving laser - often in a beam with better angular confinement⁴⁶.

As commonly encountered in nonlinear optics, there are two aspects to consider: The microscopic response of an isolated atomic oscillator to the incoming field, leading to the (weak) emission of light with a differing spectral composition, and macroscopic effects of phase matching, describing how these individual contributions can interfere to produce a strong perceptible signal. Depending on the intensity of the pump light, the former is described by different models, detailed in the following two sections.

5.1.1 Perturbative harmonic generation

For sufficiently low intensity of the driving field, harmonic generation within a gas target (just like within a solid nonlinear crystal) can be handled within the framework of conventional perturbative nonlinear optics [50]. Typically, the assumption is made that the dipole moment per unit volume, or polarization $P(t)$ of a medium responds instantaneously and nonlinearly to an applied optical field, and its functional dependence is presented as a power series in the field strength $E(t)$ according to

$$P(t) = \epsilon_0[\chi^{(1)}E(t) + \chi^{(2)}E(t)^2 + \chi^{(3)}E(t)^3 + \dots]$$

⁴⁶ The divergence decreases for higher harmonic orders.

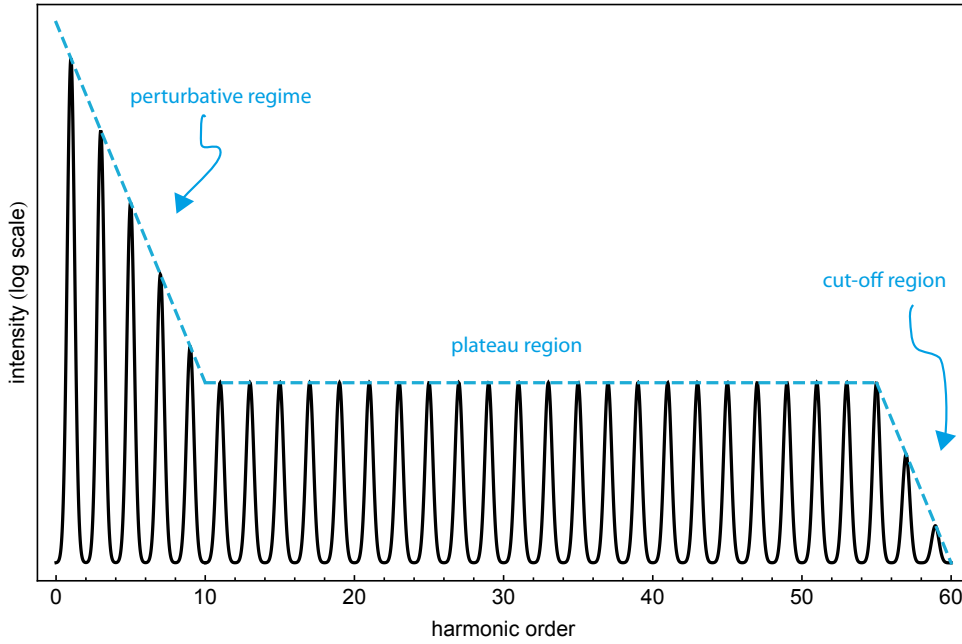


Figure 5.1 HHG spectrum.

where ϵ_0 is the permittivity of free space and the coefficients $\chi^{(n)}$ represent the n -th order susceptibilities⁴⁷. The oscillating dipole then acts as the source of a newly generated field. Each of the coefficients $\chi^{(n)}$ gives rise to specific types of nonlinear effects, among them the generation of an n -th harmonic signal, as obvious from trigonometric relations such as:

$$\begin{aligned}\cos^2 x &= \frac{1}{2}(\cos 2x + 1), \\ \cos^3 x &= \frac{1}{4}(\cos 3x + 3 \cos x), \\ \cos^4 x &= \frac{1}{8}(\cos 4x + 4 \cos 2x + 3), \\ \cos^5 x &= \dots\end{aligned}$$

It can be shown, that for media without inversion symmetry (which includes gases) all even terms in this series are equal to zero, which explains a series of odd harmonics. However, due to the tendency of $\chi^{(n)}$ to rapidly decrease for increasing n , the generation of harmonics much beyond the third order is not efficient. In a quantum picture, this process is analogous to multiphoton absorption (Fig. 5.2(a)) in a barely perturbed atomic potential (which becomes increasingly unlikely for growing n), followed by the emission of a high energy photon. The low-order harmonics in Fig. 5.1 follow this description.

⁴⁷ One should keep in mind that this is by far no universal representation of a nonlinear response. Due to the restriction of P following E instantaneously (no dependence of $P(t)$ on $E(t \pm \Delta t)$), the description even excludes standard effects of linear optics, like dispersion.

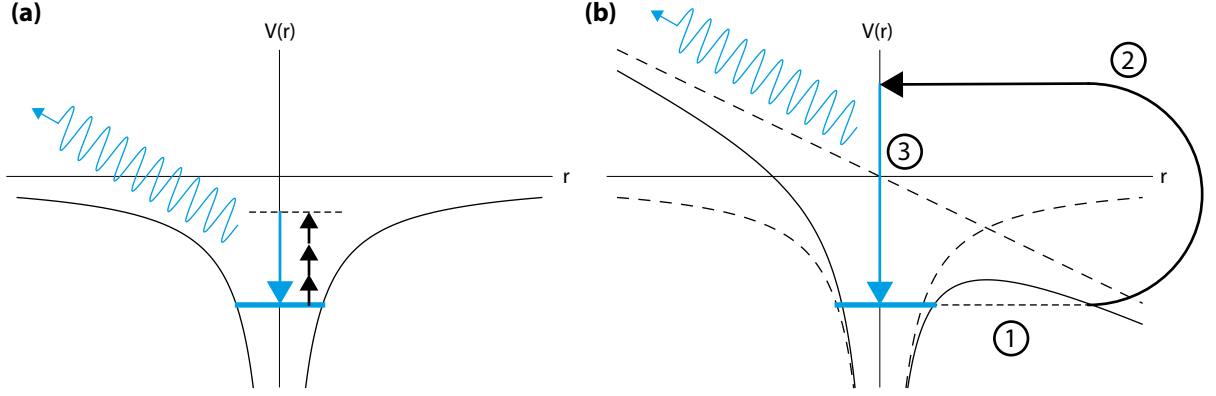


Figure 5.2 Different regimes of HHG. (a) Generation of low-order harmonics by multiphoton absorption in the perturbative regime. (b) Generation of higher-order harmonics in the semi-classical strong field approximation, encompassing the steps: (1) Tunneling ionization, (2) Acceleration in the optical field, (3) Recombination with the nucleus.

5.1.2 Semi-classical strong field approximation

The plateau region in Fig. 5.1 is a clear indication of a non-perturbative behavior (as there is no continued rapid drop-off of conversion efficiency with harmonic order). Also, it is obvious that the perturbative description of Chap. 5.1.1 must break down for energies of the quanta exceeding the ionization energy of the atom. In fact, photoionization is the fundamental process upon which HHG is based. Interestingly, a simple semi-classical three-step-model (Fig. 5.2(b)) put forward in the early 1990s by Krause et al. [51] and Corkum [52], serves to explain (at least qualitatively) most important characteristics and scaling effects of HHG.

The first step is “ionization”: As soon as the optical field becomes comparable to the Coulomb potential, the effective potential becomes significantly distorted, enabling tunneling of a bound electron through the Coulomb energy barrier.

In a second step, the time evolution of the free electron is described by classical oscillations in the field $E = E_0 \sin(\omega t)$, around the position of the nucleus. It is assumed that the electron (of charge e and mass m_e) is “born” in the vacuum with zero initial velocity. Since the influence of the Coulomb force is practically negligible, due to its $1/r^2$ behavior and the short time spent in the vicinity of the nucleus, it is straightforward to integrate the equations of motion

$$\begin{aligned}
 a(t) &= \frac{E_0 e}{m_e} \sin \omega t, \\
 v(t) &= \int_{t_0}^t a(\tau) d\tau = \frac{E_0 e}{m_e \omega} (\cos \omega t_0 - \cos \omega t), \\
 x(t) &= \int_{t_0}^t v(\tau) d\tau = \frac{E_0 e}{m_e \omega^2} (\sin \omega t_0 - \sin \omega t) + (t - t_0) \frac{E_0 e}{m_e \omega} \cos \omega t_0. \quad (5.2a)
 \end{aligned}$$

Upon each return of the electron to the position of its parent nucleus, there is a chance of recombination and subsequent conversion of the combined acquired kinetic energy E_{kin} and ionization potential U_{I} to a high-energy photon

$$\hbar\omega_{\text{rec}} = U_{\text{I}} + E_{\text{kin}}. \quad (5.3)$$

An important precondition for this event is an exactly linear polarization of the driving field - even the slightest ellipticity of the polarization leads to a phase-shifted motion in a transverse plane which makes the electron miss the nucleus, drastically reducing the recombination probability due to reduced wavefunction overlap [39]. The energy spectrum of these emissions will actually be continuous and broadband, since the acquired kinetic energy of Eq. 5.3 depends heavily on the time of tunneling and release of the electron, relative to the phase of the optical field (Fig. 5.3(a)).

However, the recombination events are synchronized by the driving field and occur for both optical half cycles (with inverse field directions). Looking at an ensemble of atoms, this leads to the emission of coherent pulses at twice the frequency of the driving field (2ω) and a carrier envelope shift of π , shown in Fig. 5.3(c). This fact alone already explains the observed discrete odd-harmonic HHG spectrum. Completely analogous to our description of femtosecond lasers in Chap. 2.1.1, the corresponding spectrum is a discrete comb⁴⁸ with a (in this case, very large) line spacing of 2ω and “offset frequency” of ω , as illustrated in Fig. 5.3(d).

The spectral envelope⁴⁹ is determined by the emission spectrum of the recombining electrons (Fig. 5.3(b)). This defines the cut-off energy, marking the abrupt limit for harmonic generation as

$$E_{\text{cut-off}} = U_{\text{I}} + 3.17U_{\text{p}} \quad (5.4)$$

where U_{p} is the so-called *ponderomotive energy*, that is the mean kinetic energy of a charge traveling in an oscillating harmonic field, given by

$$U_{\text{p}} = \frac{e^2 E_0^2}{4m_e \omega^2}. \quad (5.5)$$

The generally low probability of recombination explains the low efficiency of the HHG process. However, the electron which acquires the highest energy of $3.17U_{\text{p}}$ is released at a time $0.3T$ in the optical cycle, when the electric field is still very close to its maximum and the probability of ionization is high (compare Fig. 5.3(a) and (b)). Hence, this comparably efficient harmonic generation at the highest possible energies explains the steepness of the cut-off.

⁴⁸ Only emissions from recombinations yielding energies spaced by $\hbar\omega$ can interfere constructively. The more pulses interfere, the “sharper” or more discrete the emerging spectrum. Therefore the HHG spectrum of isolated femtosecond pulses (featuring only a few pulse cycles) has a much more continuous quality. The same lack of discreteness can be observed at the high-energy end of spectra produced with longer isolated pulses, which is contributed only by emissions during a few optical cycles at the center of the pulse (where it has the highest intensity).

⁴⁹ The range of frequencies available for the interference process.

If we assume a train of mutually coherent pulses (a frequency comb) as the driving field, above reasoning can be applied to each of its constituent frequency components, such that the spectrum of the individual harmonics emerges as a copy of the original comb spectrum, scaled by the harmonic order⁵⁰. This also implies that an initial comb spacing of ω_r will be transformed to $n\omega_r$ for harmonics of order n .

Several other scaling properties can be understood from the semi-classical model. In general, increasing the laser intensity $I = E_0^2$, very rapidly increases the harmonic yield, due to a highly nonlinear dependence of the tunneling probability on I . Increasing I also extends the plateau region and pushes the cut-off energy further into the UV, due to the ponderomotive energy being proportional to I according to Eq. 5.5. Both growth effects are limited by the ionization reaching saturation at an intensity I_{sat} . Once all atoms already get ionized at (or even before) the maximum field amplitude is reached, efficient harmonic generation later in the pulse is prohibited [53–54] which leads to a drastic drop of the conversion efficiency. In addition, the generated plasma negatively affects the phase matching. Alternatively, the cut-off energy can be increased by choosing an atomic species with a larger ionization energy (Eq. 5.4). However there is a tradeoff with the conversion efficiency, since a larger ionization energy is also connected to a lower ionization probability. (Still, these species can have a higher maximum yield, due to an increased saturation intensity I_{sat} , if sufficient laser intensity is available [55].) A similar tradeoff exists for the choice of the driving wavelength. Since the ponderomotive energy scales also with λ^2 , longer wavelengths again extend the cut-off. On the other hand, the harmonic yield is significantly higher for shorter wavelength - a scaling behavior between ω^5 and ω^6 has been predicted based on quantum mechanical numerical simulations [56], in agreement with experiment [57–58]. At least a qualitative understanding of this effect can also be obtained from the semi-classical model: According to Eq. 5.2a the oscillation amplitude of the electron in the optical field scales with λ^2 , such that the electron spends a longer time in the vicinity of the parent atom for shorter-wavelength drivers, which increases the probability of a photon emission per unit time [55].

5.1.3 Phase matching

At the position of each microscopic emitter in the (gas) medium, the harmonic wave (proportional to $\sin(n\omega t + \varphi)$) is generated with the same fixed phase offset⁵¹ φ relative to the driving field (proportional to $\sin\omega t$). This relation (or phase-link) can only be maintained during propagation, if both waves travel at the same speed, that is, if $\frac{\omega}{k(\omega)} = \frac{n\omega}{k(n\omega)}$, or put another way, if the wave vectors fulfill the condition

$$nk(\omega) = k(n\omega).$$

⁵⁰ If plotting the spectrum as a function of wavelength (such as in an image acquired from a grating-based spectrometer), harmonics become increasingly “narrow” and closely spaced for higher order.

⁵¹ This is due to the fact that, under steady state conditions, each individual emitter responds in the exact same deterministic way to the external perturbation.

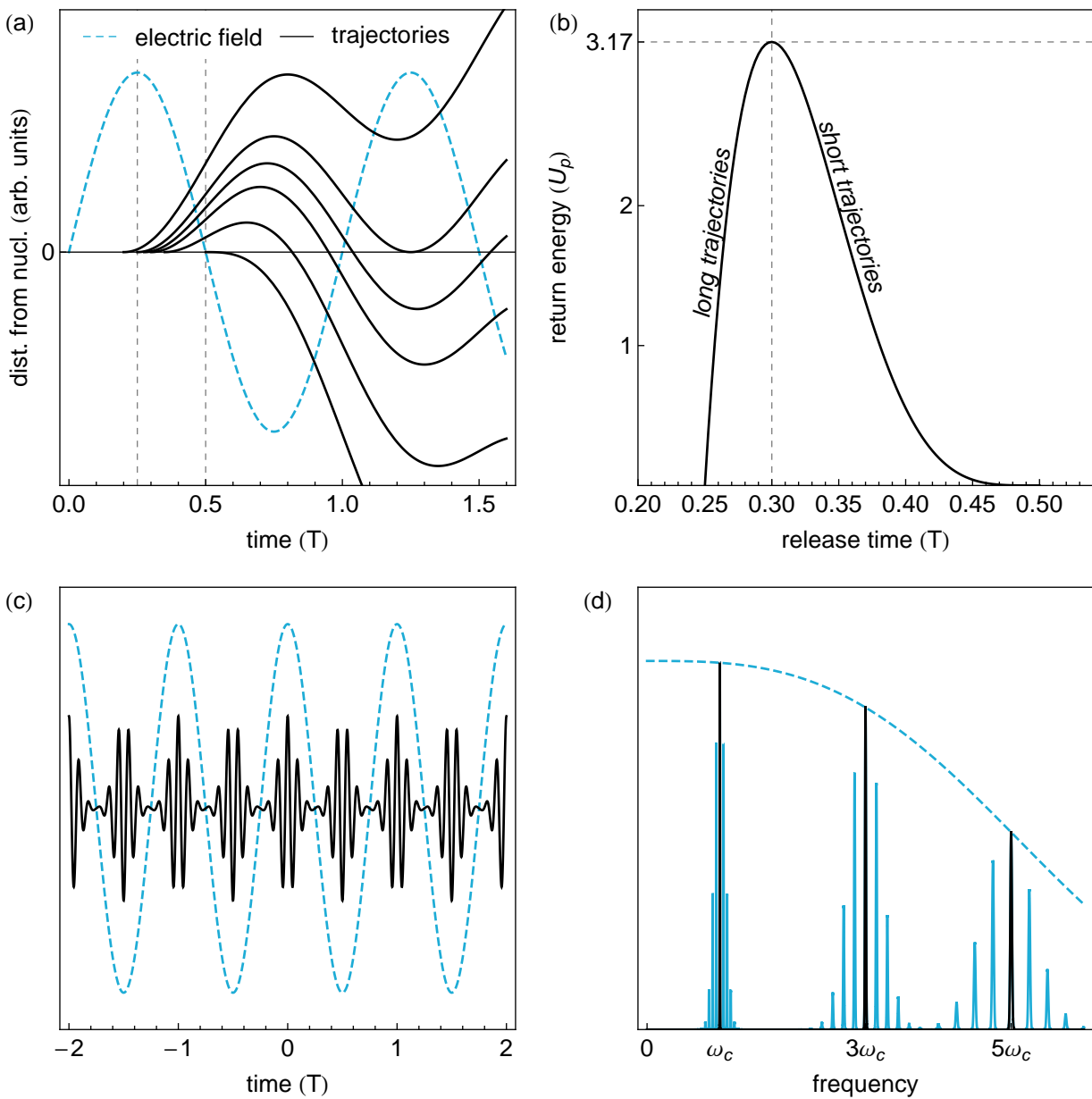


Figure 5.3 (a) Classical trajectories of the free electron according to Eq. 5.2, for different release times (tunneling times) during the optical cycle (period T) of the driving field. The kinetic energy upon recombination is proportional to the steepness of the trajectory at the zero crossing. The highest energy occurs for a release time of roughly $0.3T$. All other energies can be generated via two different (short and long) trajectories. Electrons released between 0 and $1/4T$ are lost, and do not recollide with the nucleus. (b) Return energy depending on the release time. The maximum energy of $3.17 U_p$ occurs at a release time of $0.3T$. (c) The ionization and recombination processes lead to the emission of coherent pulses at twice the frequency of the driving field, with alternating phase according to the instantaneous field gradient. (d) Only odd harmonics of the driving field are generated up to the limit given by the maximum return energy of the electrons. The original structure of a comb with central (or carrier) frequency ω_c is maintained.

Since the individual emitters are positioned randomly in space, this is the precondition

for all generated harmonics to be in phase, leading to a detectable macroscopic effect via constructive interference. In the most general case, at least the effect of normal chromatic dispersion (stating exactly that the phase velocity is not independent of frequency) leads to a deviation from this condition, or phase mismatch

$$\Delta k = k(n\omega) - nk(\omega).$$

Other effects can be used to deliberately balance the chromatic dispersion, to achieve $\Delta k = 0$. In the case of HHG the following main contributions can be considered:

$$\Delta k = \underbrace{\Delta k_{\text{disp}}}_{<0} + \underbrace{\Delta k_{\text{electron}}}_{>0} + \underbrace{\Delta k_{\text{Gouy}}}_{>0}.$$

The first term is caused by normal dispersion in the neutral medium, as already discussed above. The second term is due to the presence of free electrons, generated by ionizing a fraction of the atoms and is the most important contribution to compensate the first term. The third term is caused by the Gouy phase shift at the laser focus (see Eq. 3.14). This makes driving laser wavelength, intensity, gas pressure and focusing geometry the most important directly accessible parameters to influence phase matching.

Although not directly considered a phase matching effect, reabsorption of the generated harmonics in the gas medium has an important influence on the efficiency of the generation process [45].

Up to date, no fully comprehensive theory of all influences exists, to allow straight forward HHG phase matching [47, 56].

5.2 Experimental realization

5.2.1 Gas supply and nozzle design

Xenon was chosen as the gas target for high harmonic generation, because it has the lowest ionization energy of all noble gases (12.13 eV). According to the discussion in Chap. 5.1.2 it therefore provides the highest conversion efficiency, while the reduced high-energy cut-off is of no importance in the context of low-order harmonic generation. The backing pressure of the gas was controlled via a digital valve and pressure gauge (Pfeiffer Vacuum APR 265), digital valve (Pfeiffer Vacuum EVR 116) and controller (Pfeiffer Vacuum RVC 300) operating in a closed loop.

The gas jet is supplied via a nozzle inside the chamber, positioned closely to the primary intracavity focus. Care has been taken to keep the gas tubing between the valve and nozzle short, to avoid excessively long evacuation times and waste of the (expensive) Xenon gas in the dead volume. (Once the vacuum has been broken and the tube filled with air, it can take some time to pump it through the small nozzle opening.) We mostly used circular quartz glass capillaries of varying inner diameter (50 μm , 100 μm and 200 μm), glued to

a gas tubing connector (Fig. 5.6(c)) with two-component epoxy glue, adapted by a short aluminum tube of 1 mm inner diameter.

In an attempt to increase the interaction length with the gas, without increasing the net gas flow, we also tried nozzles with a “slit-like” geometry. These were fabricated from standard medical hollow needles (0.5 mm inner diameter) by squeezing and cutting them with an oblique end wire cutter and finally polishing the end (which has been sealed by the cutting process) with fine Grit-1000 sanding paper, while monitoring the result under a microscope, to produce a slit of constant thickness (around 50 μm) as in Fig. 5.6(d). In the end, the potential theoretical gain in harmonic yield was outweighed by losses due to imperfect alignment of the slit parallel to the beam, with no additional rotational degree of freedom available for online optimization.

To exactly steer the gas jet, the nozzle was mounted on a 3D translation stage, assembled from three vacuum compatible miniature single-axis direct-drive piezo stepper translation stages (Newport Agilis AG-LS25V6) shown in Fig. 5.6(b). Due to backaction of the incremental stepper motion, the cavity was regularly thrown out of lock when optimizing the gas jet position during operation. This problem was solved by mounting the translation stage on a separate small breadboard, mounted directly to the inside of the vacuum chamber wall (Fig. 5.6(a)).

5.2.2 Output couplers

One of the main challenges in cavity-enhanced HHG is efficient outcoupling of the generated harmonic light - especially for low order harmonics. As mentioned in Chap. 5.1 the harmonic light is usually⁵² generated collinearly with the driving laser, requiring a spectrally selective outcoupling mechanism. However, while a high efficiency of this mechanism is desired, it has to equally fulfill the constraint of introducing only negligible attenuation of the driving laser wavelength, otherwise the power enhancement within the resonator would break down.

A few different approaches exist:

- A particularly simple solution is to use p-polarized light inside the cavity and position a glass plate at Brewster angle for the driving wavelength, as a low-loss dichroic intra-cavity beam splitter. The disadvantage of this approach is the typically low reflectance (and thereby outcoupling efficiency) for the generated harmonics, which depends on the (small) change of the refractive index for the driving wavelength and the harmonic wavelength. For low-order harmonics, the outcoupling efficiency is therefore especially bad.

In principle, knowledge of the wavelength-dependent complex refractive index

$$\underline{n}(\omega) = n(\omega) + i\kappa(\omega)$$

⁵² noncollinear hhg...

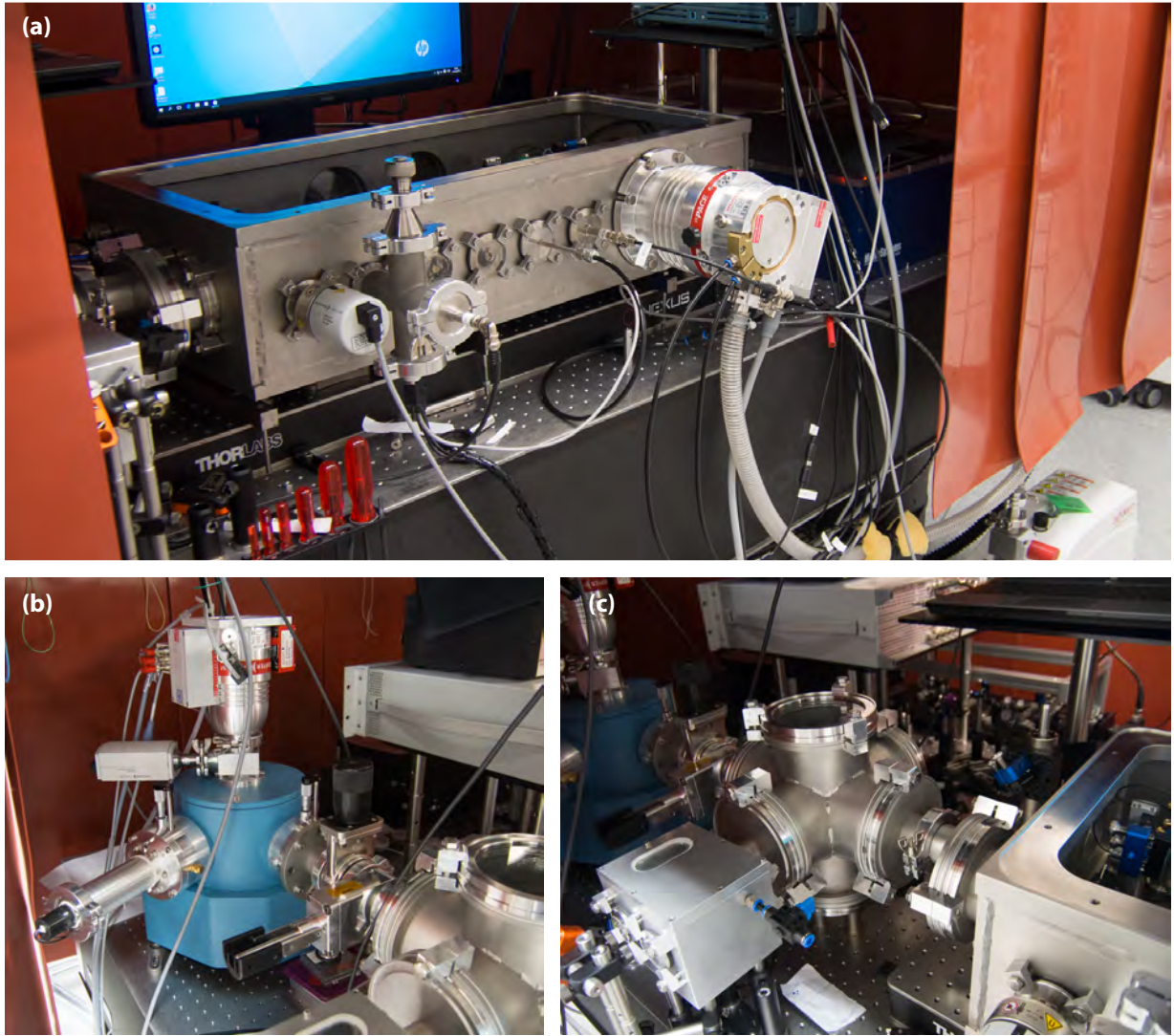


Figure 5.4 Overview of vacuum chamber and UV diagnostics. (a) Main chamber. (b) UV spectrometer with PMT (left) mounted. (c) Additional intermediate vacuum chamber with flip mirror to relay intracavity beam to other output ports.

of a beam splitter material, allows calculation of the reflected intensity R of s- and p-polarized components, incident under an angle α via the Fresnel equations:

$$R_s = \left| -\frac{\sin(\alpha - \alpha')}{\sin(\alpha + \alpha')} \right|^2 \quad (5.6a)$$

$$R_p = \left| \frac{\tan(\alpha - \alpha')}{\tan(\alpha + \alpha')} \right|^2 \quad (5.6b)$$

$$n \sin \alpha = n' \sin \alpha' \quad (5.6c)$$

where n' is associated with the optical component and $n = 1$ in vacuum. The Brewster angle α_B indicating zero reflection of p-polarized light, is given by

$$\alpha_B = \arctan\left(\frac{n'}{n}\right).$$

Angles α and α' can in general emerge as complex quantities (with non-vanishing imaginary part even for real refractive indices, if $n' < n$) from Eq. 5.6c (in which case the Brewster angle loses its meaning).

A typical material choice for such a beam splitter is sapphire, which allows a reflectance of up to 0.17 for harmonics at 50 nm [59].

- In principle, it is possible to enhance the reflectance of the brewster plate at the target wavelength by adding an appropriate dielectric coating, however, it is technically challenging to do this without introducing significant loss at the fundamental wavelength, and to make these coatings withstand the high intracavity power levels. Reference [60] reports the use of a fluoride-multilayer-coated fused silica plate, designed for a reflectance above 90% for p-polarized light at 159 nm, having an absorption loss at the fundamental wavelength of around 0.1 % and showing rapid degradation during operation.
- Specially engineered diffraction gratings can be used as an optical element inside the cavity which acts as a near-perfect high reflector for the fundamental light while diffracting harmonic orders [61–62].
- The increasing angular confinement of the HHG beam with harmonic order, opens up the possibility to extract the harmonic light geometrically via a small hole in one of the focusing mirrors, without introducing excessive loss for the much larger fundamental cavity mode [63–64]. This method is obviously not suited for low-order harmonics.
- Non-collinear HHG via two pulses incident on the gas target at an angle might be yet another viable alternative [65–66].

We made an attempt to use thin nitrocellulose membranes (used to fabricate common pellicle beam splitters) at Brewster angle as an outcoupling element. This would have the advantage of only introducing minor amounts of GDD due to typical membrane thicknesses of only a few micrometers. Since such polymers are also typically strong absorbers in the UV, a correspondingly high reflectance⁵³ is to be expected according to Eq. 5.6. However, not much data is available on the optical characteristics of nitrocellulose in the UV. Reference [67] gives a value of 10^5 cm^{-1} for the absorption coefficient μ at 160 nm, which relates to an extinction coefficient κ of 0.127 via

⁵³ According to the Fresnel equations, a good (ideal) absorber is also a good (ideal) reflector. Metals have the largest extinction coefficients and are therefore the best reflectors. It is interesting to note, that a “true” absorber (in the sense of featuring a low surface reflectance) actually needs a moderate κ and a porous surface to cause absorption via multiple bounces - an effect not covered by the macroscopic application of the Fresnel equations to a plane optical interface between homogeneous media.

$$\kappa = \frac{\lambda\mu}{4\pi}.$$

The real part of the refractive index can be estimated via the Kramers-Kronig relations to be in the range of 1.9 – 2.2, yielding a reflectance on the order of a percent - much better than equivalent values for optical glasses (compared in table 5.1).

	sapphire	fused silica	nitrocellulose
Brewster angle @ 800 nm	60.40°	56.50	56.31
n @ 800 nm	1.76	1.45	1.5
κ @ 800 nm	0	0	0
n @ 267 nm	1.83	1.55	
κ @ 267 nm	0	$2.8 \cdot 10^{-6}$	
n @ 160 nm	2.03	1.65	2
κ @ 160 nm	0.024	$2 \cdot 10^{-6}$	0.13
Reflectance for p-polarization @ 267 nm	0.018 %	0.006 %	
Reflectance for p-polarization @ 160 nm	0.268 %	0.073 %	1.051 %
Data source (UV)	[68–69]	[70]	[67]

Table 5.1 Comparison of complex refractive indices and calculated reflectances for different outcoupler materials.

One has to bear in mind, that membranes can act as a Fabry-Perot etalon even for large incidence angles like the Brewster angle (since, owing to their small thickness, multiple reflections from both boundaries still overlap). Therefore, the thickness of the membrane has to be appropriately chosen (to have a resonance peak at the driving wavelength), to avoid the amplification of losses via destructive multi-beam interference, even for tiny deviations of the alignment from Brewster angle. The problem with this approach was, that the membranes did not sustain the high power levels in the resonator, leading to a decrease of the power enhancement by a factor of 10 within seconds, due to damage evidenced by Fig. 5.5. The damage could not be attributed to generated UV light, but occurred already with no gas medium for high harmonic generation present.



Figure 5.5 Damaged spots on pellicle outcouplers.

For this reason, we turned to using a 100 μm thick BK7 silicate glass plate (easily available as cover glass plates for microscopy). We did not employ sapphire plates (factor of 3-4

improvement in reflectance at our target wavelength of 160 nm), since none was available at a comparable thickness. (Polishing of the brittle material seems to be tricky.)

5.2.3 XUV detection

To characterize the generated high harmonic radiation, a VUV grating spectrometer (McPherson Model 234) was available, with a detector choice of a high-sensitivity CCD camera (Andor DO940P-BN-995) or a photomultiplier tube (Hamamatsu R6836). The spectrometer was pumped independently from the main chamber with a small turbo pump and could be disconnected by a manual vacuum shutter, such that vacuum in the spectrometer could be maintained while breaking the vacuum in the main chamber.

One of the challenges in the detection of the very faint HHG signal was to separate it from the unwanted small fraction of light at the fundamental wavelength which is unavoidably coupled out as well. As a consequence, the useful signal can be masked by light at the fundamental wavelength, scattered inside the spectrometer, since this residual contribution often has a larger intensity.

The selected photomultiplier tube (PMT) offers an easy solution, being “solar blind” outside a sensitivity region limited to the range of 115 nm to 320 nm. Using the PMT, spectra could only be acquired by mechanically scanning the spectrometer grating, however this detector type has the advantage of a “real time” output signal (compared to single image acquisition and readout times of the CCD on the order of a few seconds, at least) which is a clear advantage when monitoring the HHG signal at a particular harmonic wavelength during alignment of the cavity.

On the other hand, the CCD allowed assessment of the harmonic beam profiles and recording of more reliable spectra, since fluctuations in the cavity operation during the acquisition time do not distort the relative spectral intensities. Here, suppression of the fundamental wavelength was more involved. Scattering inside the spectrometer occurred at the entry slit, at the grating itself, and of course at the positions where the first-order diffraction beam and the zero order diffraction beam hit the spectrometer chamber walls (or sensor). Use of a more highly dispersing grating with smaller groove spacing can be helpful to suppress the last two contributions by increasing the geometrical distance between diffracted beams at different wavelengths, with the tradeoff of lower radiant power per surface area on the detector surface. Partly, scattered light could be suppressed by lining the spectrometer chamber with more highly absorptive material (e.g. vacuum compatible matte black aluminum foil). Filters (transmissive or reflective) with high suppression ratio are not available for the UV region. The best we could obtain (Pelham Research 160-BB-1D) featured 34% transmission at 160 nm (fifth harmonic), 4% transmission at 267 nm (third harmonic) and 1% transmission at 800 nm (fundamental).

To focus the outcoupled harmonic light on the spectrometer entry slit, a UV-transparent magnesium fluoride or calcium fluoride lens was used. (The same material was used for the chamber windows.) The choice of a UV mirror (alignment also remote controlled) for beam steering onto the spectrometer, initially proved to be a pitfall. As we found out, the

operational range of the initially chosen MgF₂-coated aluminum mirror (Thorlabs PF10-03-F01) did not extend to short wavelengths beyond 200 nm. A similar specialty mirror (Acton Optics H1200-1D-MB) was finally used successfully.

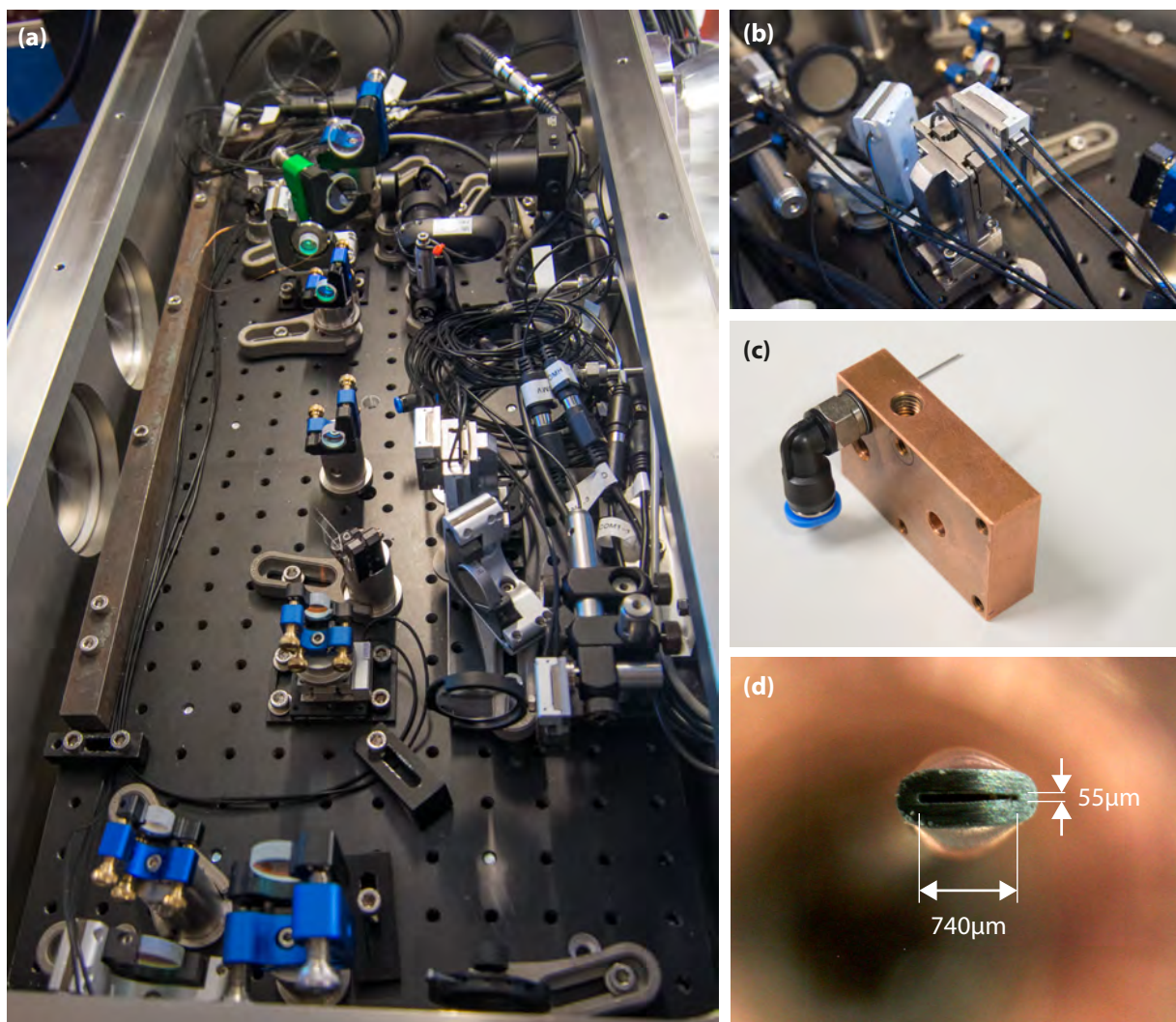


Figure 5.6 (a) View inside the main HHG chamber. (b) 3D translation stage to position gas jet. (c) Gas nozzle mount. (d) Alternative slit-nozzle.

5.2.4 HHG results

Third and fifth harmonic signals were successfully generated (Fig. 5.7(b)). The best result (data summarized in table 5.2) was obtained with a gas nozzle with inner diameter of $100\ \mu\text{m}$ and maximum possible backing pressure of two bar. The yield was optimized mainly through alignment of the nozzle position in three degrees of freedom and adjustment of the CEO frequency of the comb. Further increase of the backing pressure was not possible, due to the the gas load limit of the turbo pump being reached. Harmonics of higher order could not be detected within the sensitivity of our detection scheme.

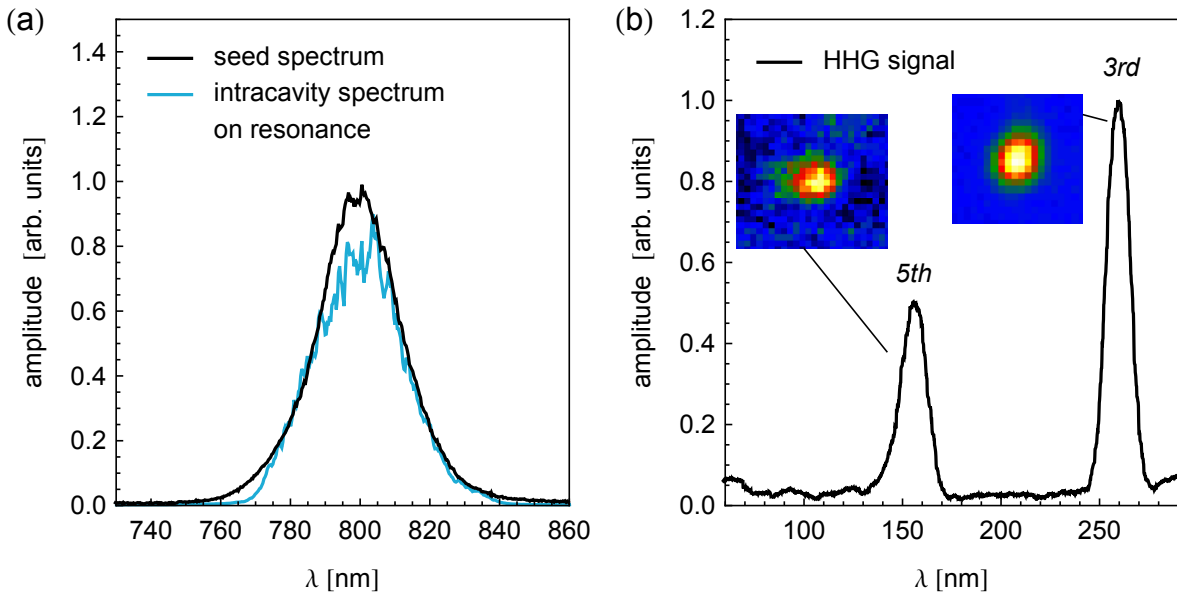


Figure 5.7 Spectrum of the (a) fundamental mode and (b) harmonic output measured via the PMT. Amplitudes of outcoupled harmonics are not to scale for the latter, due to different filtering and detection efficiencies of the spectrometer. The inset beam profile of the 3rd and 5th harmonic were recorded on the Andor CCD and exhibit a nicely Gaussian shape.

harmonic order	3 rd	5 th
wavelength	267 nm	160 nm
PMT signal (U)	11 V	230 mV
PMT photocatode radiant sensitivity	23 mA/W	11 mA/W
PMT high voltage	1250 V	1250 V
PMT gain (G)	$2 \cdot 10^6$	$2 \cdot 10^6$
PMT measurement load resistance (R)	1 M Ω	1 M Ω
Outcoupler efficiency	0.000063	0.00073
UV mirror efficiency	0.89	0.84
Grating efficiency	0.2	0.3
detected power (I_{det})	$2 \cdot 10^{-10}$ W	$1 \cdot 10^{-11}$ W
generated power (I_{gen})	20 μ W	60 nW
conversion efficiency ⁵⁴	$2 \cdot 10^{-5}$	$6 \cdot 10^{-8}$

Table 5.2 HHG results. The detected power is derived according to $I_{\text{det}} = U/(S \cdot G \cdot R)$. The PMT voltage U was measured with a large enough spectrometer exit slit width to record a significant part of the spectrum of each harmonic. The entrance slit width was chosen large enough to avoid clipping.

⁵⁴ Given with respect to extracavity power of 900 mW

We obtain a peak power density at the primary focus of $PD_p = 5 \cdot 10^{13} \text{ W/cm}^2$ according to

$$PD_p = 0.94 I \frac{1\text{s}}{f_{\text{rep}} \tau_{\text{pulse}}} \frac{2}{\pi w^2},$$

based on all relevant parameters: Average intracavity power $I = 0.9W \cdot 250$, comb repetition rate $f_{\text{rep}} = 108 \text{ MHz}$, FWHM pulse duration $\tau_{\text{pulse}} = 26 \text{ fs}$ and $1/e^2$ beam radius $w = 10 \mu\text{m}$ at the primary cavity focus.

6 Conclusions and Outlook

We realized a Ti:Sapphire laser seeded femtosecond enhancement cavity with about 25 fs intracavity pulse duration and an overall enhancement factor of 250. We demonstrated tunability of the beam waist in the intracavity focus between $10\ \mu\text{m}$ and $22\ \mu\text{m}$ while preserving the high enhancement factor of the cavity. The fifth harmonic at 160 nm was generated in the intracavity focus in Xe gas. Realization of such a VUV comb is an essential step e.g. for the precise measurement of optical transition of the ^{229}Th nucleus or for the realization of an $^{115}\text{In}^+$ optical clock [60].

Due to the ionization probability of Xe being extremely sensitive to the intensity at a range of several $10^{13}\ \text{W}/\text{cm}^2$ [71], an increase in intensity by a small factor already holds promise to further improve the high harmonic generation efficiency by several orders of magnitude. However, due to the dense line spectrum of frequency combs, each individual line will always have a power that is just a tiny fraction of the total harmonic output power, probably requiring a tunable CW laser as an intermediate step for interrogating the isomer transition.

We have developed a generally applicable scheme to compensate beam profile ellipticity in femtosecond enhancement cavities in standard bow-tie configuration, by moving to a non-planar layout that still conserves the linear polarization throughout the entire cavity. Our solution introduces manageable additional complexity with respect to setup and operation, and can be built from the same readily available off-the-shelf components used in the planar setup. The freedom to tune the intracavity focus spot size over a wider range and to reduce the pulse energy density on the cavity mirrors, is beneficial in non-linear conversion applications with both low- and high-power seed laser source.

Calcium fluoride crystals doped with high concentrations of ^{229}Th have already been successfully grown by our group. Recent findings of collaborators at the MPQ Munich have provided direct proof for the existence of the thorium isomer state [14]. For direct probing of the isomer transition, there is the prospect of tunable CW lasers becoming available in the VUV, based on the nonlinear crystal potassium beryllium fluoroborate (KBBF) [18]. All in all, based on this growing toolset, there are justified hopes to realize the envisioned solid state nuclear frequency standard in the foreseeable future.

A Driver electronics for shear piezoelectric motors

In shear piezoelectric motors, the movable component or load (bed of a linear stage, or mirror holder of a mirror mount) is directly pressed against a shear piezo by a spring. When a sawtooth voltage signal is applied to the piezo, the slow voltage ramp leads to a slow piezo movement, dragging along the load in the process. Upon the voltage reset during the steep edge of the signal, the piezo moves back to its initial position so quickly, that it slips on the contact surface to the load without moving it. The net effect is an incremental directed motion of the load with principally unlimited range. The direction can be changed by applying a “reverse sawtooth” signal.

Immediately obvious from its design, a piezo stack behaves electrically as a capacitor, which means that a comparably large transient current is needed to quickly switch the applied voltage. A direct connection to a digital analog converter output is therefore not possible, and even an added operational amplifier (op-amp) based amplifier circuit usually does not provide sufficiently fast response times. A simple solution is to use a MOSFET bridge, as a high-current switch between ground and a slow voltage ramp provided by an op-amp, similar to the solution described in [72]. The op-amp output needs to be supported by a large enough capacitor, to avoid a voltage drop when the switching occurs. Since the capacitor also limits the slew rate of the voltage ramp, a compromise for the capacitance value has to be found.

Figures A.1 and A.2 illustrate the circuit design and printed circuit board layout (PCB) of a driver designed for compatibility with actuators from the Newport Agilis series, used in the experiment.

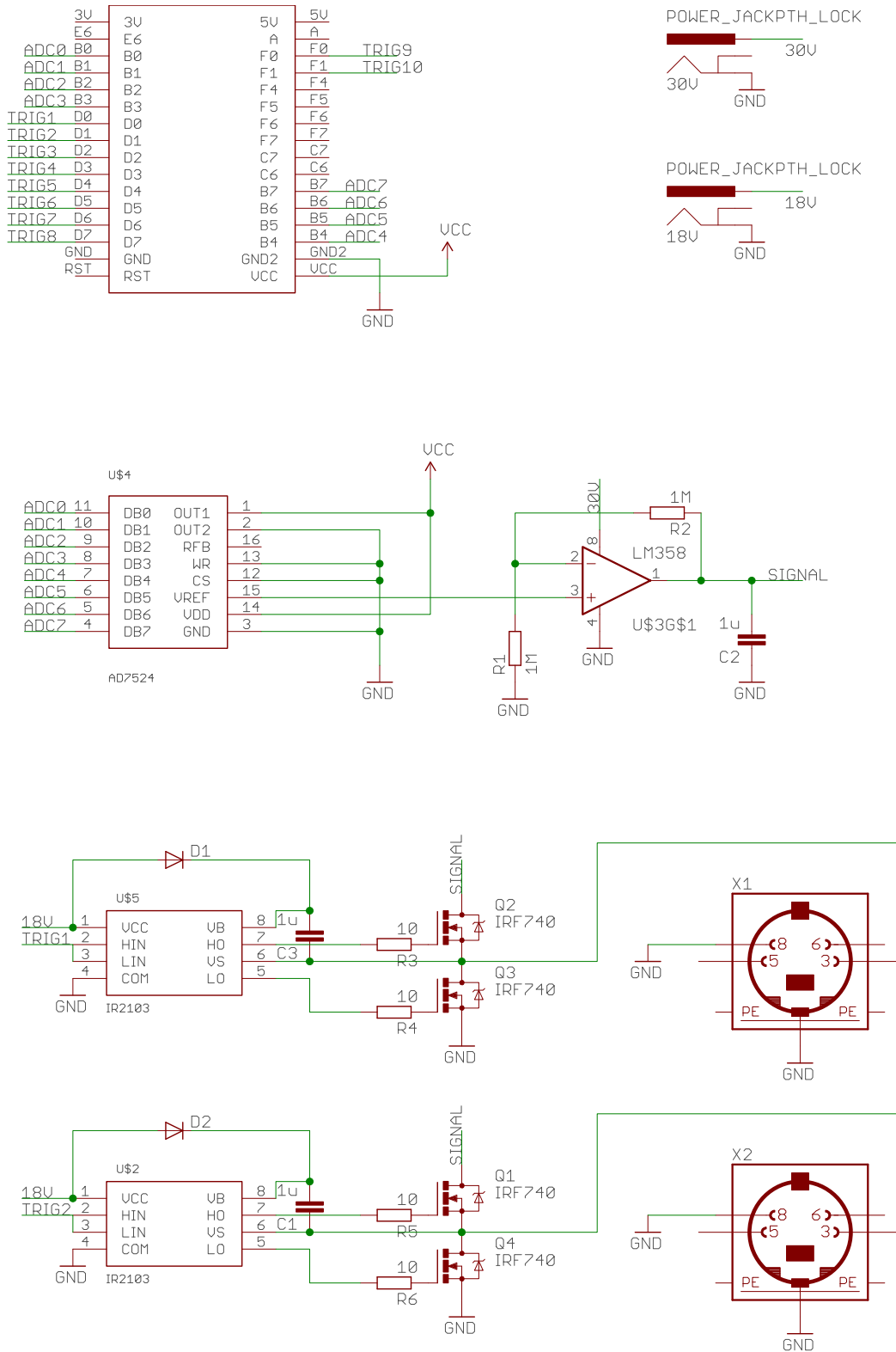


Figure A.1 PCB schematic. Top left to bottom: Microcontroller with USB interface controlling the voltage ramps and MOSFET triggers. Power supply. Digital analog converter (DAC) and op-amp amplifier circuit providing a maximum voltage of 18 V, shared between all output ports. One MOSFET bridge (including MOSFET driver IC) is added for each output port. (Multiplexing using an analog multiplexer IC is not possible, since it also does not support the high transient currents.)

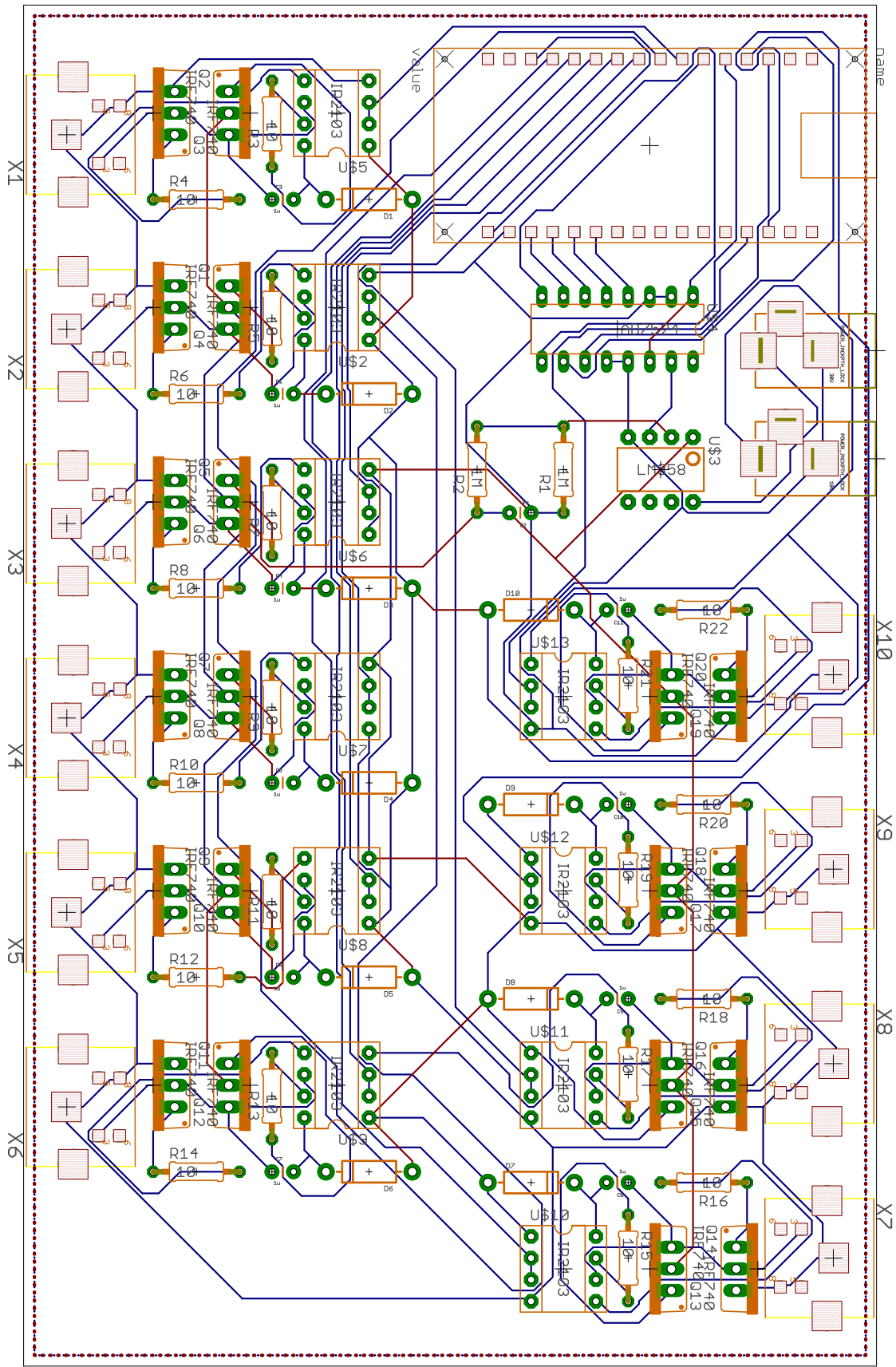


Figure A.2 PCB layout. Output ports for up to ten piezos.

Acknowledgements

First of all, I would like to thank my supervisor Prof. Thorsten Schumm, for giving me the opportunity to collaborate on an exciting and very interdisciplinary new research project, from the very beginning. Starting with literally assembling the first screws in an empty lab, the work towards an ambitious goal (partially outside of our established fields of expertise) was a challenge at times, but an equally great adventure, thanks to his dedication and clear vision of our project. On top of exceptional scientific insight and experience, he always put a very humane meaning to the german term “Doktorvater”, with a refreshing energy and sometimes unconventional but always caring nature.

I’m lucky for having been able to work with a team that, although small, provided a great mix of knowledge, shared motivation and humor. Matthias Schreitl was my “lab and office buddy” from day one, always available for support and insightful discussion - both scientific and unscientific. Our mutual outdoorsy and guitar-related adventures outside the lab are also greatly remembered. I’m thankful to Georgy Kazakov for being my go-to person for all types of questions about the gory details of nuclear-physical model calculations. Simon Stellmer proved to be a great source of knowledge and guidance for a really very broad range of topics in day-to-day experimental work. I’m particularly indebted to Jozsef and Enikoe Seres, who brought their expertise in high harmonic generation to our group. Over the years, joining forces with a number of bright and motivated bachelor and master students was also a very rewarding experience, not least in honing my own skills as a supervisor or my physical understanding (upon the attempt to explain some facts which were previously believed to be understood). In particular, I thank Jakob Fellingner, who stayed with us the longest, and was a great help in our last attempts in scaling up the yield of the HHG process.

I feel, that I owe a lot to our “extended family”, involving the groups of Prof. Jörg Schmiedmayer and Prof. Arno Rauschenbeutel, with respect to the greatly enjoyable and stimulating international work atmosphere at the *Atominstitut*. Fostered by the somewhat remoteness of the location (in the beautiful nature surroundings of the *Wiener Prater*), and the important institutions of a shared kitchen, coffee corner and outdoor patio, a lot of fruitful scientific exchange as well as friendships could develop. I am already missing the shared meals and early morning summer sessions of soccer and volleyball, among many other things.

I also would like to thank...

...Collaborators at the MPQ Munich, and in particular Marc Fischer from Menlo Systems, for helpful discussion and continued support on frequency comb issues.

...the doctoral program *Complex Quantum Systems* (CoQuS), which provided a plethora of added benefits, including lecture series, summer schools, retreats and visits at other research institutions. I’m especially happy about the chance for an extended research visit at the fascinating group of Prof. Jun Ye in Boulder, Colorado, where I had the pleasure

to collaborate with Oliver Heckl on mid-IR optical parametric amplifiers and frequency comb spectroscopy.

...the tax payers and general public for getting the chance to learn what I learned during more than a decade of university studies and work - honestly.

...my exceptional highschool teachers (finally), who implanted the spirit very early, that it's cool and rewarding to learn new things and explore.

Last but not least, I am greatly thankful for...

...my most loving parents, who supported me in each and every possible way, literally from day one - I surely do not take it for granted.

...Anita - my greatest discovery, and partner of many years - for continued support, patience and friendship.

...all my friends and extended family (even those who don't share excitement about atomic clocks), for being great company and consistently refining "some free time" to many pleasant memories.

Since compiling an inclusive list will always remain a futile attempt, I stop here⁵⁵, apologize, and say "thank you" to all of you I have not explicitly mentioned - you know who you are.

⁵⁵ Before this gets awkward. However, not before finally and officially confessing my love of footnotes ;)

List of Publications

Publications to which the author has contributed (also documenting some of his work conducted within the broader scope of the “thorium-229 project” - not directly related to laser spectroscopy):

- G. Winkler, J. Fellingner, J. Seres, E. Seres, and T. Schumm
“Non-planar femtosecond enhancement cavity for VUV frequency comb applications”
Opt. Express 24, 1206–1208 (2016).
- J. Seres, E. Seres, B. Landgraf, B. Ecker, B. Aurand, a Hoffmann, G. Winkler, S. Namba, T. Kuehl, and C. Spielmann
“Parametric amplification of attosecond pulse trains at 11 nm”
Sci. Rep. 4, 4254 (2014).
- P. Dessoovic, P. Mohn, R. a Jackson, G. Winkler, M. Schreitl, G. Kazakov, and T. Schumm
“²²⁹Thorium-doped calcium fluoride for nuclear laser spectroscopy”
J. Phys. Condens. Matter 26, 105402 (2014).
- G. a. Kazakov, a. N. Litvinov, V. I. Romanenko, L. P. Yatsenko, a. V. Romanenko, M. Schreitl, G. Winkler, and T. Schumm
“Performance of a ²²⁹ Thorium solid-state nuclear clock”
New J. Phys. 14, 083019 (2012).
- G. Kazakov, M. Schreitl, G. Winkler, J. Sterba, G. Steinhauser, and T. Schumm
“Atomic clock with a nuclear transition: solid state approach at TU Wien”
Arxiv Prepr. arXiv1110.0741 1–10 (2011).

References

- 1 Beck, B., Becker, J., Beiersdorfer, P., Brown, G. and Moody, K. et al. (2007). Energy Splitting of the Ground-State Doublet in the Nucleus Th229. *Physical Review Letters*, *98*(14), 142501.
- 2 Beck, B. R., Moody, K. J., Wilhelmy, J. B., Porter, F. S. and Kelley, R. L. (2009). Improved Value for the Energy Splitting of the Ground-State Doublet in the Nucleus. In *12th International Conference on Nuclear Reaction Mechanisms*.
- 3 Peik, E. and Okhapkin, M. (2015). Nuclear clocks based on resonant excitation of gamma-transitions. *Comptes Rendus Physique*, *16*(5), 516–523.
- 4 Kazakov, G. a., Litvinov, a. N., Romanenko, V. I., Yatsenko, L. P. and Romanenko, a. V. et al. (2012). Performance of a 229 Thorium solid-state nuclear clock. *New Journal of Physics*, *14*(8), 083019.
- 5 Cingöz, A., Yost, D. C., Allison, T. K., Ruehl, A. and Fermann, M. E. et al. (2012). Direct frequency comb spectroscopy in the extreme ultraviolet.. *Nature*, *482*(7383), 68–71.
- 6 Hänsch, T. W. (2006). Nobel Lecture: Passion for precision. *Reviews of Modern Physics*, *78*(4), 1297–1309.
- 7 Ludlow, A. D., Boyd, M. M. and Ye, J. (2015). Optical atomic clocks. , *87*(June), 637–701.
- 8 Itano, W. M., Bergquist, J. C., Bollinger, J. J., Gilligan, J. M. and Heinzen, D. J. et al. (1993). Quantum projection noise: Population fluctuations in two-level systems. *Physical Review A*, *47*(5), 3554–3570.
- 9 Hollberg, L., Diddams, S., Bartels, a., Fortier, T. and Kim, K. (2005). The measurement of optical frequencies. *Metrologia*, *42*, S105–S124.
- 10 Ruchowska, E., Plociennik, W. A., Zylicz, J., Mach, H. and Kvasil, J. et al. (2006). Nuclear structure of Th229. *Physical Review C - Nuclear Physics*, *73*(4), 1–17.
- 11 Dykhne, A. M. (1998). Matrix element of the anomalously low-energy (3.5 +- 0.5 eV) transition in 229Th and the isomer lifetime. *Jetp Letters*, *67*(4), 251–256.
- 12 Kroger, L. A. and Reich, C. W. (1976). Features of the low-energy level scheme of 229Th as observed in the alpha-decay of 233U. *Nuclear Physics, Section A*, *259*(1), 29–60.
- 13 Helmer, R. G. and Reich, C. W. (1994). An excited state of 229-Th at 3.5 eV. *Phys. Rev. C*, *49*(4), 1845–1858.
- 14 von der Wense, L., Seiferle, B., Laatiaoui, M., Neumayr, J. B. and Maier, H.-J. et al. (2016). Direct detection of the 229Th nuclear clock transition. *Nature*, *533*(7601), 47–51.
- 15 Herrera-Sancho, O. A., Nemitz, N., Okhapkin, M. V. and Peik, E. (2013). Energy levels of Th+ between 7.3 and 8.3 eV. *Physical Review A - Atomic, Molecular, and Optical Physics*, *88*(1), 1–7.
- 16 Kazakov, G., Schreitl, M., Winkler, G., Sterba, J. and Steinhauser, G. et al. (2011). Atomic clock with a nuclear transition: solid state approach at TU Wien. *Arxiv preprint arXiv:1110.0741*, pp. 1–10.

- 17 Dessoovic, P., Mohn, P., Jackson, R. a., Winkler, G. and Schreitl, M. et al. (2014). 229Thorium-doped calcium fluoride for nuclear laser spectroscopy.. *Journal of physics. Condensed matter : an Institute of Physics journal*, *26*(10), 105402.
- 18 Chen, C., Xu, Z., Deng, D., Zhang, J. and Wong, G. K. L. et al. (1995). The vacuum ultraviolet phase-matching characteristics of nonlinear optical KBe₂BO₃F₂ crystal. *Applied Physics Letters*, *2930*, 2930.
- 19 Flambaum, V. V. (2006). Enhanced Effect of Temporal Variation of the Fine Structure Constant and the Strong Interaction in 229 Th. , *092502*(September), 1–3.
- 20 Udem, T., Holzwarth, R. and Hänsch, T. W. (2002). Optical frequency metrology.. *Nature*, *416*(6877), 233–7.
- 21 Cundiff, S. T. and Ye, J. (2003). Colloquium: Femtosecond optical frequency combs. *Reviews of Modern Physics*, *75*(1), 325–342.
- 22 Diddams, S. A. (2010). The evolving optical frequency comb [Invited]. *Journal of the Optical Society of America B*, *27*(11), B51.
- 23 Träger, F. (2007). Springer Handbook of Lasers and Optics. *Springer Handbook of Lasers and Optics*, *72*, 1332.
- 24 Ell, R., Morgner, U., Kärtner, F. X., Fujimoto, J. G. and Ippen, E. P. et al. (2001). Generation of 5-fs pulses and octave-spanning spectra directly from a Ti:sapphire laser. *Optics Letters*, *26*(6), 373.
- 25 Ranka, J. K., Windeler, R. S. and Stentz, A. J. (2000). Visible continuum generation in air–silica microstructure optical fibers with anomalous dispersion at 800 nm. *Optics Letters*, *25*(1), 25.
- 26 Iaconis, C. and Walmsley, I. a. (1998). Spectral phase interferometry for direct electric-field reconstruction of ultrashort optical pulses.. *Optics letters*, *23*(10), 792–4.
- 27 Liu, W. and Zhou, C. (2005). Femtosecond laser speckles.. *Applied optics*, *44*(30), 6506–6510.
- 28 Gohle, C., Udem, T., Herrmann, M., Rauschenberger, J. and Holzwarth, R. et al. (2005). A frequency comb in the extreme ultraviolet. *Nature*, *436*(7048), 234–237.
- 29 Jones, R. J., Moll, K. D., Thorpe, M. J. and Ye, J. (2005). Phase-Coherent Frequency Combs in the Vacuum Ultraviolet via High-Harmonic Generation inside a Femtosecond Enhancement Cavity. *Physical Review Letters*, *94*(19), 193201.
- 30 Svelto, O. (1998). *Principles of Lasers*. 4th edition.
- 31 Kogelnik, H. and Li, T. (1966). Laser beams and resonators.. *Applied optics*, *5*(10), 1550–1567.
- 32 Gouy, L. G. (1890). Sur une propriété nouvelle des ondes lumineuses. *C. R. Acad. Sci. Paris*, *110*, 1251–1253.
- 33 Siegman, A. E. and Valley, M. (1986). *Lasers*. University Science Books.
- 34 Dupraz, K., Cassou, K., Martens, a. and Zomer, F. (2015). The ABCD matrix for parabolic reflectors and its application to astigmatism free four-mirror cavities. *Optics Communications*, *353*, 178–183.
- 35 Zomer, F., Fedala, Y., Pavloff, N., Soskov, V. and Variola, A. (2009). Polarization induced instabilities in external four-mirror Fabry-Perot cavities. *Appl. Opt.*, *48*(35), 6651–6661.

- 36 Carstens, H., Holzberger, S., Kaster, J., Weitenberg, J. and Pervak, V. et al. (2013). Large-mode enhancement cavities. *Optics Express*, *21*(9), 11606–11617.
- 37 Bonis, J., Chiche, R., Cizeron, R., Cohen, M. and Cormier, E. et al. (2012). Non-planar four-mirror optical cavity for high intensity gamma ray flux production by pulsed laser beam Compton scattering off GeV-electrons. *Journal of Instrumentation*, *7*, P01017–P01017.
- 38 Yefet, S. S., Jouravsky, V., Pe'er, A. and Pe'er, A. (2013). Kerr-lens Mode Locking Without Nonlinear Astigmatism. *Journal of the Optical Society of America B*, *30*(3), 549–551.
- 39 Möller, M., Cheng, Y., Khan, S. D., Zhao, B. and Zhao, K. et al. (2012). Dependence of high-order-harmonic-generation yield on driving-laser ellipticity. *Physical Review A - Atomic, Molecular, and Optical Physics*, *86*(1), 1–5.
- 40 Chang, Z. (2004). Single attosecond pulse and xuv supercontinuum in the high-order harmonic plateau. *Physical Review A*, *70*(4), 043802.
- 41 Nilsson, a. A. C., Byer, R. L. R. L. and Gustafson, E. (1989). Eigenpolarization theory of monolithic nonplanar ring oscillators. *IEEE Journal of Quantum Electronics*, *25*(4), 767–790.
- 42 Yelland, C., Hong, J., Padgett, M. J., Dunn, M. H. and Sibbett, W. (1994). A vector approach to the geometrical dependence of polarisation rotation in a non-planar cw Nd:YAG ring laser. *Optics Communications*, *109*(5-6), 451–456.
- 43 Hansch, T. W. and Couillaud, B. (1980). Laser frequency stabilization by polarization spectroscopy of a reference cavity. *Optics Communications*, *35*(3), 441–444.
- 44 Moore, J., Davis, C., Coplan, M. and Greer, S. (2009). *Building Scientific Apparatus (4th Edition)*.
- 45 Constant, E., Garzella, D., Breger, P., Mével, E. and Dorrer, C. et al. (1999). Optimizing High Harmonic Generation in Absorbing Gases: Model and Experiment. *Physical Review Letters*, *82*(8), 1668–1671.
- 46 Takahashi, E., Nabekawa, Y. and Midorikawa, K. (2002). Generation of 10- microJ coherent extreme-ultraviolet light by use of high-order harmonics.. *Optics letters*, *27*(21), 1920–1922.
- 47 Popmintchev, T., Chen, M.-C., Bahabad, A., Gerrity, M. and Sidorenko, P. et al. (2009). Phase matching of high harmonic generation in the soft and hard X-ray regions of the spectrum.. *P N A S*, *106*(26), 10516–21.
- 48 Lee, J., Carlson, D. R. and Jones, R. J. (2011). Optimizing intracavity high harmonic generation for XUV fs frequency combs. *Optics Express*, *19*(23), 23315.
- 49 Chang, Z., Rundquist, A., Wang, H., Murnane, M. and Kapteyn, H. (1997). Generation of Coherent Soft X Rays at 2.7 nm Using High Harmonics. *Physical Review Letters*, *79*(16), 2967–2970.
- 50 Boyd, R. W. (2008). Nonlinear Optics. *Book*, pp. 613.
- 51 Krause, J. L., Schafer, K. J. and Kulander, K. C. (1992). High-order harmonic-generation from atoms and ions in the high-intensity regime. *Phys. Rev. Lett.*, *68*(24), 3535–3538.
- 52 Corkum, P. B. (1993). Plasma Perspective on Strong-Field Multiphoton Ionization. *Physical Review Letters*, *71*(13), 1994–1997.

- 53 Pérez-Hernández, J. A., Roso, L., Zaïr, A. and Plaja, L. (2011). Valley in the efficiency of the high-order harmonic yield at ultra-high laser intensities. *Optics Express*, *19*(20), 19430.
- 54 Pérez-Hernández, J. A., Ciappina, M. F., Lewenstein, M., Zaïr, A. and Roso, L. et al. (2014). High-order harmonic generation at high laser intensities beyond the tunnel regime. *The European Physical Journal D*, *68*(7), 195.
- 55 Ditmire, T., Crane, J. K., Nguyen, H., Dasilva, L. B. and Perry, M. D. (1995). Energy-yield and conversion-efficiency measurements of high-order harmonic radiation. , *51*(2), 902–905.
- 56 Falcão-Filho, E. L., Gkortsas, M., Gordon, A. and Kärtner, F. X. (2009). Analytic scaling analysis of high harmonic generation conversion efficiency. *Optics Express*, *17*(13), 11217.
- 57 Colosimo, P., Doumy, G., Blaga, C. I., Wheeler, J. and Hauri, C. et al. (2008). Scaling strong-field interactions towards the classical limit. *Nature Physics*, *4*(5), 386–389.
- 58 Vozzi, C., Calegari, F. and Frassetto et al. (2010). High order harmonics driven by a self-phase-stabilized IR parametric source. *Laser Physics*, *20*(5), 1019–1027.
- 59 Ozawa, A. (2010). *Frequency combs in the extreme ultraviolet*. PhD thesis,.
- 60 Wakui, K., Hayasaka, K. and Ido, T. (2014). Generation of vacuum ultraviolet radiation by intracavity high-harmonic generation toward state detection of single trapped ions. *Applied Physics B-Lasers and Optics*, *117*(3), 957–967.
- 61 Yost, D. C., Schibli, T. R. and Ye, J. (2008). Efficient output coupling of intracavity high-harmonic generation.. *Optics letters*, *33*(10), 1099–101.
- 62 Cingoz, A., Yost, D. C., Allison, T. K., Ruehl, A. and Fermann, M. E. et al. (2011). Direct Frequency Comb Spectroscopy in the Extreme Ultraviolet. *Nature*, *482*(23), 10711.
- 63 Moll, K. D., Jones, R. J. and Ye, J. (2006). Output coupling methods for cavity-based high-harmonic generation.. *Optics express*, *14*(18), 8189–97.
- 64 Weitenberg, J., Ruböldt, P., Pupeza, I., Udem, T. and Hoffmann, H.-D. et al. (2015). Geometrical on-axis access to high-finesse resonators by quasi-imaging: a theoretical description. *Journal of Optics*, *17*(2), 025609.
- 65 Ozawa, A., Vernaleken, A., Schneider, W., Gotlibovych, I. and Udem, T. (2008). Non-collinear high harmonic generation : a promising outcoupling method for cavity-assisted XUV generation. , *16*(9), 383–388.
- 66 Wu, J. and Zeng, H. (2007). Generation for Extreme Ultraviolet Frequency Combs. *Optic Letters*, *32*(22), 3315–3317.
- 67 Philipp, H. R., Cole, H. S., Liu, Y. S. and Sitnik, T. A. (1986). Optical absorption of some polymers in the region 240-170 nm. *Applied Physics Letters*, *48*(2), 192–194.
- 68 Hagemann, H.-J., Gudat, W. and Kunz, C. (1975). Optical constants from the far infrared to the x-ray region: Mg, Al, Cu, Ag, Au, Bi, C, and Al₂O₃. *Journal of the Optical Society of America*, *65*(6), 742.
- 69 D. Palik, E. (1997). *Handbook of Optical Constants of Solids*..

- 70 Kitamura, R., Pilon, L. and Jonasz, M. (2007). Optical constants of silica glass from extreme ultraviolet to far infrared at near room temperature.. *Applied optics*, 46(33), 8118–33.
- 71 Kruit, P., Kimman, J., Muller, H. G. and Van Der Wiel, M. J. (1983). Electron spectra from multiphoton ionization of xenon at 1064, 532, and 355 nm. *Physical Review A*, 28(1), 248–255.
- 72 Chatterjee, K., Boyer, M. C., Wise, W. D. and Hudson, E. W. (2009). An auxiliary capacitor based ultrafast drive circuit for shear piezoelectric motors. *Review of Scientific Instruments*, 80(9).

Curriculum Vitae

Personal details

Name: Dipl.-Ing. Georg Winkler

Born on: March 20th, 1983 in Vienna, Austria

Citizenship: Austrian

Contact: Goethegasse 1/30
2500 Baden, Austria
georg.winkler.at@gmail.com

Education

Oct. 2010 – July 2016 PhD in Physics, Atominstitut, TU Wien.
Experimental thesis in quantum metrology/ultrafast lasers under the supervision of Prof. Thorsten Schumm. Towards high-precision VUV frequency comb spectroscopy of the thorium-229 nuclear isomer

2003 - 2010 Master of Technical Physics, TU Wien. Degree “Diplom-Ingenieur” received with highest honors.
Thesis in quantum optics/cold atoms under the supervision of Prof. Jörg Schmiedmayer. Implementation of a dipole trap on an atom chip.

2002 - Study in Software and Information Engineering, TU Wien.
Baccalaureate thesis finished June 2006 (graded “excellent”)

2001 - 2002 Basic military service.
Promotion to the rank of private first class.
Completion of training as paramedic “with excellence”.

1993 - 2001 Austrian high school with emphasis on foreign languages.
Graduated with highest honors. Major subjects: physics, mathematics and French

